Engineering Sensor-Based Antithetic Integral Controllers for Enhanced Dynamic Performance and Noise Attenuation

Maurice Filo[1,2], Stephanie K. Aoki[1,2], Mucun Hou[1,2], Stanislav Anastassov[1], and Mustafa Khammash[1,*]

[1]Department of Biosystems Science and Engineering, ETH Zürich, 4056 Basel, Switzerland
[2]These authors contributed equally
[*]Correspondence: mustafa.khammash@bsse.ethz.ch

SUMMARY

Effective cellular regulation relies on feedback control mechanisms to maintain homeostasis and mitigate environmental fluctuations. Simple repression-based negative feedback is a widely used regulatory strategy, but it provides limited adaptation capabilities and struggles to effectively reject disturbances. Here, we theoretically and computationally demonstrate that a sensor-based Antithetic Integral Feedback (sAIF) controller enhances this regulatory motif as it achieves robust adaptation while ensuring good transient performance and intrinsic noise suppression. By leveraging a topological refinement, sAIF embeds a proportional feedback component within its integral feedback structure, effectively implementing a biomolecular Proportional-Integral (PI) controller with a single actuation reaction. Theoretical analysis and simulations reveal that sAIF outperforms conventional negative feedback and standard AIF controllers, achieving superior response speed and lower cell-to-cell variability. We implement this controller in *Escherichia coli* using inteins—self-splicing protein segments—to construct a genetically encoded feedback loop. Experimental results confirm that sAIF provides rapid adaptation and robust disturbance rejection over a broad dynamic range. Furthermore, we show that at low expression levels—where noise is most pronounced—the sAIF controller exhibits lower total noise than the parts-matched, no-feedback configuration in a multi-plasmid context that introduces extrinsic noise due to plasmid copy-number variability. This observation is supported by simulations incorporating both intrinsic and extrinsic noise. These findings establish a generalizable design principle for engineering high-performance biological controllers, with broad implications for synthetic biology, metabolic engineering, and cell-based therapies.

KEYWORDS

Genetic Circuits, Robust Perfect Adaptation, Inteins, Integral Feedback Control, Chemical Reaction Networks, Noise, Homeostasis, Cybergenetics

INTRODUCTION

Living cells are complex dynamical systems that interact with their environment and endure disturbances that can disrupt their biomolecular processes. To robustly maintain homeostasis, cells often rely on exquisite feedback control mechanisms[1–4]. Synthetic biology[5] aims to mimic and enhance these natural control capabilities by engineering biomolecular systems and embedding them inside the cells to sense, compute, and actuate in a programmable manner[6,7]. A major challenge in this field is designing feedback controllers capable of managing noise and uncertainty while achieving precision and high performance. Advances in control-theoretic tools[8–12] have driven progress, giving rise to Cybergenetics[13], a discipline at the intersection of synthetic biology and control theory, fostering novel strategies for engineering resilient biomolecular systems.

One of the fundamental tasks of synthetic biomolecular feedback controllers is to maintain homeostasis, a critical property with transformative potential in fields like bioproduction, metabolic engineering, and cell-based therapies, where many diseases stem from homeostatic failure[14]. Robust Perfect Adaptation (RPA)[15–17] is a stringent form of homeostasis, ensuring exact steady-state regulation of a target variable to a setpoint despite varying initial conditions, uncertainties, and constant disturbances. Achieving RPA often requires integral feedback, which drives the steady-state error—the deviation from the desired setpoint—to zero by mathematically integrating the error signal over time[18,19]. The antithetic integral feedback (AIF) controller[20] implements this mechanism as a biochemical reaction network, capable of achieving RPA in both deterministic and stochastic settings where noise enter the dynamics. Stochastic noise[21] can be categorized as intrinsic, arising from the random timing of biochemical reactions, or extrinsic, stemming from variations in global cellular factors such as plasmid copy number, gene expression capacity, or cell size. The AIF motif is proven to be both necessary and minimal for RPA in the stochastic regime[22,23]. Supported by control theory, AIF-based controllers and their variants have rapidly found their way to experimental implementations in *Escherichia coli*[22,24,25] and mammalian cells[26–28].

Since its introduction, efforts to enhance the AIF controller have focused on optimizing dynamic trade-offs[29–31] or incorporating additional circuitry[32–41], including Proportional-Integral-Derivative (PID) controllers and anti-windup strategies. Standalone integral controllers, such as AIF, face limitations: they can only partially shape the dynamic response[32,33] and achieve RPA at the cost of increased intrinsic stochastic noise[34,42] or energetic burden[42], resulting in elevated cell-to-cell variability. These drawbacks can be mitigated by adding proportional and derivative components. In particular, adding proportional feedback was shown to improve dynamic

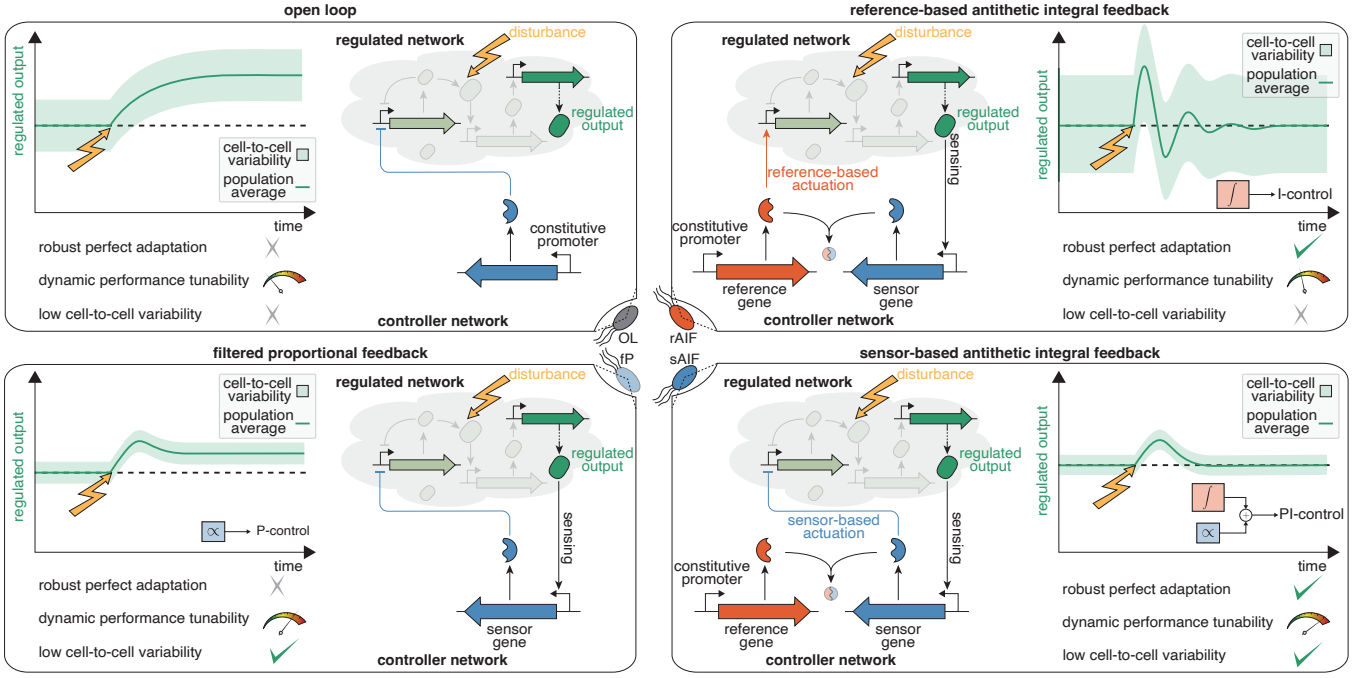

Figure 1: Sensor-based antithetic integral feedback (sAIF) controllers not only achieve Robust Perfect Adaptation (RPA) but also improve dynamic performance and reduce intrinsic cell-to-cell variability. The figure illustrates four genetic circuits for robustly regulating a target output within an arbitrary network. The top-left shows an open-loop configuration without feedback, while the bottom-left depicts a (filtered) proportional feedback controller providing negative feedback from the regulated output via the sensor gene. The top-right and bottom-right circuits represent reference-based (rAIF) and sensor-based (sAIF) AIF controllers, where two genes encode mutually sequestering proteins. Both AIF circuits include a constitutively expressed reference gene, differing in actuation mechanisms via the reference or sensor genes. The plots show that neither the open-loop nor proportional controllers achieve RPA, though the proportional controller reduces steady-state error compared to open-loop. In contrast, rAIF and sAIF both achieve RPA, with sAIF surpassing rAIF by offering superior dynamics and reduced variability, a feat paralleled by the proportional controller. These properties are supported by theory and experiments, attributed to a "hidden" proportional component within the sAIF design.

performance and reduce noise[32–34].

In this paper, we examine and genetically implement a simple variant of the AIF motif, first introduced in[20] Fig. S1 and more recently studied in[42]. This variant retains the basic AIF network topology but replaces one actuation reaction, forming a sensor-based AIF topology (sAIF) shown in Fig. 1. While initially regarded as a standalone integral controller, we demonstrate that it contains a "hidden" proportional component, realizing a *minimal* Proportional-Integral (PI) controller. The design is *minimal* in that it introduces no new species or reactions to the antithetic motif, which is shown to be the minimal integrator in the stochastic setting[38]. Instead, a single reaction is replaced. This subtle modification yields all the added benefits of proportional control, including improved dynamic response and intrinsic noise attenuation, without imposing any additional complexity or burden relative to the original integral controller.

To implement the sAIF controller in bacteria, we utilized inteins for genetic engineering[26]. Inteins are proteins that perform protein splicing reactions without additional cofactors[43–45]. Split inteins, referred to as Int^{N} and Int^{C}, enable sequence exchange, cleavage, or ligation by flanking protein domains, offering versatile functionalities. Previously, we used split inteins to construct reference-based AIF controllers in mammalian cells[26] (Fig. 1). Building on this, we engineer the first biomolecular PI controller in *E. coli* by employing split inteins to implement a sensor-based AIF topology. Our experimental results confirmed its theoretically predicted ability to achieve RPA. The high dynamic performance observed in *E. coli*, alongside our prior mammalian cell study, highlights inteins' versatility across life domains. While our theoretical analyses focus on intrinsic noise, our experimental data also reflect the impact of extrinsic noise arising from plasmid copy number variability in our multi-plasmid design. Even under these conditions, the data show that at low expression levels, closed-loop implementations (including that of the sAIF controller) exhibit lower total noise than open-loop implementations with comparable plasmid copy number variability, consistent with stochastic simulations that account for both intrinsic and extrinsic noise.

Notation

Uppercase bold letters, e.g. $\mathbf{X_1}$, denote species names. Their lowercase counterparts, e.g. $x_1(t)$, represent deterministic time-varying concentrations, while uppercase counterparts, e.g. $X_1(t)$, represent stochastic copy numbers, with t as time. Over-bars, e.g. $\bar{x}_1 \triangleq \lim_{t\to\infty} x_1(t)$, indicate steady-state values (when they exist). Tildes, e.g. $\tilde{x}_1(t) \triangleq x_1(t) - \bar{x}_1$, represent deviations from steady-state, and hats, e.g. $\hat{x}_1(s)$, denote the Laplace transform of $\tilde{x}_1(t)$, where s is the Laplace variable. Variables s and t are omitted when clear from context. The Jacobian of a multi-variable function f, evaluated at $\bar{x} \in \mathbb{R}^n$, is $\partial f(\bar{x})$. $\mathbb{R}^n_+$ and $\mathbb{R}^n_-$ are sets of n-dimensional vectors with non-negative and non-positive entries, respectively. e_i is a vector of appropriate size with all zeros except for the i^{th} entry, which is 1. $\mathbb{E}[X_1]$ and $\text{CV}[X_1]$ denote the expecta-

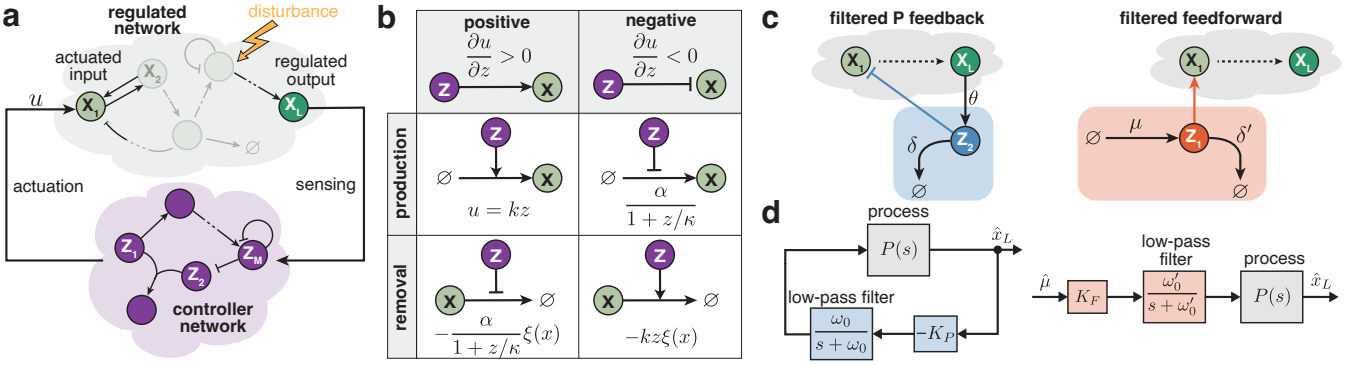

Figure 2: Biomolecular feedback controllers: framework and basic motifs. (a) Closed-loop network: An arbitrary regulated network is in a feedback interconnection with a controller network whose objective is to endow the regulated output of interest $\mathbf{X_L}$ with Robust Perfect Adaptation (RPA), high dynamic performance, and reduced cell-to-cell variability. (b) Examples of actuation mechanisms. A single controller species **Z** actuates **X** via positive (activating production/blocking removal) or negative (blocking production/activating removal) control, determined by the sign of $\partial u/\partial z$. Examples of the functional forms of u are provided. Note that $\xi(x)$ denotes the functional form of degradation. Extended mechanisms with two control species are in SI Fig. S1. (c) Reaction motifs for elementary biomolecular controllers. Left: An intermediate species $\mathbf{Z_2}$ is produced by the output $\mathbf{X_L}$ at a rate θx_L, degrades at a rate δ and closes the loop by negatively actuating the input $\mathbf{X_1}$. Right: An intermediate species $\mathbf{Z_1}$ is constitutively produced at a rate μ, degrades at a rate δ' and positively actuates the input $\mathbf{X_1}$. (d) The underlying control architectures of the basic controller motifs. Note that $P(s)$ is the process transfer function. Linear analysis shows direct feedback realizes a proportional controller (see SI Section S1.1) while indirect feedback through $\mathbf{Z_2}$ realizes a low-pass-filtered proportional controller with cutoff frequency ω_0 and gain K_P. In contrast, actuation with $\mathbf{Z_1}$ enables low-pass-filtered feedforward control with gain K_F and cutoff frequency ω_0'.

tion and coefficient of variation of X_1.

RESULTS

A Framework for Biomolecular Feedback Controllers

The closed-loop network in Fig. 2(a) provides a general framework for biomolecular controllers. It consists of a regulated network (the process) with L species: $\mathbf{X_1}$, $\mathbf{X_2}$, …, $\mathbf{X_L}$, and a controller network with M species: $\mathbf{Z_1}$, $\mathbf{Z_2}$, …, $\mathbf{Z_M}$. The networks interact through (1) a sensing reaction, where the regulated output $\mathbf{X_L}$ influences controller species, and (2) an actuation reaction, where controller species influence the actuated input $\mathbf{X_1}$. The goal is to design a controller network that ensures RPA, maintaining a constant steady-state concentration of $\mathbf{X_L}$ despite uncertainties, persistent disturbances, and varying initial conditions. The controller must also provide good dynamic performance and suppress noise.

We consider the actuation mechanisms in Fig. 2(b), classified as positive or negative and implemented through production or removal reactions. Positive actuation increases production or decreases removal, while negative actuation reduces production or increases removal. This is determined by the derivatives of the control action u, defined next. The actuation reactions and their propensities are

$$\begin{cases} \varnothing \longrightarrow \mathbf{X_1} & \text{propensity: } h^+(z) \\ \mathbf{X_1} \longrightarrow \varnothing & \text{propensity: } h^-(z)\xi(x_1), \end{cases} \tag{1}$$

where $h^{\pm}$ define the actuation mechanisms and $\xi(x_1)$ represents degradation, e.g. $\xi(x_1) = x_1/(x_1+\kappa_x)$ for modeling saturation effects. The total control action is

$$u = h(z;x_1) \triangleq h^+(z) - h^-(z)\xi(x_1). \tag{2}$$

Examples of u's functional forms are listed in Fig. 2(b). With this framework, the deterministic dynamics of the closed-loop network in Fig. 2(a) are

$$\begin{cases} \textbf{process:} & \dot{x} = f(x) + ue_1; \qquad x_L = e_L^T x \\ \textbf{controller:} & \dot{z} = g(z, x_L); \qquad u = h(z, x_L; x_1), \end{cases} \tag{3}$$

where f, g, h are differentiable functions modeling the regulated network, controller dynamics, and control action, respectively, and $x \triangleq [x_1, \ldots, x_L]^T$, $z \triangleq [z_1, \ldots, z_M]^T$. As such, the feedback control problem reduces to designing g and h that ensure RPA while achieving high dynamic performance and possibly suppressing noise in the stochastic setting.

Biomolecular Proportional & Feedforward Control

Consider the two basic control topologies depicted in Fig. 2(c): filtered proportional (fP) feedback and filtered feedforward (fF). Their dynamics are compactly expressed as:

$$\begin{cases} \dot{z}_1 = \mu - \delta' z_1 \\ \dot{z}_2 = \theta x_L - \delta z_2 \\ u = h(z_1, z_2; x_1), \end{cases}$$

	examples of h	parameters
fP	$\dfrac{\alpha}{1+(z_2/\kappa)^n}$	$\mu = \delta' = 0$
fF	kz_1	$\theta = \delta = 0$

(4)

A linear perturbation analysis (detailed in SI Section S1.1) reveals the controller transfer function relating x_L to u as

$$\hat{u}(s) = K_F \frac{\omega_0'}{s+\omega_0'}\hat{\mu}(s) - K_P \frac{\omega_0}{s+\omega_0}\hat{x}_L(s),$$
$$\text{where} \quad K_F \triangleq \frac{\sigma_1}{\delta'}; \quad K_P \triangleq \frac{\sigma_2\theta}{\delta}; \quad \omega_0 \triangleq \delta; \quad \omega_0' \triangleq \delta', \tag{5}$$

and $\partial h(\bar{z}_1, \bar{z}_2; \bar{x}_1) \triangleq \begin{bmatrix}\sigma_1 & -\sigma_2 & \sigma_x\end{bmatrix}$ with $\sigma_1, \sigma_2 \geq 0$. The transfer function in Equation 5, linking the controller's output to its input in the Laplace domain, allows us to draw the block diagrams depicted in Fig. 2(d) which unravel the architectures of the two controllers. The fP

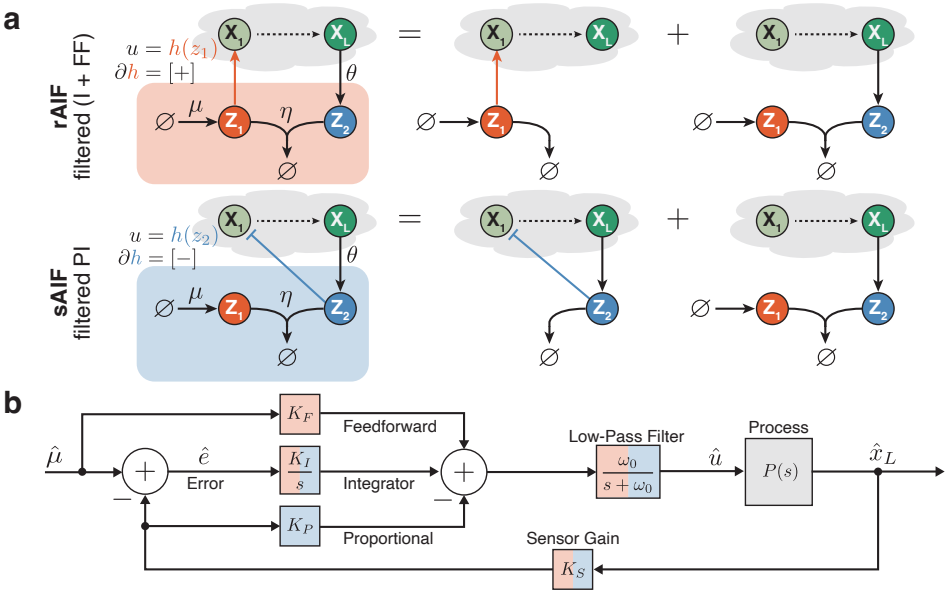

Figure 3: Assembly of biomolecular Proportional-Integral (PI) controllers: integrating a sequestration motif with the basic controller topologies from Fig. 2(c). (a) Different Antithetic Integral Feedback (AIF) reaction motifs. The reference-based AIF (rAIF) controller is obtained by assembling a sequestration motif with the filtered feedforward motif from Fig. 2(c). The sensor-based AIF (sAIF) controller is obtained by assembling a sequestration motif with the filtered P Feedback motif from Fig. 2(c). The key difference lies in the actuation reaction: rAIF uses the reference molecule $\mathbf{Z_1}$ for positive actuation, while sAIF uses the sensor molecule $\mathbf{Z_2}$ for negative actuation. This simple but subtle difference results in entirely distinct control architectures. (b) Underlying control architectures. The block diagram compactly represents the two controllers operating in closed loop, color-coded to match panel (a). The rAIF appends the integrator with a feedforward component with gain K_F, while the sAIF appends it with a proportional component with gain K_P. The resulting PI architecture is thus achieved through a single actuation reaction.

controller passes a proportional control action $-K_P\tilde{x}_L$ through a low-pass filter, which is realized as a simple birth-death process via an intermediate species $\mathbf{Z_2}$ between the output $\mathbf{X_L}$ and input $\mathbf{X_1}$. Note that direct negative actuation of the $\mathbf{X_1}$ by the $\mathbf{X_L}$, without an intermediate species, results in a non-filtered proportional controller (see SI Section S1.1), which is more challenging to implement biologically. Finally, the fF controller has no feedback from $\mathbf{X_L}$, but it also includes a low-pass filter.

Biomolecular Proportional-Integral Control

Next, we "append" the basic controller motifs listed in Fig. 2(c) to the sequestration motif – which lies at the heart of the AIF controller[20] – to obtain the two topologies in Fig. 3(a). The reference-based (rAIF) and sensor-based (sAIF) controllers are obtained by appending the sequestration motif to the filtered feedforward and filtered proportional components from Fig. 2(c), respectively. The dynamics for both controllers can be compactly expressed as

$$\begin{cases} \dot{z}_1 = \mu - \eta z_1 z_2 \\ \dot{z}_2 = \theta x_L - \eta z_1 z_2 \\ u = h(z_1, z_2; x_1), \end{cases} \quad \text{e.g. } u = \begin{cases} \dfrac{\alpha}{1+(z_2/\kappa)^n} & \textbf{(sAIF)} \\ k z_1 & \textbf{(rAIF)}. \end{cases} \tag{6}$$

Equation 6 differs from Equation 4 by replacing simple removal terms with sequestration terms. This is the key modification that leads to a robust steady-state output given by $\bar{x}_L = \mu/\theta$, assuming stability. A linear perturbation analysis (see SI Section S1.2) reveals the control architectures, summarized in the block diagram in Fig. 3(b). The rAIF topology implements integral and feedforward control, both passed through a low-pass filter, while the sAIF topology realizes a PI controller passed through a low-pass filter. Note that the proportional component acts on the output rather than the error signal, consistent with the two degrees of freedom configuration (see[19] Fig. 10.1). While error feedback could be implemented by adding an additional external actuation of $\mathbf{X_1}$[35], it is omitted here to reduce the genetic components required for circuit construction.

Filtered PI Coverage

To conduct a simulation-free evaluation of the dynamic capabilities of the various controller topologies, we examine the achievable ranges of the gains (K_P, K_I) and the cutoff frequency ω_0. Specifically, we ask: can these parameters be tuned to any desired value, and if not, what ranges are achievable? Of course, a broader range indicates greater flexibility in shaping the dynamic response. To address these questions, we first establish a bi-directional mapping between biomolecular parameters and the gain/cutoff-frequency parameters, translating biological constraints (e.g., positivity) into the gain/cutoff-frequency space to reveal the attainable ranges. Here, we present the results for the sAIF topology, with details in SI Section S2.

Consider the sAIF controller in Fig. 3(a). We treat two biologically-relevant functional forms of h implementing the two negative actuation mechanisms shown in Fig. 2(b). Specifically, we have $u = h(z_2; x_1)$ with

$$h(z_2; x_1) = \begin{cases} \dfrac{\alpha}{1+(z_2/\kappa)^n} & \textbf{(Repression)} \\ \alpha - \gamma z_2 \xi(x_1) & \textbf{(Degradation)}, \end{cases} \tag{7}$$

where $\xi(x_1) = \frac{x_1}{x_1+\kappa_x}$. As established in SI Section S2, the achievable gain and cutoff frequency sets for repression $(\mathcal{S}_r^n)$ and degradation $(\mathcal{S}_d)$ are

$$\begin{aligned} \mathcal{S}_r^n &= \left\{ (K_P, K_I, \omega_0) \in \mathbb{R}_+^3 : K_P < n\frac{\bar{u}}{\mu},\ K_I < \omega_0 K_P \left(1 - \frac{\mu K_P}{n\bar{u}}\right) \right\} \\ \mathcal{S}_d &= \left\{ (K_P, K_I, \omega_0) \in \mathbb{R}_+^3 : K_I < \omega_0 K_P \right\}, \end{aligned} \tag{8}$$

where $\bar{u}$ is the supporting input that depends solely on the desired setpoint and the process (see SI Section S2, Assumption 1). Observe that for all $n = 1, 2, \cdots$, we have $\mathcal{S}_r^n \subset \mathcal{S}_r^{n+1} \subset \mathcal{S}_d$, and $\mathcal{S}_r^n$ converges to $\mathcal{S}_d$ as $n \to \infty$. Equation 8 indicates that repression constrains

the achievable proportional and integral gains K_P and K_I, but increasing cooperativity n expands the range, thus offering more flexibility in tuning the filtered PI parameters. Degradation, by contrast, constrains only the integral gain K_I. Note that these filtered PI controllers have more constrained achievable ranges compared to two-reaction PI controllers[32,33], reflecting the trade-off for embedding proportional and integral feedback in a single actuation reaction.

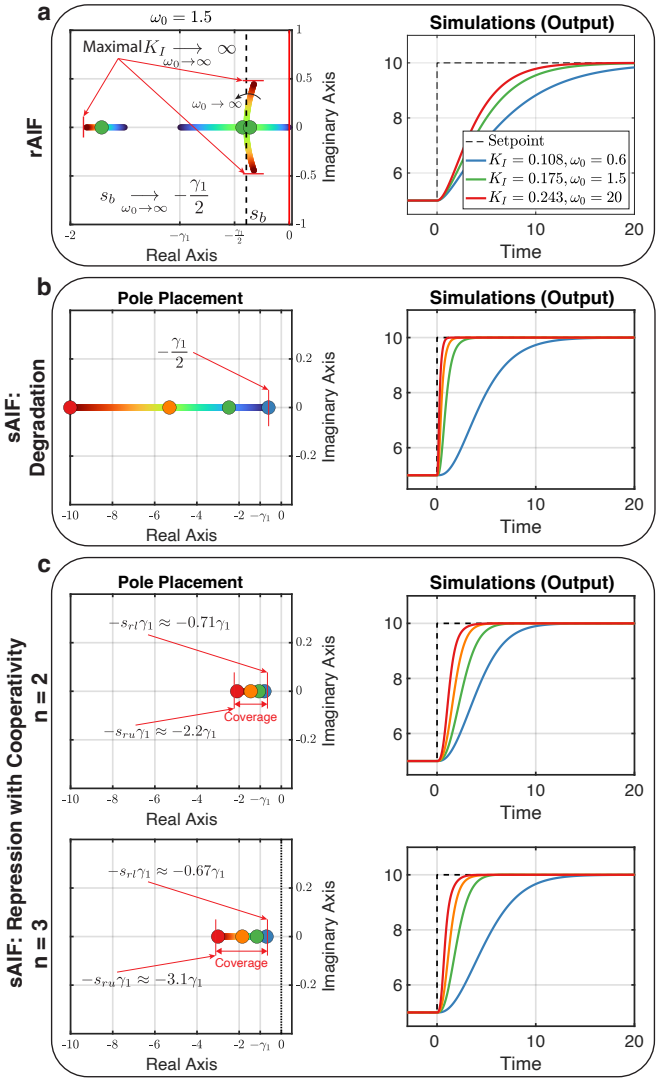

Figure 4: Dynamic Performance Assessment. A birth-death process (see Fig. 5(a), left) is controlled by rAIF and sAIF. (a) rAIF Performance Limitation. The response cannot be sped up beyond a certain threshold without inflicting oscillations. The left plot shows the locus of the eigenvalues as the integral gain K_I is increased while the cutoff frequency ω_0 is fixed. Note that s_b, calculated analytically in Equation S25, denotes the breaking point where two eigenvalues meet on the real axis and break away to become complex conjugates. As ω_0 is increased, one real eigenvalue moves more to the left and the breaking point s_b tends to $-\gamma_1/2$. Therefore, the dominant eigenvalue is confined by the breaking point s_b which imposes a limitation on the achievable performance as demonstrated in the simulations. (b) and (c) sAIF Design Flexibility. These two panels show the results of pole-placement where the three closed-loop eigenvalues are placed on the real axis of the left-half plane to ensure a stable and non-oscillating response. Unlike with repression actuation, degradation actuation allows us to place the eigenvalues arbitrarily as far to the left as desired to obtain a step-like response. However, cooperativity helps in mitigating the restriction with repression actuation. The numerical values of the parameters are $\gamma_1 = 1, \mu = 5, \theta = 1, \kappa_1 = 10^{-5}$. To change the setpoint at $t = 0$, μ is doubled. A more detailed version of this figure showing the mappings from the eigenvalues to the gains and biomolecular parameters can be found in SI Fig. S3.

sAIF Controllers Enhance Dynamic Performance

Next, we demonstrate, analytically and through simulations, that sAIF offers more flexibility in shaping the dynamics compared to rAIF. We also explore the performance-enhancement capabilities of the two negative actuation mechanisms. We adopt a root locus methodology similar to the one used in our previous work[32], where we analyzed other network topologies.

Consider the closed-loop dynamics of a simple one-species birth-death process, i.e. $f(x) \triangleq -\gamma_1 x + u$, which is sufficient to highlight the proportional component's added flexibility. The process transfer function is $P(s) = \frac{1}{s+\gamma_1}$. Using the block diagram in Fig. 3(b), the closed-loop transfer function for the linearized dynamics of rAIF ($K_P = 0, K_F > 0$) and sAIF ($K_P > 0, K_F = 0$) is calculated as $H(s) \triangleq \frac{\hat{x}_L(s)}{\hat{\mu}(s)}$, with

$$H(s) = \frac{\omega_0(K_F s + K_I)}{s^3 + (\omega_0 + \gamma_1)s^2 + \omega_0\left(\gamma_1 + K_P K_S\right)s + \omega_0 K_S K_I}. \tag{9}$$

Root-locus analysis (see SI Section S3) shows that for rAIF, at least one pole cannot be placed left of $s = -\frac{\gamma_1}{2}$, regardless of how K_I is tuned or how fast the cutoff frequency ω_0 (i.e. sequestration rate η) is. This limits rAIF's response speed to a threshold dictated by $\frac{\gamma_1}{2}$. This limitation is analytically established in SI Section S3 and illustrated in Fig. 4(a).

This is exactly where the filtered-proportional component, enabled by actuation via $\mathbf{Z_2}$ instead of $\mathbf{Z_1}$, adds crucial flexibility. To illustrate this, consider the pole placement design problem: the goal is to select PI gains (K_P, K_I) and cutoff frequency ω_0 to place the three closed-loop poles at $s = -a$. For stability, $a > 0$ should place the poles in the left-half complex plane, on the real axis to avoid oscillations, and farther left for faster transient responses. We investigate whether sAIF, with repression or degradation actuation, can achieve this. If so, we analyze the achievable pole placement range and its impact on the dynamics.

First, we aim at placing the three closed-loop poles at the same location $s = -a$. As a result, the characteristic polynomial is given by

$$p(s) = (s + a)^3 = s^3 + 3as^2 + 3a^2 s + a^3. \tag{10}$$

Equating $p(s)$ to the denominator of $H(s)$ allows us to express the designed PI gains (K_P, K_I) and cutoff frequency ω_0 in terms of the birth-death parameter γ_1, the sensing gain K_S and the placed pole $-a$ as

$$K_P = \frac{3a^2 - \gamma_1(3a - \gamma_1)}{K_S(3a - \gamma_1)}, \quad K_I = \frac{a^3}{K_S(3a - \gamma_1)}, \quad \omega_0 = 3a - \gamma_1. \tag{11}$$

The sets of achievable PI gains and cutoff frequencies in Equation 8 constrain the achievable poles $s = -a$ to the following regions on the real axis

$$\begin{aligned} \textbf{Rep:} \quad & (K_P, K_I, \omega_0) \in \mathcal{S}_r^n \implies s_l(n)\gamma_1 < a < s_u(n)\gamma_1 \\ \textbf{Deg:} \quad & (K_P, K_I, \omega_0) \in \mathcal{S}_d \implies a > \frac{\gamma_1}{2}, \end{aligned} \tag{12}$$

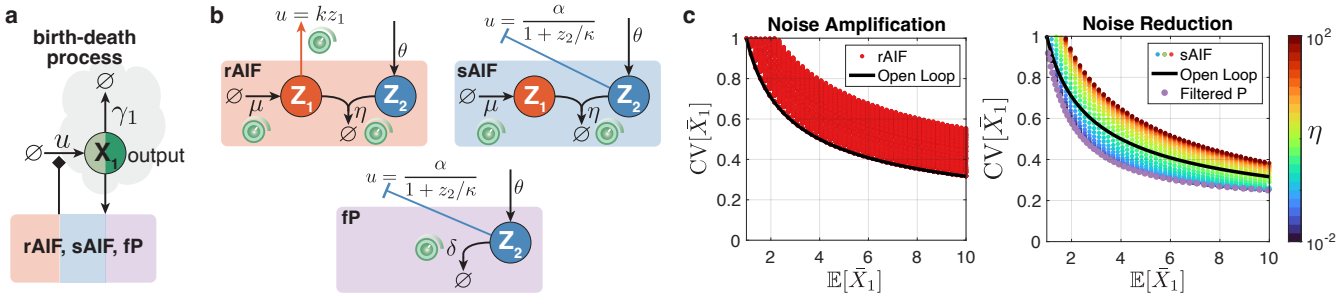

Figure 5: Stochastic noise attenuation capabilities and limitations. (a) We examine a case study for the process to be regulated: a birth-death process. Note that the square shaped arrowhead indicates either activation or repression. Two additional case studies for processes with a higher number of species are shown to exhibit the same conclusions in SI Fig. S5. (b) The process is controlled by three different controllers: rAIF and sAIF, which supplement integral controllers with filtered feedforward and proportional components, respectively, and a fP controller without an integrator. (c) displays the relationship between the coefficients of variation and expectations at stationarity for the regulated output $\mathbf{X_1}$. The left plot corresponds to rAIF, while the right plot corresponds to sAIF and fP feedback. The key takeaway from these plots is that rAIF can only increase noise compared to the open-loop scenario, while sAIF can attenuate noise to a certain extent, limited by a "hidden" proportional component. The simulations support the notion that integral controllers amplify noise, whereas proportional controllers attenuate it. The solid black lines are calculated analytically using Equation 13, while the various circles are computed empirically through the stochastic simulation algorithm[46], generating $10^4 - 10^5$ trajectories on the Euler cluster (https://scicomp.ethz.ch/wiki/Euler). Numerical values for the birth-death process are: $\gamma_1 = 0.1$. The controller parameter values are as follows: $\alpha = 2, \theta = 1, \kappa = 0.05, \eta \in [10^{-2}, 10^2], k \in [10^{-3}, 1], \delta \in [0.1, 20], \mu \in [1, 10]$.

where $s_l(n)$ and $s_u(n)$ are calculated analytically in SI Section S4. With degradation actuation, there is no theoretical upper limit on pole placement, as shown in Fig. 4(b), where poles can be moved far left to achieve an ideal step-like response. This highlights sAIF's ability to fully shape the dynamics of a birth-death process, unlike rAIF. In contrast, repression actuation constrains pole placement to the open set $\mathcal{R}(n) = (-s_u(n)\gamma_1, -s_l(n)\gamma_1)$. Without cooperativity ($n = 1$), we have $s_l(1) = s_u(1) = 1$ and thus $\mathcal{R}(1)$ is empty, making it impossible to place poles at the same location. For $n = 2$, $\mathcal{R}(2)$ expands $(s_l(2) \approx 0.7082, s_u(2) \approx 2.1769)$, showing cooperativity is necessary for single-location pole placement. Higher cooperativity ($n > 2$) further broadens $\mathcal{R}(n)$, as illustrated in Fig. 4(c). Finally, the case where repression is used without cooperativity ($n = 1$) is treated separately in SI Section S4. Here, the poles must be placed at two locations. The transient response speed is shown to be limited by γ_1, still exceeding the rAIF threshold of $\gamma_1/2$. Additional details are in SI Fig. S3(d). Similar behaviors were observed in the nonlinear stochastic simulations, as shown in SI Fig. S4, which depict the evolution of average concentrations. This is expected, as the pole placement derived from the linearized deterministic models serves as an approximate analysis of the mean dynamics for the stochastic setting under the linear noise approximation.

In conclusion, this case study demonstrates that sAIF outperforms rAIF in dynamic performance. Using degradation for sAIF's negative actuation allows arbitrary acceleration of the transient response of a birth-death process without overshoots or oscillations. While repression-based actuation also improves performance compared to rAIF, it cannot achieve arbitrary speed. However, this limitation is mitigated by adding cooperativity to the repression. Note that cooperativity does not help pole placement for the rAIF controller because, with $K_P = 0$, only two degrees of freedom (K_I, ω_0) are available to place the three poles of the transfer function in Equation 9. Thus, replacing the actuation $u = kz_1$ with a cooperative Hill function still limits pole placement.

Limits of Intrinsic Stochastic Noise Attenuation

This section examines the intrinsic noise attenuation capabilities of rAIF, sAIF, and fP controllers in the stochastic setting. Noise is defined as the relationship between the coefficient of variation (CV) and the expectation at stationarity[42]. We consider the simple birth-death model of Fig. 5(a) as the process, controlled by the rAIF, sAIF and fP controllers of Fig. 5(b). Two processes with more species are also presented in SI Fig. S5. Throughout the analysis, the process parameter γ_1 is fixed, and negative actuations are implemented as repression reactions. In the open-loop case, the actuation $u = \alpha$ is constant, resulting in a unimolecular network with closed moment equations. The stationary CV of the output is explicitly expressed in terms of the expectation as

$$\mathrm{CV}[\bar{X}_L] = \sqrt{\frac{1}{\mathbb{E}[\bar{X}_L]}}. \tag{13}$$

This analytical expression is shown as a solid black curve in Fig. 5(c). Stochastic simulations for the closed-loop scenarios with each controller are carried out to compute stationary expectations and CVs across a range of controller parameters. For rAIF, k, η, and μ are varied with θ fixed. Results, shown as data points in Fig. 5(c) (left), reveal that rAIF increases noise compared to the open-loop case. For sAIF, η and μ are varied while α, κ, and θ remain fixed. The simulation results, color-coded by η, are depicted in Fig. 5(c) (right) and show that sAIF control reduces noise below open-loop levels as demonstrated previously by Kell et al.[42] through similar simulations and linear noise approximations. We show that this observation generalizes to more complex regulated processes in SI Fig. S5. The key distinction from[42] is that we uncover the control-theoretic basis for the observed noise attenuation and identify its lower bound, as described next. Comparable simulations for the fP controller are carried out by varying δ with the remaining parameters matched to those of the sAIF controller. The results are shown as purple points in Fig. 5(c) (right). This suggests that the noise attenuation in sAIF control is at-

tributable to a "hidden" proportional component, rather than the integrator. In fact, as η increases in sAIF, noise rises, consistent with the proportional gain K_P approaching zero as $\eta \to \infty$.

Motivated by the outcomes of stochastic simulations, we apply the linear noise approximation (LNA) technique to obtain analytical expressions for the CV in the case of a birth-death process. This analytical exploration is detailed in SI Section S5. Through this analysis, we analytically confirm the relationship observed between the deterministic and stochastic frameworks, demonstrating that noise levels indeed rise with an increase in η, and highlighting that the capacity of the sAIF controller to reduce noise is bounded by its filtered-proportional component, as indicated in Equation S52.

Steady-State Errors in Non-Ideal Settings

In practice, controller species always dilute at some rate δ, as illustrated in Fig. 6(a). It is well-known that this dilution effect introduces a "leaky integrator", which results in a steady-state error[20,22,31]. This raises a reasonable question: given that steady-state error is inevitable with dilution, why not simply use a (filtered) proportional controller and avoid the added circuit complexity of incorporating an additional controller species? The following theorem addresses this question by proving that even the non-ideal sAIF controller consistently outperforms the filtered proportional controller in terms of sensitivity to disturbances.

Theorem 1. *For any strictly monotonic regulated network under a constant disturbance Δ, operating in negative feedback with either a non-ideal sAIF or filtered proportional (fP) controller, assume identical dilution rate δ and strictly monotonic actuation mechanisms h_s for both controllers (see Fig. 6(a)). At any desired steady-state output $\bar{x}_L = r$, the steady-state sensitivities to the disturbance satisfy*

$$\left|\frac{\partial \bar{x}_L}{\partial \Delta}\right|^{sAIF} < \left|\frac{\partial \bar{x}_L}{\partial \Delta}\right|^{fP}.$$

Moreover, if either μ or θ is fixed and the other tuned to maintain $\bar{x}_L = r$, the sensitivity strictly decreases as the sequestration rate η increases.

The proof can be found in SI Section S6.1.1. This result is general and applies to the deterministic setting for any regulated process with a strictly monotonic dose-response. Figure 6(b) illustrates a numerical demonstration, where the regulated process is a simple birth-death process (see Fig. 5(a)). Steady-state outputs are computed for various values of μ, θ, and η (non-ideal sAIF controller) and θ_p (fP controller), both before and after introducing a disturbance. The relative steady-state error, plotted against the output before the disturbance, is consistently lower for the sAIF controller compared to the fP controller. A more detailed plot for the same example can be found in Fig. S6 demonstrating that the lower bound of the error is achieved as $\eta \to \infty$.

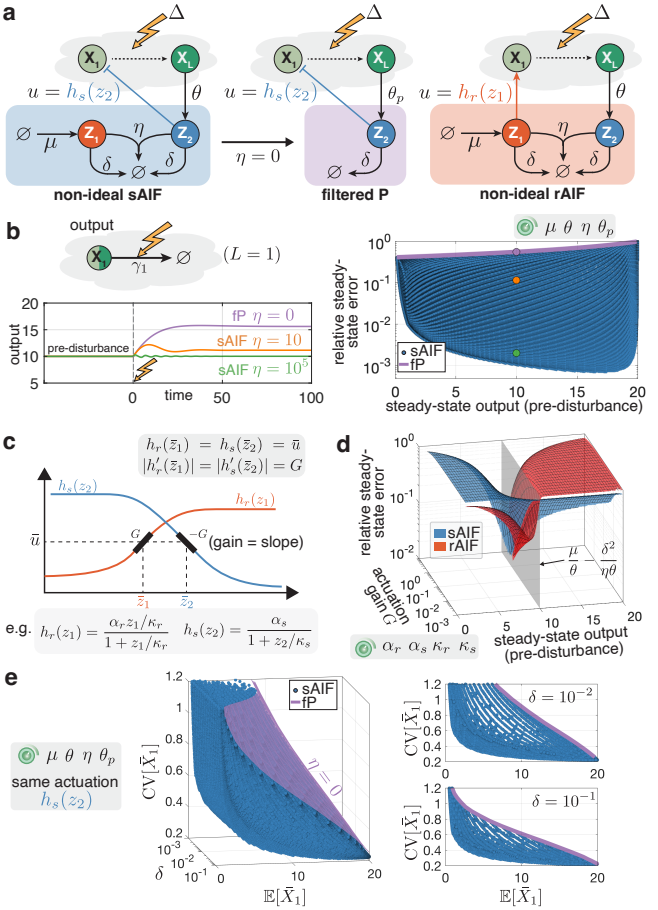

Figure 6: Non-ideal setting. (a) Closed-loop networks with non-ideal sAIF, rAIF, and fP controllers. Here, the fP controller is the same as that in Fig. 5(b), while the non-ideal sAIF and rAIF controllers now include dilution of the controller species at the same rate δ. (b) Numerical demonstration showing the strictly lower steady-state error achieved by the non-ideal sAIF compared to the fP controller. The regulated network is a simple birth-death process with a disturbance affecting the degradation rate. Parameters μ, θ, η, and θ_p are varied to plot the relative steady-state error against the output before disturbance. The bottom plot shows time responses for three cases, illustrating reduced error as η increases. More details including the numerical values can be found in SI Fig. S6. (c) Actuation functions for sAIF and rAIF controllers, ensuring fair comparison by matching the function values and their derivative magnitudes (gain G). (d) Numerical comparison of steady-state errors for non-ideal sAIF and rAIF controllers, using the same regulated network and disturbance as in panel (b). Parameters α_r, α_s, κ_r, and κ_s are varied to plot the relative steady-state error against actuation gain and pre-disturbance output. The results show a performance switch as $\bar{x}_L$ crosses the threshold defined in Theorem 2. (e) Comparison of noise between the non-ideal sAIF and fP controller. Both controllers share the same actuation function h_s, with μ, θ, η, δ, and θ_p varied while other parameters remain fixed. Stochastic simulations are conducted to empirically plot, in 3D, the stationary CVs against the stationary expectation and dilution rate δ. For clarity, two slices are shown for $\delta \in \{10^{-2}, 10^{-1}\}$. The results demonstrate that, in practical settings where the repressor and dilution rate are identical for both controllers, the non-ideal sAIF consistently performs as well as or better than the fP controller. Numerical values can be found in SI Fig. S8.

We now present a theorem comparing the steady-state sensitivities of the non-ideal sAIF and rAIF controllers.

Theorem 2. *For any strictly monotonic regulated network under a constant disturbance Δ, operating in negative feedback with either a non-ideal sAIF or rAIF controller, assume identical controller parameters μ, θ, η, and δ for both controllers (see Fig. 6(a)). At any fixed desired steady-state output $\bar{x}_L$, the steady-state sensi-*

tivities to the disturbance satisfy:

$$\begin{cases} \left|\dfrac{\partial \bar{x}_L}{\partial \Delta}\right|^{\text{sAIF}} < \left|\dfrac{\partial \bar{x}_L}{\partial \Delta}\right|^{\text{rAIF}} & \text{if} \quad \bar{x}_L > \dfrac{\mu}{\theta} - \dfrac{\delta^2}{\eta\theta}, \\ \left|\dfrac{\partial \bar{x}_L}{\partial \Delta}\right|^{\text{sAIF}} > \left|\dfrac{\partial \bar{x}_L}{\partial \Delta}\right|^{\text{rAIF}} & \text{if} \quad \bar{x}_L < \dfrac{\mu}{\theta} - \dfrac{\delta^2}{\eta\theta}, \end{cases}$$

assuming the absolute value of the actuation gains of both controllers are matched (see Fig. 6(c)).

The proof can be found in SI Section S6.1.2. This result provides a complete characterization of when the non-ideal sAIF and rAIF controllers outperform each other in terms of steady-state sensitivities to disturbances. Notably, the condition is straightforward, depending solely on the desired steady-state level $\bar{x}_L$ and the controller parameters μ, θ, and δ, without relying on the specifics of the regulated process. Figure 6(d) presents a numerical demonstration of relative steady-state error across a range of actuation gains and pre-disturbance outputs. The results clearly show that for a desired setpoint below $\mu/\theta - \delta^2/\eta\theta$, the non-ideal rAIF controller achieves lower error, while the non-ideal sAIF outperforms it above this threshold.

We conclude this section by analyzing the trade-off between dynamic performance and steady-state error in the non-ideal setting. A comprehensive simulation study was performed, scanning all controller parameters for both sAIF and rAIF designs to jointly evaluate steady-state error and settling time. As shown in SI Fig.S7, the sAIF controller achieves faster settling times without sacrificing steady-state accuracy. As predicted by Theorem 2, the rAIF can yield slightly lower steady-state error at low setpoints, but only at the cost of longer settling times—highlighting the trade-off. The improved performance of sAIF is, once again, attributed to its proportional component, which offers an extra degree of control and helps relax this trade-off.

Intrinsic Noise in Non-Ideal Settings

Simulation studies in Fig. 5 and SI Fig. S8, supported by theoretical analysis, show that for a given setpoint, tuning the degradation rate δ of $\mathbf{Z_2}$ in the fP controller can achieve the lowest stationary CV compared to the sAIF controller for a fixed θ. However, in practice, tuning the degradation rate may be difficult, while tuning θ is easier (as done experimentally in Fig. 7). Furthermore, dilution affects both controllers similarly. To this end, we now examine the stochastic setting of the fP and non-ideal sAIF controllers in Fig. 6(a), where the expressed repressor $\mathbf{Z_2}$ is identical for both controllers. This practical scenario focuses on the design question: given a shared repressor which dilutes at a rate δ, is it better to reduce noise with or without sequestration?

The simulation study in Fig. 6(e) demonstrates that in this practical scenario, the non-ideal sAIF controller consistently performs as well as or better than the fP controller in reducing stationary noise. Using the same regulated network as in Fig. 6(b), we vary μ, θ, and η for the non-ideal sAIF controller and θ_p for the fP controller across different values of δ. The CV and expectation are computed and plotted in 3D, along with slices for $\delta \in \{10^{-2}, 10^{-1}\}$. The results clearly show that for any $\mathbb{E}[\bar{X}_1]$ and δ, $\text{CV}[\bar{X}_1]^{\text{sAIF}} \leq \text{CV}[\bar{X}_1]^{\text{fP}}$. This conclusion holds also for more complicated regulated networks as demonstrated in the numerical simulations of SI Fig. S8.

Motivated by the outcomes of our stochastic simulations, we once again apply the LNA technique to obtain analytical expressions for the CV in the case of a birth-death process as detailed in SI Section S6.2. Through this analysis, we obtain that for a fixed desired setpoint $\mathbb{E}[\bar{X}_1] = r$, we have $\left.\frac{\partial \text{CV}[\bar{X}]}{\partial \eta}\right|_{\eta=0} < 0$. This aligns with the simulation results, showing that as we transition from the filtered P controller ($\eta = 0$) to the non-ideal sAIF controller ($\eta > 0$) at the same setpoint, the CV decreases.

Genetic Implementation

In this section, we build and test the sAIF and filtered proportional controllers in *E. coli*. To do so, we leverage the flexibility offered by inteins in building genetic control systems[26].

The genetic circuits used in the experiments are shown in Fig. 7(a). Each circuit consists of three genes distributed across three plasmids: Genes 1 and 2 form the controller components, while Gene 3 represents the regulated process. For clarity, dummy plasmids—used to ensure similar plasmid burden across circuits but which do not influence the regulated output—are not shown in Fig. 7(a), but are fully detailed in SI Fig.S9(a). The configuration of Genes 1 and 2 determines the type of controller: three open-loop circuits are shown on the left, filtered-proportional control in the center, and sAIF control on the right. These circuits were carefully designed to minimize differences in genetic components across configurations, enabling a fair comparison—particularly in relation to extrinsic noise, which is not accounted for in the theoretical analysis. A more detailed discussion of extrinsic noise is provided in the following section.

We begin by introducing the open-loop systems which are available in three configurations. Open Loop 1 (OL 1) serves as the minimal non-actuated configuration. Gene 3—encoding the *E. coli* transcription factor AraC fused to the red fluorescent protein mScarlet-I (denoted as the regulated output $\mathbf{X_1}$)—is driven by a constitutive promoter, with no interaction from controller components. Open Loop 2 (OL 2) introduces the actuator $\mathbf{Z_2}$, encoded by Gene 2, which resides on plasmid 2. This gene is driven by a constitutive promoter and encodes a Tetracycline Repressor (TetR) protein with a split intein Int^{C} inserted into its dimerization domain. Gene 3 is driven by the P_{TET} promoter, which is repressed by TetR and can be chemically induced using anhydrotetracycline (aTc). Open Loop 3 (OL 3) builds on OL 2 by introducing Gene 1 on plasmid 1, which encodes a different split intein, Int^{N}. This enables intein-splicing between $\mathbf{Z_1}$ (Int^{N}) and $\mathbf{Z_2}$ (Int^{C}), thereby sequestering TetR's repressive function and modulating the regulation of $\mathbf{X_1}$. Like OL 2,

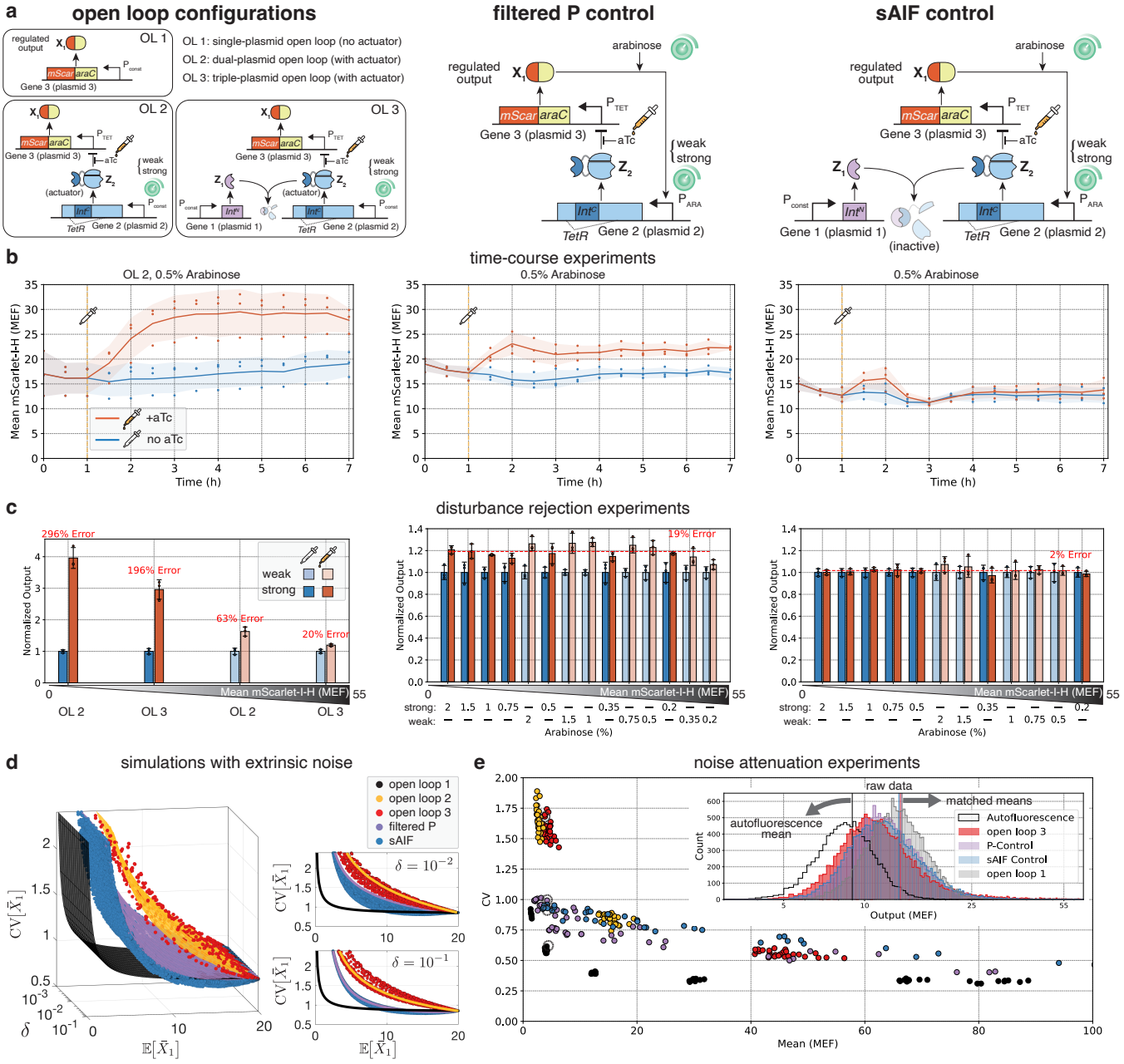

Figure 7: Genetic implementation and experimental validation of intein-based feedback controllers in *Escherichia coli*. (a) Schematic diagrams of three Open Loop configurations, Filtered Proportional (fP) Control, and sensor-based Antithetic Integral Feedback (sAIF) Control circuits. The controllers consist of Gene 1 and Gene 2, which actuate the regulated process, represented by Gene 3, via the TetR protein which represses the P_{TET} promoter. Gene 3 expresses the output of interest represented by AraC fused to mScarlet-I, serving as a fluorescent reporter. Each gene is cloned on a separate plasmid. Note that anhydrotetracycline (aTc) serves as an external perturbation in these experiments. (b) Time-course experiments displaying the dynamic response of the output to a disturbance induced by aTc at 1 hour, with 0.5% arabinose present to enable feedback in closed-loop configurations. The blue and red curves represent the mean response of three biological replicates (depicted by the colored dots at 30-minute intervals) for undisturbed and disturbed conditions, respectively. The shaded areas around the curves indicate the standard deviation from the mean of these triplicates. It is important to note that the different configurations were deliberately chosen to ensure that the undisturbed responses would have similar levels, all measured in Molecules of Equivalent Fluorochrome (MEF) units[47,48]. See SI Fig. S10 for more comparisons at different steady-state levels. All circuits are observed to reach a steady state, with the sAIF controller demonstrating an exceptionally small steady-state error and exhibiting favorable dynamic behavior. (c) Bar graphs showing disturbance rejection capabilities of each circuit, across a wide range of setpoints, with the steady-state output levels normalized to the steady-state undisturbed levels and indicated by different arabinose concentrations. Output levels, based on three biological replicate measurements, are ordered by increasing mean values. The color shade of the bars (light/dark) indicates the expression strength of Gene 2 (weak/strong). Error bars reflect the standard deviations from the triplicate data. The displayed results demonstrate the varied responses to disturbance: significant deviations in open-loop circuits, a moderate reduction in the disturbance effect with the fP controller, and a near-complete eradication of disturbance in the sAIF controller circuit. The non-normalized data can be found in SI Fig. S11. (d) Simulation results incorporating both intrinsic and extrinsic noise. This panel parallels Fig. 6(e), now including extrinsic noise from plasmid copy number variability. Results for the sAIF and fP controllers are shown alongside the three open-loop configurations. See SI Fig. S9 for more details. (e) Noise properties in an sAIF controller: The histograms in the inset display raw data for both the autofluorescence of cells and the output fluorescence for one instance of each closed-loop circuit and two open loop configurations, pointed out with dashed circles, all with matched means. Using tools developed in[47,48], the undisturbed steady-state data from our circuits, shown in panel (c), as well as undisturbed OL 1 data, have been processed to remove debris, autofluorescence and outliers (see Methods). This leads to the scatter plot, which correlates the mean output expression level with the coefficient of variation (CV) to compare the noise properties of the different control circuits. Three biological replicates are plotted, each circle representing one biological replicate.

Gene 3 is driven by the P_{TET} promoter and responds to aTc induction. In both OL 2 and OL 3, the promoter driving Gene 2 is varied between weak and strong versions, enabling tunable output levels. Note that OL 2

with a strong promoter yields the lowest $\mathbf{X_1}$ expression due to stronger repression, while OL 3 with a weak promoter achieves the highest expression—benefiting from both reduced repression and active sequestration. In all open-loop configurations, there is no feedback from $\mathbf{X_1}$ to the controller. The inducer aTc is reserved in these experiments for introducing external disturbances to assess the disturbance rejection capabilities of the various control architectures.

Next, we introduce the filtered-proportional controller circuit, a design that is essentially achieved by a slight modification of the OL 2 configuration. The key adjustment involves substituting the constitutive promoter that drives Gene 2 with the P_{ARA} promoter. This promoter is activated by the AraC protein and can be induced by arabinose. This slight alteration establishes a feedback mechanism by incorporating a sensing reaction which monitors the level of the regulated output $\mathbf{X_1}$ and provides a negative feedback response. Note that arabinose is reserved for tuning the setpoint (steady-state level of the regulated output $\mathbf{X_1}$) – more arabinose yields a lower setpoint, since arabinose plays a role similar to θ in Fig. 2(c). Similar to the setup in the open-loop configurations, the expression strength of Gene 2 is available in two levels: strong and weak. However, in contrast to the open-loop configuration, here, the variation in expression strength is achieved via ribozymes (see Methods). Finally, we present the sAIF controller circuit. This design is, once again, derived from a minor, but essential, modification to the filtered-proportional controller circuit. This primary change introduces Gene 1, as in OL 3, thus enabling the intein splicing reaction in the feedback loop which lies at the heart of the sAIF topology depicted in Fig. 3(a).

We close this section by pointing out that we did not construct an intein-based rAIF controller for direct comparison in this study. Experimental comparison between rAIF and sAIF circuits is nontrivial, as they rely on different actuator parts. In contrast, the sAIF and filtered proportional controllers share the same actuator, allowing for a more direct comparison.

Experimental Assessment of the Genetic Controllers

After constructing the genetic circuits, we evaluated their performance, focusing on their temporal response, their ability to reject disturbances and their noise properties. Fig. 7(b) shows the results of time-course experiments that examined the transient responses of the circuits to the addition of 0.5 ng/mL of aTc as an external disturbance at time $t = 1$h. In the experiments involving closed-loop configurations, 0.5% arabinose was introduced to activate the sensing mechanisms and to adjust the setpoint to levels comparable to those observed in the open-loop configuration. It was observed that all circuits reached a steady state within a 6-hour period. As expected, the open-loop circuits demonstrated a significant deviation from its undisturbed state. The filtered-proportional controller circuit was more effective in mitigating the disturbance impact compared to the open-loop setup, though it still exhibited a residual steady-state error. The sAIF controller circuit, however, was notably successful in almost completely rejecting the disturbance, thereby achieving RPA. Indeed, the responses with and without disturbance settle to levels indistinguishable within the precision of triplicate measurements.

To further explore disturbance rejection across various setpoints, we introduced a range of arabinose concentrations (ranging from $0.2 - 2\%$) and recorded the steady-state output levels with and without the aTc disturbance. These findings, depicted in the bar graphs of Fig. 7(c), are normalized to their respective undisturbed states and are organized by ascending output levels on the x-axis. Unnormalized plots are provided in SI Fig. S11. The results reinforced our expectations: the open-loop circuits failed to counteract the disturbance, showing large steady-state errors. In contrast, the filtered-proportional controller reduced the disturbance's impact to an average steady-state error of 19%, and the sAIF controller excelled by nearly eradicating the disturbance, leading to a minimal steady-state error of just 2%. This insignificant steady-state error is within the error bars of the biological triplicates. Interestingly, the impact of the aTc disturbance was more pronounced at lower setpoints (which correspond to higher arabinose levels), suggesting a diminished sensitivity to this disturbance at lower TetR concentrations.

Next, we examine the experimental noise properties of the various built circuits. However, the experimental setup cannot be directly compared to the theoretical analysis in Fig. 6(e), as the experiments include both intrinsic and extrinsic noise, whereas the theoretical analysis considers only intrinsic noise. As such, we performed additional simulations incorporating extrinsic noise, specifically due to variability in plasmid copy numbers, using data from[49] that match the plasmid origins of replication we use. Since circuits with more plasmids introduce more extrinsic noise, this factor is critical for a fair comparison. We simulated and experimentally measured all the circuits in Fig.7(a). Simulation details, combining both intrinsic and extrinsic noise, are provided in SI Fig. S9 and the results are summarized in Fig.7(d), where the CV is plotted against the mean and the dilution rate δ as in Fig. 6(e). With both intrinsic and extrinsic noise present, sAIF does not reduce noise relative to OL 1 (no actuator). This contrasts with the idealized intrinsic-only setting (Fig. 5), where sAIF can attenuate noise relative to OL1. When extrinsic noise is included, simulations show at most a very narrow, marginal attenuation window—too small to be reliably observed experimentally. This limitation arises because it is designed to involve three different plasmids compared to only one plasmid in the OL 1 configuration, amplifying extrinsic variability. However, when compared to OL 2—which uses only one additional plasmid to house the actuator gene expressing $\mathbf{Z_2}$—the sAIF and filtered proportional controllers do reduce total noise. This indicates that, despite housing the genes on more plasmids yielding higher extrinsic noise, the sAIF controller remains

effective at attenuating noise relative to more comparable open-loop designs (OL 2 and 3). The OL 2 scenario is particularly relevant in practice, as regulating the process through an external actuator component (e.g. transcription factor or chemical inducer) is often necessary and offers greater flexibility in both design and tuning, compared to modifying the promoter that directly drives the process. The corresponding experimental results are presented in Fig. 7(e). Note that the histograms shown in the inset display the distributions for a single instance of each circuit from the scatter plot pointed out in dashed circles, prior to the processing that removes autofluorescence and outliers. This analysis demonstrated that the sAIF controller not only ensures RPA but also decreases noise levels below those found in the open-loop configuration with comparable number of plasmids, i.e. OL 2 and 3, particularly at lower setpoints. Additionally, the data reveal that the noise-reducing capability of the sAIF controller in this example is comparable to that of the filtered-proportional controller.

Lastly, in SI Fig. S12, we include previously published data from Aoki et al.[22], in which an rAIF controller was implemented in *E. coli* using Sigma/anti-Sigma sequestration and successfully achieved RPA at the population level. However, unlike the sAIF controller, the rAIF resulted in a more than fourfold increase in CV relative to its open-loop counterpart. It is important to note that this open-loop circuit also included the controller gene (similar to OL 2), meaning the comparison was not made against a minimal open-loop system without actuator species (i.e. OL 1). Additionally, due to significant differences in experimental setups and genetic parts, our experiment does not attempt a direct comparison between rAIF and sAIF noise levels. Rather, both studies perform relative comparisons within their respective contexts. In our case, the sAIF controller reduces noise at low expression level where noise is prominent compared to its corresponding actuated open-loop configurations (OL 2 and OL 3 in Fig. 7(a)) - a feature that the rAIF controller in[22] did not achieve. However, in this work we have not disentangled topology from part-specific effects. Staging a fair comparison between sAIF and rAIF that takes into account the different parts (such as split inteins and sigma/anti-sigma pairs) and their associated extrinsic noise remains an important future direction.

Discussion

Achieving homeostasis is crucial in regulating cellular processes in living cells, which are inherently noisy and uncertain. While RPA is an important property that endows the system with homeostasis, it is often not sufficient for achieving high dynamic performance. Furthermore, achieving RPA at the population level may come at the cost of high cell-to-cell variability[20] or elevated energetic burden[42]. Therefore, it is vital to develop biomolecular controllers that can deliver both RPA and high performance, taking into account the inherent variability of living cells. While integral controllers are usually the suitable choice to achieve RPA at the population level, proportional controllers are often added on top of the integrators to enhance the dynamic performance and reduce noise or cell-to-cell variability[32,34]. In previous works, such addition was realized by adding extra circuitry which could be biologically demanding, although unavoidable in certain scenarios. In this paper, we have shown that a slight variant of the standard rAIF controller (see the sAIF topology in Fig. 3(a)) gives rise to a (filtered) PI controller without adding the extra circuitry. We also demonstrated analytically and through simulations that this variant indeed brings in the benefits of the proportional controller while maintaining the RPA property offered by the integrator.

The sAIF controller was first introduced in[20] Fig. S1 as one of several realizations of AIF control. More recently, a stochastic analysis employing linear noise approximation was conducted in[42] to show that this variant is capable of reducing noise when controlling a birth-death process. Our study reveals that it is precisely the "hidden" proportional component which is responsible for this noise reduction, and not the integrator. This is demonstrated in Fig. 5 when regulating not only a birth-death process but also a gene expression process with and without protein maturation (see SI Fig. S5). We also demonstrate analytically and through simulations that the "hidden" proportional component not only reduces noise, but also enhances the dynamic performance. Interestingly, this seemingly minor, but subtle, alteration in the choice of the actuating species yields a different controller architecture which tangibly offers better responses. The intuition behind this improvement lies in the fact that the altered choice of actuating species cascades both a filtered proportional controller and an integral controller, resulting in the best of both worlds. This finding has practical implications as it offers a minimal design for biomolecular PI controllers which is easier to build. Furthermore, this minimal design serves as a fundamental principle for constructing negative feedback controllers using a given repressor. As demonstrated in Theorem 1 and supported by theoretical and computational analysis, incorporating sequestration alongside the repressor consistently improves adaptation compromising noise attenuation compared to using the repressor alone.

Leveraging the simple design, we have genetically engineered the sAIF controller in *E. coli* using inteins. We used our previously reported TetR-IntC(Gp41-1)/IntN(Gp41-1) pair[26] for all gene circuits, with no detectable off-target activity. Although we did not perform an extensive characterization of Gp41-1 in this study, this is a widely used and characterized split intein, due to its small size, rapid splicing kinetics, and reliable performance[50–54]. As an added benefit, Gp41-1 is part of a library of orthogonal split inteins validated *in vivo* in *E. coli*[53], supporting its potential for multiplexing, scale up, and incorporation into more complex circuits. Our experimental results successfully demonstrated the controller's capabilities in achieving RPA, favorable transient dynamics and noise reduction. Indeed, our experimen-

tal findings confirm that the sAIF controller is capable of reducing the noise levels below those observed in a parts-matched open-loop configuration where the network is regulated by an actuator. The reduction is clearly observed experimentally at low expression levels where noise is prominent.

Although the previously tested rAIF controller[22] is not directly comparable to our sAIF controller due to differences in biological parts, it is worth noting that it exhibited a more than four-fold increase in noise relative to its own open-loop configuration, which also involved regulation by an actuator species. While not directly comparable, the results are nonetheless informative in assessing the potential of the sAIF architecture. A direct comparison between rAIF and sAIF using matched biological parts remains an important direction for future work.

Our theoretical analysis focused on intrinsic noise, which, while present in our experimental data, is intertwined with extrinsic noise arising from our multi-plasmid design. To account for this additional noise source, we conducted a comprehensive simulation study incorporating intrinsic and extrinsic noise in the form of plasmid copy-number variability (see Fig. 7(d)). The experimental results show that at low expression levels—where noise is most pronounced—the sAIF controller exhibits lower total noise than open-loop circuits that include the actuator (OL2 and OL3), consistent with the simulation results. Two key future directions emerge from this work: (1) designing circuits with measurement modalities capable of disentangling intrinsic and extrinsic noise to study them separately, and (2) embedding controller genes on the same plasmid to reduce variability from plasmid copy number—while carefully avoiding gene interference.

Our theoretical analysis has demonstrated that the choice of actuation mechanisms plays a critical role in facilitating these enhancements. Specifically, degradation-based actuation mechanisms exhibited the best performance in shaping the transient dynamics. Although our genetic implementation, which utilizes TetR as a repressor for actuation, has already shown significant improvements, we anticipate that alternative designs incorporating degradation could unlock even greater enhancements. Exploring these possibilities remains an avenue for future research. Additionally, future work involves testing our controllers in more complex regulatory systems, where unintended interactions and cellular burden may become significant. Although we observed no significant signs of cellular burden—evidenced by the monotonic steady-state responses in SI Fig. S11 and unchanged cell densities indicating no impact on growth rate—burden may still arise when regulating more complex networks. It would also be valuable to experimentally investigate the effects of severe disturbances that could induce integral windup, and to build genetic circuits capable of preventing or mitigating such effects, as proposed in[41].

The first genetically engineered PI controllers in mammalian cells, utilizing sense/anti-sense RNAs, was reported by Frei et al.[27]. Our work introduces the first successful implementation of a PI controller in bacteria, marking a significant milestone. Unlike the previous approach that relied on a proxy for the output molecules to implement proportional control, our sAIF controller employs a minimal design. This design enables the realization of both proportional and integral components through a single actuation reaction, thus avoiding the need for additional genetic parts or proxies.

Our implementation in bacteria underscores the versatility of inteins as a genetic tool applicable across diverse life forms. In fact, the simplicity in the design, coupled with the exquisite role of inteins in bridging theoretical constructs and practical implementations, sets the stage for the promising deployment of such controllers across diverse domains intersecting with synthetic biology. This holds the potential for significant advancements in sectors where precise and swift biomolecular regulation is essential, including biotechnology, metabolic engineering, and cell therapy, among others.

ACKNOWLEDGMENTS

This research was funded in whole or in part by the Swiss National Science Foundation (SNSF) grant no. 216505.

DECLARATION OF INTERESTS

The authors declare no competing interests.

References

1. Yi, T.M., Huang, Y., Simon, M.I., and Doyle, J. (2000). Robust perfect adaptation in bacterial chemotaxis through integral feedback control. Proceedings of the National Academy of Sciences *97*, 4649–4653.

2. Muzzey, D., Gómez-Uribe, C.A., Mettetal, J.T., and van Oudenaarden, A. (2009). A systems-level analysis of perfect adaptation in yeast osmoregulation. Cell *138*, 160–171.

3. El-Samad, H., Goff, J., and Khammash, M. (2002). Calcium homeostasis and parturient hypocalcemia: an integral feedback perspective. Journal of theoretical biology *214*, 17–29.

4. Turrigiano, G. (2007). Homeostatic signaling: the positive side of negative feedback. Current opinion in neurobiology *17*, 318–324.

5. Benner, S.A., and Sismour, A.M. (2005). Synthetic biology. Nature reviews genetics *6*, 533–543.

6. Filo, M., Chang, C.H., and Khammash, M. (2023). Biomolecular feedback controllers: from theory to applications. Current Opinion in Biotechnology *79*, 102882.

7. Barajas, C., and Del Vecchio, D. (2022). Synthetic biology by controller design. Current Opinion in Biotechnology *78*, 102837.

8. Del Vecchio, D., Dy, A.J., and Qian, Y. (2016). Control theory meets synthetic biology. Journal of The Royal Society Interface *13*, 20160380.

9. Hsiao, V., Swaminathan, A., and Murray, R.M. (2018). Control theory for synthetic biology: recent advances in system characterization, control design, and controller implementation for synthetic biology. IEEE Control Systems Magazine *38*, 32–62.

10. Prescott, T.P., and Papachristodoulou, A. (2014). Synthetic biology: A control engineering perspective. In 2014 European Control Conference (ECC). IEEE pp. 1182–1186.

11. Perrino, G., Hadjimitsis, A., Ledesma-Amaro, R., and Stan, G.B. (2021). Control engineering and synthetic biology: working in synergy for the analysis and control of microbial systems. Current Opinion in Microbiology *62*, 68–75.

12. Ruolo, I., Napolitano, S., Salzano, D., di Bernardo, M., and di Bernardo, D. (2021). Control engineering meets synthetic biology: Foundations and applications. Current Opinion in Systems Biology *28*, 100397.

13. Khammash, M.H. (2022). Cybergenetics: Theory and applications of genetic control systems. Proceedings of the IEEE *110*, 631–658.

14. Kotas, M.E., and Medzhitov, R. (2015). Homeostasis, inflammation, and disease susceptibility. Cell *160*, 816–827.

15. Khammash, M.H. (2021). Perfect adaptation in biology. Cell Systems *12*, 509–521.

16. Frei, T., and Khammash, M. (2021). Adaptive circuits in synthetic biology. Current Opinion in Systems Biology *28*, 100399.

17. Xiao, F., and Doyle, J.C. (2018). Robust perfect adaptation in biomolecular reaction networks. In 2018 IEEE conference on decision and control (CDC). IEEE pp. 4345–4352.

18. Francis, B.A., and Wonham, W.M. (1976). The internal model principle of control theory. Automatica *12*, 457–465.

19. Åström, K.J., and Murray, R. (2021). Feedback systems: an introduction for scientists and engineers. Princeton university press.

20. Briat, C., Gupta, A., and Khammash, M. (2016). Antithetic integral feedback ensures robust perfect adaptation in noisy biomolecular networks. Cell systems *2*, 15–26.

21. Hilfinger, A., and Paulsson, J. (2011). Separating intrinsic from extrinsic fluctuations in dynamic biological systems. Proceedings of the National Academy of Sciences *108*, 12167–12172.

22. Aoki, S.K., Lillacci, G., Gupta, A., Baumschlager, A., Schweingruber, D., and Khammash, M. (2019). A universal biomolecular integral feedback controller for robust perfect adaptation. Nature *570*, 533–537.

23. Gupta, A., and Khammash, M. (2022). Universal structural requirements for maximal robust perfect adaptation in biomolecular networks. Proceedings of the National Academy of Sciences *119*, e2207802119.

24. Lillacci, G., Aoki, S., Schweingruber, D., and Khammash, M. (2017). A synthetic integral feedback controller for robust tunable regulation in bacteria. BioRxiv pp. 170951.

25. Huang, H.H., Qian, Y., and Del Vecchio, D. (2018). A quasi-integral controller for adaptation of genetic modules to variable ribosome demand. Nature communications *9*, 5415.

26. Anastassov, S., Filo, M., Chang, C.H., and Khammash, M. (2023). A cybergenetic framework for engineering intein-mediated integral feedback control systems. Nature Communications *14*, 1337.

27. Frei, T., Chang, C.H., Filo, M., Arampatzis, A., and Khammash, M. (2022). A genetic mammalian proportional–integral feedback control circuit for robust and precise gene regulation. Proceedings of the National Academy of Sciences *119*, e2122132119.

28. Mallozzi, A., Fusco, V., Ragazzini, F., and di Bernardo, D. (2024). The crisprator: a biomolecular circuit for automatic gene regulation in mammalian cells with crispr technology. bioRxiv.

29. Filo, M., and Khammash, M. (2019). Optimal parameter tuning of feedback controllers with application to biomolecular antithetic integral control. In 2019 IEEE 58th Conference on Decision and Control (CDC). IEEE pp. 951–957.

30. Olsman, N., Baetica, A.A., Xiao, F., Leong, Y.P., Murray, R.M., and Doyle, J.C. (2019). Hard limits and performance tradeoffs in a class of antithetic integral feedback networks. Cell systems *9*, 49–63.

31. Qian, Y., and Del Vecchio, D. (2018). Realizing 'integral control'in living cells: how to overcome leaky integration due to dilution? Journal of The Royal Society Interface *15*, 20170902.

32. Filo, M., Kumar, S., and Khammash, M. (2022). A hierarchy of biomolecular proportional-integral-derivative feedback controllers for robust perfect adaptation and dynamic performance. Nature communications *13*, 2119.

33. Filo, M., Kumar, S., Anastassov, S., and Khammash, M. (2022). Exploiting the nonlinear structure of the antithetic integral controller to enhance dynamic performance. In 2022 IEEE 61st Conference

on Decision and Control (CDC). IEEE pp. 1294–1299.

34. Briat, C., Gupta, A., and Khammash, M. (2018). Antithetic proportional-integral feedback for reduced variance and improved control performance of stochastic reaction networks. Journal of The Royal Society Interface *15*, 20180079.

35. Chevalier, M., Gómez-Schiavon, M., Ng, A.H., and El-Samad, H. (2019). Design and analysis of a proportional-integral-derivative controller with biological molecules. Cell Systems *9*, 338–353.

36. Samaniego, C.C., and Franco, E. (2021). Ultrasensitive molecular controllers for quasi-integral feedback. Cell Systems.

37. Alexis, E., Cardelli, L., and Papachristodoulou, A. (2022). On the design of a pid bio-controller with set point weighting and filtered derivative action. IEEE Control Systems Letters *6*, 3134–3139.

38. Gupta, A., and Khammash, M. (2019). An antithetic integral rein controller for bio-molecular networks. In 2019 IEEE 58th Conference on Decision and Control (CDC). IEEE pp. 2808–2813.

39. Oyarzún, D.A., and Hancock, E. (2022). Stabilisation of antithetic control via molecular buffering. Journal of The Royal Society Interface.

40. Hancock, E.J., Ang, J., Papachristodoulou, A., and Stan, G.B. (2017). The interplay between feedback and buffering in cellular homeostasis. Cell systems *5*, 498–508.

41. Filo, M., Gupta, A., and Khammash, M. (2024). Anti-windup strategies for biomolecular control systems facilitated by model reduction theory for sequestration networks. Science Advances *10*, eadl5439.

42. Kell, B., Ripsman, R., and Hilfinger, A. (2023). Noise properties of adaptation-conferring biochemical control modules. Proceedings of the National Academy of Sciences *120*, e2302016120.

43. Anastassov, S., Filo, M., and Khammash, M. (2024). Inteins: A swiss army knife for synthetic biology. Biotechnology Advances pp. 108349.

44. Gogarten, J.P., Senejani, A.G., Zhaxybayeva, O., Olendzenski, L., and Hilario, E. (2002). Inteins: structure, function, and evolution. Annual Reviews in Microbiology *56*, 263–287.

45. Wang, H., Wang, L., Zhong, B., and Dai, Z. (2022). Protein splicing of inteins: a powerful tool in synthetic biology. Frontiers in Bioengineering and Biotechnology *10*, 810180.

46. Gillespie, D.T. (1977). Exact stochastic simulation of coupled chemical reactions. The journal of physical chemistry *81*, 2340–2361.

47. Castillo-Hair, S.M., Sexton, J.T., Landry, B.P., Olson, E.J., Igoshin, O.A., and Tabor, J.J. (2016). Flowcal: a user-friendly, open source software tool for automatically converting flow cytometry data from arbitrary to calibrated units. ACS synthetic biology *5*, 774–780.

48. Gerhardt, K.P., Rao, S.D., Olson, E.J., Igoshin, O.A., and Tabor, J.J. (2021). Independent control of mean and noise by convolution of gene expression distributions. Nature Communications *12*, 6957.

49. Shao, B., Rammohan, J., Anderson, D.A., Alperovich, N., Ross, D., and Voigt, C.A. (2021). Single-cell measurement of plasmid copy number and promoter activity. Nature communications *12*, 1475.

50. Carvajal-Vallejos, P., Pallissé, R., Mootz, H.D., and Schmidt, S.R. (2012). Unprecedented rates and efficiencies revealed for new natural split inteins from metagenomic sources. Journal of Biological Chemistry *287*, 28686–28696.

51. Palanisamy, N., Degen, A., Morath, A., Ballestin Ballestin, J., Juraske, C., Öztürk, M.A., Sprenger, G.A., Youn, J.W., Schamel, W.W., and Di Ventura, B. (2019). Split intein-mediated selection of cells containing two plasmids using a single antibiotic. Nature communications *10*, 4967.

52. Yao, Z., Aboualizadeh, F., Kroll, J., Akula, I., Snider, J., Lyakisheva, A., Tang, P., Kotlyar, M., Jurisica, I., Boxem, M. et al. (2020). Split intein-mediated protein ligation for detecting protein-protein interactions and their inhibition. Nature communications *11*, 2440.

53. Pinto, F., Thornton, E.L., and Wang, B. (2020). An expanded library of orthogonal split inteins enables modular multi-peptide assemblies. Nature Communications *11*, 1529.

54. Shepherd, C., Lawson-Williams, M., Holland, A., Bello, A.J., Sexton, D.W., and Olorunniji, F.J. (2025). Conditional split inteins: Adaptable tools for programming protein functions. International Journal of Molecular Sciences *26*, 586.

55. Potapov, V., Ong, J.L., Kucera, R.B., Langhorst, B.W., Bilotti, K., Pryor, J.M., Cantor, E.J., Canton, B., Knight, T.F., Evans Jr, T.C. et al. (2018). Comprehensive profiling of four base overhang ligation fidelity by t4 dna ligase and application to dna assembly. ACS synthetic biology *7*, 2665–2674.

56. Marillonnet, S., and Grützner, R. (2020). Synthetic dna assembly using golden gate cloning and the hierarchical modular cloning pipeline. Current protocols in molecular biology *130*, e115.

57. Lou, C., Stanton, B., Chen, Y.J., Munsky, B., and Voigt, C.A. (2012). Ribozyme-based insulator parts buffer synthetic circuits from genetic context. Nature biotechnology *30*, 1137–1142.

58. Bindels, D.S., Haarbosch, L., Van Weeren, L., Postma, M., Wiese, K.E., Mastop, M., Aumonier, S., Gotthard, G., Royant, A., Hink, M.A. et al. (2017). mscarlet: a bright monomeric red fluorescent protein for cellular imaging. Nature methods *14*, 53–56.

59. Lutz, R., and Bujard, H. (1997). Independent and tight regulation of transcriptional units in escherichia coli via the lacr/o, the tetr/o and arac/i1-i2 regulatory elements. Nucleic acids research *25*, 1203–1210.

60. Romano, E., Baumschlager, A., Akmeric, E.B., Palanisamy, N., Houmani, M., Schmidt, G., Öztürk, M.A., Ernst, L., Khammash, M., and Di Ventura, B. (2021). Engineering arac to make it responsive to light instead of arabinose. Nature chemical biology *17*, 817–827.

61. Chung, C., Niemela, S.L., and Miller, R.H. (1989). One-step preparation of competent escherichia coli: transformation and storage of bacterial cells in the same solution. Proceedings of the National Academy of Sciences *86*, 2172–2175.

62. Baumschlager, A., Aoki, S.K., and Khammash, M. (2017). Dynamic blue light-inducible t7 rna polymerases (opto-t7rnaps) for precise spatiotemporal gene expression control. ACS synthetic biology *6*, 2157–2167.

63. Galbusera, L., Bellement-Theroue, G., Urchueguia, A., Julou, T., and van Nimwegen, E. (2020). Using fluorescence flow cytometry data for single-cell gene expression analysis in bacteria. PloS one *15*, e0240233.

STAR METHODS

Growth Conditions

Escherichia coli cells were grown in M9 medium supplemented with 0.2% casamino acids, 0.4% glucose, 0.001% thiamine, 0.00006% ferric citrate, 0.1 mM calcium chloride, 1 mM magnesium sulfate, and 20 µg/mL uracil (Sigma-Aldrich Chemie GmbH), and incubated in an environmental shaker (New Brunswick) at 37°C with shaking at 230 rpm. Antibiotics (Sigma-Aldrich Chemie GmbH) were used at the following concentrations: carbenicillin (carb), 100 µg/mL; spectinomycin (spec), 100 µg/mL; chloramphenicol (cam), 34 µg/mL.

E. coli Host Strain

Host strain SKA360 (MG1655 *ΔaraCBAD ΔlacIZYA ΔaraE ΔaraFGH attB::lacYA177C ΔrhaSRT ΔrhaBADM*) is a precursor strain to SKA703 constructed as previously described in[22].

E. coli Plasmids

All plasmids (Table S1) were constructed from a custom-made library of parts with optimized overhangs[55] using standard Golden-Gate assembly methods and modular cloning (MoClo)[56] with restriction enzymes BsaI-HF v2 and BbsI-HF (New England Biolabs). Circuit modules were split between three different plasmids. The Gene 1 plasmids contain either *intC(gp41-1)* or *intN(gp41-1)*[26,50] under a Bba_J23119 constitutive promoter and weak B0033 ribosomal binding site (RBS) from the Registry of Standard Biological Parts on a medium copy plasmid with p15A origin of replication and aminoglycoside adenylyltransferase ($spec^R$) gene. The Gene 2 TetR-IntC plasmids consist of a *tetR(1-183)::intC(gp41-1)::tetR(184-212)* fusion[26] under the control of either a modified P_{araB} promoter[22] and weak B0033 RBS or AraJ-B0033m ribozyme/RBS (for the weak and strong filtered proportional and sAIF circuits, respectively)[57] or a Bba_J23111 or Bba_J23119 constitutive promoter from the Registry of Standard Biological Parts (for the weak and strong open-loop circuits, respectively) and weak B0033 RBS on a low copy plasmid with pSC101 origin of replication and chloramphenicol-acyltransferanse (cam^R) gene. The regulated Gene 3 output plasmid consists of a *V5::araC::mScarlet-I* fusion[22,58] under the control of a $P_{LtetO-1}$ promoter[59] and weak B0033 RBS on a high copy plasmid with ColE1 origin of replication and beta-lactamase (carbR) gene. Additionally, a set of unregulated Gene 3 output plasmids with *V5::araC::mScarlet-I* under a weak B0033 RBS and constitutive promoters Bba_J23114, Bba_J23106, Bba_J23102, Bba_J23111, Bba_J23119 from the Registry of Standard Biological Parts as well as J23101*, a modified weaker variant of Bba_J23101*[60] were constructed using the same backbone as the regulated Gene 3 output plasmid. Plasmids were transformed into *E. coli* host strain SKA360 for testing as previously described[61]. The plasmid combinations used for each circuit are listed in Table S2. Plasmid sequences are available at the following Github repository https://github.com/Maurice-Filo/Sensor-Based-Biomolecular-Integral-Controllers.

E. coli Steady-State Experiments

200 µl aliquots of M9 medium in 96-well flat-bottom plates (Greiner) with appropriate antibiotics were inoculated with the circuit strains from glycerol freeze stocks. The plates were covered with BreathSeal film (Greiner) and a plastic lid (Greiner) and were incubated overnight at 37°C with shaking to stationary phase. In the morning, cultures were diluted 1:1,200,000 in fresh 200 µl aliquots of M9 medium in 96-well flat-bottom plates containing arabinose (Sigma-Aldrich) at final concentrations of 0%, 0.2%, 0.35%, 0.5%, 0.75%, 1%, 1.5%, or 2% with or without 0.5 ng/mL anhydrotetracycline (aTc, Chemie Brunschwig). Plates were covered with BreathSeal film and plastic lids and incubated for six hours at 37°C with shaking. After six hours of shaking, all cultures were in exponential phase (optical density at 600 nm (OD) less

than 0.1). As previously described, cell growth, transcription, and translation were stopped with a rifampicin-tetracycline solution and the mScarlet-I was matured for three hours at 37°C[62]. Matured samples were stored at 4°C overnight and samples were measured by flow cytometry on a CytoFlex S (Beckman Coulter) the next day with a minimum of 50,000 events recorded. As a no-fluorescence control, host strain SKA360 was cultured, processed, and measured in parallel with the other samples. Rainbow calibration beads (Spherotech, RCP-30-5A) were also measured in the same run as each experiment with a minimum of 50,000 events collected.

Open loop 2 (OL 2), open loop 3 (OL 3), filtered proportional (fP), and sensor-based Antithetic Integral Feedback (sAIF) circuits were tested together in parallel, along with a no-fluorescence control (empty host strain SKA360) and rainbow calibration beads (Spherotech, RCP-30-5A), to ensure that all circuits were assayed under identical conditions and could be directly compared within each experiment. Single-plasmid experiments using open loop 1 (OL 1) were performed separately in M9 medium without arabinose or aTc along with the no-fluorescence control and rainbow calibration beads. All experiments were performed on three independent days (biological replicates). Each OL 2, OL 3, fP, and sAIF circuit experiment included one sample per strain and condition, whereas OL 1 experiments were conducted with three technical replicates. Corresponding data are shown in Figures 7(c) and 7(e).

E. coli Dynamic Experiments

For this experiment, it was important that the cells were kept in exponential phase. A 3 mL aliquot of M9 medium containing appropriate antibiotics and 0.5% arabinose was inoculated with cells from glycerol freeze stocks at a low OD so that after approximately 10 hours of incubation overnight at 37°C and 230 rpms, cultures were at an OD between 0.01 and 0.03. The exponential phase culture was then used to start pseudo-time course experiments. Briefly, the time courses were split into two phases. The first phase was one hour of growth in 0.5% arabinose to ensure that the cultures were at steady-state and to assess the output level without any disturbance. The second phase was six additional hours of growth in 0.5% arabinose with or without a constant 0.5 ng/mL aTc disturbance. Cultures for time points 0-1 h were set up simultaneously and sampled every 30 minutes. After 1 h of growth, cultures for time points 1.5-7 h (with and without aTc) were set up simultaneously and sampled every 30 minutes. After collecting all the time points, mScarlet-I was matured for all the samples at the same time and matured samples were measured at the same time on the flow cytometer.

Dilution strategy for time points 0 -1h

The overnight exponential culture was diluted to an OD of 0.006 in 1.2 ml M9-0.5% arabinose. This initial 0.006 OD dilution mix was used to inoculate 200 µl of M9-0.5% arabinose in column 2 of a 96-well flat-bottom plate (Greiner) with one row per circuit strain (Plate 1). The remaining dilution mix was further diluted 2.3-fold in M9-0.5% arabinose and 200 µl aliquots of cells were aliquoted in columns 3-5 of the same 96-well plate. Empty wells were filled with 200 µl PBS and the plate was covered with a BreathSeal film and plastic lid and incubated at 37°C with shaking.

Dilution strategy for time points 1-7h

For the no disturbance (0 ng/mL aTc) condition, 96-well Plates 2 and 3 were prepared by aliquoting 200 µl M9-0.5% arabinose into Plate 2 columns 2-11 and Plate 3 columns 2-3. For the disturbance (0.5 ng/mL aTc) conditions, Plates 4 and 5 were prepared by aliquoting 200 µl M9-0.5% arabinose-0.9375 ng/ml aTc into Plate 4 column 2 and 200 µl M9-0.5% arabinose-0.5 ng/ml aTc into Plate 4 columns 3-11 and Plate 5 columns 2-3. At time 1 h, Plate 1 columns 4 and 5 were combined together and used to inoculate the 200 µl aliquots of media in Plate 2 and Plate 4 column 2 with 175 µl culture (2.3-fold dilution). The wells were pipetted up and down to mix and 175 µl was transferred to the 200 µl of media in column 3 of the same plate. This serial dilution procedure was continued for the remaining columns of Plates 2 and 4. 175 µl of diluted culture in column 11 of Plates 2 and 4 were then used to continue the serial dilutions into Plates 3 and 5 column 2, respectively.

Sample collection, mScarlet-I maturation and measurement

The experimental protocol was set up so that each column was one 30 minute time point. For each time point, 100 µl of culture was collected and mixed with 100 µl rifampicin-tetracycline solution in 96-well plates on ice to stop cell growth, transcription, and translation[62]. Plates were kept on ice in the dark until all time points were sampled. After sampling the last point, the plates were kept on ice for one hour before covering with a BreathSeal film and maturing the mScarlet-I for three hours at 37°C. Matured samples were stored at 4°C overnight and samples were measured on a CytoFlex S the next day with a minimum of 20,000 events recorded. Time 0 h was collected from leftover dilution mix used to inoculate Plate 1. Time 0.5 h was from Plate 1 column 2. Time 1h was from Plate 1 column 3. Time 1.5-6 h was from Plates 2 and 4 starting with column 2 and ending with column 11 (one column per 30 minutes). Time 6.5-7 h was from Plates 3 and 5 starting with column 2 and ending with column 3 (one column per 30 minutes).As a no-fluorescence control, host strain SKA360 was cultured, processed, and measured at time 7h in parallel with the other samples. Rainbow calibration beads (Spherotech, RCP-30-5A) were also measured in the same run as each experiment with a minimum of 50,000 events collected.

Flow Cytometry

All samples were measured on a CytoFlex S flow cytometer (Beckman Coulter) equipped with a 96-well plate sample loader using CytExpert version 2.4.0.28. mScarlet-I was measured with a 561 nm lasesr and 610/20 bandpass filter (ECD-H); the gain settings were as follows: forward scatter 100, side scatter 100, mScarlet-I 1000. Thresholds of 2,500 FSC-H and 1,000 SSC-H were used for all samples.

Data Analysis

All flow cytometry files were processed using the python package FlowCal as previously described[47]. Briefly, events were gated by SSC-H and FSC-H using a gate fraction of 0.3. mScarlet-I fluorescence (ECD-H) was then converted to Molecules of Equivalent Fluorochrome (MEF) using Rainbow calibration bead (Spherotech, RCP30-5A) measurements performed on the same day as each experiment.

The arithmetic mean and variance of the cell populations was calculated using the Python package NoiseControl as previously described[48].

Briefly, the python script first trims the FlowCal-processed data to remove a small number of outliers. Trimming is based on a kernel density estimate of the log-fluorescence distribution, used to identify the fluorescence range around the median where the density exceeds a 0.5% threshold. Then, the script subtracts autofluorescence, obtained from the untransformed host strain SKA360 measure on the same day as each experiment, as follows

$$\begin{aligned}\mathbb{E}[Y] &= \mathbb{E}[Y_{\text{tot}}] - \mathbb{E}[Y_{\text{af}}] \\ \text{CV}[Y] &= \frac{\sqrt{\text{CV}[Y_{\text{tot}}]^2\,\mathbb{E}[Y_{\text{tot}}]^2 - \text{CV}[Y_{\text{af}}]^2\,\mathbb{E}[Y_{\text{af}}]^2}}{\mathbb{E}[Y_{\text{tot}}] - \mathbb{E}[Y_{\text{af}}]},\end{aligned}$$

where Y_{af} is the autofluorescence and Y_{tot} is the total fluorescence. We also analyzed our data using a different pipeline[63] and the conclusions remained unchanged.

All experimental data was plotted in Python while computational simulations were carried out and plotted in MATLAB.

Code Availability

The MATLAB and Python codes generated in this study can be found at the following Github repository https://github.com/Maurice-Filo/Sensor-Based-Biomolecular-Integral-Controllers.

Engineering Sensor-Based Antithetic Integral Controllers for Enhanced Dynamic Performance and Noise Attenuation

Maurice Filo[1,2], Stephanie K. Aoki[1,2], Mucun Hou[1,2], Stanislav Anastassov[1], and Mustafa Khammash[1,*]

[1]Department of Biosystems Science and Engineering, ETH Zürich, 4056 Basel, Switzerland
[2]These authors contributed equally
[*]Correspondence: mustafa.khammash@bsse.ethz.ch

Contents

List of Figures

List of Tables

S1 Transfer Functions

Let $(\bar{x}, \bar{z}_1, \bar{z}_2)$ denote the closed-loop fixed point when operating at a nominal exogenous input $\bar{\mu}$. Furthermore, let $(\tilde{x}, \tilde{z}_1, \tilde{z}_2)$ denote the perturbation from the closed-loop fixed point due to a disturbance or a perturbation $\tilde{\mu}$ of the exogenous input from its nominal value. That is, we have

$$\mu(t) = \bar{\mu} + \tilde{\mu}(t); \qquad x(t) = \bar{x} + \tilde{x}(t); \qquad z_i(t) = \bar{z}_i + \tilde{z}_i(t), \tag{S1}$$

for $i = 1, 2$. Let $\hat{x}, \hat{z}_1, \hat{z}_2, \hat{\mu}$ and $\hat{u}$ respectively denote the Laplace transforms of $\tilde{x}, \tilde{z}_1, \tilde{z}_2, \tilde{\mu}$ and $\tilde{u}$. For the actuation function h, define the partial derivatives as $\partial h(\bar{z}_1, \bar{z}_2, \bar{x}_L; \bar{x}_1) \triangleq \begin{bmatrix}\sigma_1 & -\sigma_2 & -\sigma_L & \sigma_x\end{bmatrix}$ with $\sigma_1, \sigma_2, \sigma_L \geq 0$, and let e_i be a vector of an appropriate size whose entries are all zeros except the i^{th}-entry being 1.

S1.1 Proportional & Feedforward Controllers

Consider the following closed-loop dynamics

$$\begin{cases} \dot{x} = f(x) + ue_1 \\ \dot{z}_1 = \mu - \delta' z_1 \\ \dot{z}_2 = \theta x_L - \delta z_2, \end{cases} \tag{S2}$$

where the control action is given as $u = h(z_1, z_2, x_L; x_1)$ to encompass the two basic controller motifs listed in Fig. 2(c) and an additional controller where $\mathbf{X_L}$ directly actuates $\mathbf{X_1}$ since now h is allowed to, more generally, depend on x_L. The approximated perturbation dynamics are thus given by the linearization that can be written separately for the process $\mathcal{P}$ and the controller $\mathcal{C}$ as

$$\begin{aligned} \mathcal{P}: \quad & \dot{\tilde{x}} = \underbrace{\left[\partial f(\bar{x}) + \sigma_x e_1 e_1^T\right]}_{A_p} \tilde{x} + \tilde{u} e_1 \\ \mathcal{C}: \quad & \begin{bmatrix}\dot{\tilde{z}}_1 \\ \dot{\tilde{z}}_2\end{bmatrix} = \underbrace{\begin{bmatrix}-\delta' & 0 \\ 0 & -\delta\end{bmatrix}}_{A_c} \begin{bmatrix}\tilde{z}_1 \\ \tilde{z}_2\end{bmatrix} + \underbrace{\begin{bmatrix}0 & 1 \\ \theta & 0\end{bmatrix}}_{B_c} \begin{bmatrix}\tilde{x}_L \\ \tilde{\mu}\end{bmatrix} \\ & \tilde{u} = \underbrace{\begin{bmatrix}\sigma_1 & -\sigma_2\end{bmatrix}}_{C_c} \begin{bmatrix}\tilde{z}_1 \\ \tilde{z}_2\end{bmatrix} + \underbrace{\begin{bmatrix}-\sigma_L & 0\end{bmatrix}}_{D_c} \begin{bmatrix}\tilde{x}_L \\ \tilde{\mu}\end{bmatrix}, \end{aligned} \tag{S3}$$

where, for convenience and with a slight abuse of notation, σ_x is absorbed in the dynamics of the process and so $\tilde{u}$ does not involve $\tilde{x}_1$. Taking the Laplace transforms on both sides of the equalities in Equation (S3) and recalling that the transfer matrix of the controller is $C_c(sI - A_c)^{-1}B_c + D_c$ yields the following transfer functions

$$\begin{aligned} \mathcal{P}: \quad & \hat{x}_L(s) = P(s)\hat{u}(s) \triangleq e_L^T(sI - A_p)^{-1}e_1\hat{u}(s) \\ \mathcal{C}: \quad & \hat{u}(s) = K_F \frac{\omega_0'}{s + \omega_0'}\hat{\mu}(s) - \left[K_P \frac{\omega_0}{s + \omega_0} + K_P'\right]\hat{x}_L(s), \end{aligned} \tag{S4}$$

where

$$K_F \triangleq \frac{\sigma_1}{\delta'}, \qquad K_P \triangleq \frac{\sigma_2 \theta}{\delta}, \qquad K_P' \triangleq \sigma_L, \qquad \omega_0 \triangleq \delta, \qquad \omega_0' \triangleq \delta'.$$

As a result, the two cases presented in Fig. 2(c) can be directly obtained from Equation (S4) by choosing the control action $u = h(z_1, z_2, x_L; x_1)$ appropriately which leads to setting a subset of the partial derivatives $\sigma_1, \sigma_2, \sigma_L$ and σ_x to zero.

S1.2 Proportional-Integral Controllers

Consider the following closed-loop dynamics

$$\begin{cases} \dot{x} = f(x) + ue_1 \\ \dot{z}_1 = \mu - \eta z_1 z_2 \\ \dot{z}_2 = \theta x_L - \eta z_1 z_2, \end{cases} \tag{S5}$$

where the control action is given as $u = h(z_1, z_2, x_L; x_1)$ to encompass the two cases presented in Fig. 3(a) and (b), and an additional controller where $\mathbf{X_L}$ directly actuates $\mathbf{X_1}$ since now h is allowed to, more generally, depend on x_L.

The approximated perturbation dynamics are thus given by the linearization that can be written separately for the process $\mathcal{P}$ and the controller $\mathcal{C}$ as

$$\begin{aligned}
\mathcal{P}: \quad & \dot{\tilde{x}} = \underbrace{\left[\partial f(\bar{x}) + \sigma_x e_1 e_1^T\right]}_{A_p} \tilde{x} + \tilde{u} e_1 \\
\mathcal{C}: \quad & \begin{bmatrix} \dot{\tilde{z}}_1 \\ \dot{\tilde{z}}_2 \end{bmatrix} = \underbrace{\begin{bmatrix} -\eta\bar{z}_2 & -\eta\bar{z}_1 \\ -\eta\bar{z}_2 & -\eta\bar{z}_1 \end{bmatrix}}_{A_c} \begin{bmatrix} \tilde{z}_1 \\ \tilde{z}_2 \end{bmatrix} + \underbrace{\begin{bmatrix} 0 & 1 \\ \theta & 0 \end{bmatrix}}_{B_c} \begin{bmatrix} \tilde{x}_L \\ \tilde{\mu} \end{bmatrix} \\
& \tilde{u} = \underbrace{\begin{bmatrix} \sigma_1 & -\sigma_2 \end{bmatrix}}_{C_c} \begin{bmatrix} \tilde{z}_1 \\ \tilde{z}_2 \end{bmatrix} + \underbrace{\begin{bmatrix} -\sigma_L & 0 \end{bmatrix}}_{D_c} \begin{bmatrix} \tilde{x}_L \\ \tilde{\mu} \end{bmatrix},
\end{aligned} \tag{S6}$$

where, for convenience and with a slight abuse of notation, σ_x is absorbed in the dynamics of the process and so $\tilde{u}$ does not involve $\tilde{x}_1$. Taking the Laplace transforms on both sides of the equalities in Equation (S6) and recalling that the transfer matrix of the controller is $C_c(sI - A_c)^{-1}B_c + D_c$ yields the following transfer functions

$$\begin{aligned}
\mathcal{P}: \quad & \hat{x}_L(s) = P(s)\hat{u}(s) = e_L^T(sI - A_p)^{-1}e_1\hat{u}(s) \\
\mathcal{C}: \quad & \hat{u}(s) = \left[\frac{K_I}{s}\hat{e}(s) + K_F\hat{\mu}(s) - K_P K_S \hat{x}_L(s)\right] \frac{\omega_0}{s+\omega_0} - K_p'\hat{x}_L(s),
\end{aligned} \tag{S7}$$

where

$$\begin{cases}
K_I \triangleq \dfrac{\sigma_1\bar{z}_1 + \sigma_2\bar{z}_2}{\bar{z}_1 + \bar{z}_2}, & K_F \triangleq \dfrac{\sigma_1}{\eta(\bar{z}_1 + \bar{z}_2)}, \quad K_P' \triangleq \sigma_L, \\
K_P \triangleq \dfrac{\sigma_2}{\eta(\bar{z}_1 + \bar{z}_2)}, & \omega_0 \triangleq \eta(\bar{z}_1 + \bar{z}_2), \quad K_S \triangleq \theta.
\end{cases} \tag{S8}$$

As a result, the two cases presented in Fig. 3 can be directly obtained from Equation (S7) by choosing the control action $u = h(z_1, z_2, x_L; x_1)$ appropriately which leads to setting a subset of the partial derivatives $\sigma_1, \sigma_2, \sigma_L$ and σ_x to zero.

S2 Mappings between Filtered PI and Biomolecular Parameters

Throughout the subsequent analysis, we will make an assumption about the process. Let F_i $(i = 1, 2, ..., L)$ denote the steady-state maps of the process, that is, if u is a constant then with reference to the first equation in Equation (S5), we write

$$f(x) + ue_1 = 0 \qquad \Longrightarrow \qquad x_i = F_i(u). \tag{S9}$$

Assumption 1. *Assume that for the desired steady-state output $\bar{x}_L = r$, there exists a feasible supporting input $\bar{u}$ and steady-state concentrations of the process species $\bar{x}_i, i = 1, \cdots, L-1$, that achieve the desired output. More precisely, for $r > 0, \exists \bar{u} \in \mathbb{U}$ and $\bar{x}_i \geq 0$ such that $F_L(\bar{u}) = r$ and $\bar{x}_i = F_i(\bar{u})$, where $\mathbb{U}$ is the set of feasible inputs.*

Remark 1. *The set of feasible inputs depends on the type of actuation. For instance if the actuation is carried out via non-saturating production only, then $\mathbb{U} = \mathbb{R}_+$; whereas if it is carried out via non-saturating degradation only, then $\mathbb{U} = \mathbb{R}_-$. If both non-saturating production and degradation actuations are allowed then, $\mathbb{U} = \mathbb{R}$.*

Remark 2. *We emphasize that this assumption does not depend on the type of controller used. Instead, it only depends on the process and the particular choice of actuated input species and actuation mechanism. This assumption has to be satisfied, otherwise, the actuation is simply inadequate and there is no controller that can achieve the desired output without changing the choice of the actuated input species and/or actuation mechanism.*

The set of formulas in Equation (S8) provides a way to calculate the block diagram parameters (see Fig. 3(b)) from the biomolecular parameters. To go in the opposite direction, one can solve Equation (S8) for the biomolecular parameters to obtain

$$\begin{cases}
\eta = \dfrac{1}{\mu}\dfrac{(K_I - \omega_0 K_F)(\omega_0 K_P - K_I)}{(K_P - K_F)^2}; \\
\sigma_1 = \omega_0 K_F; \quad \sigma_2 = \omega_0 K_P; \quad \sigma_L = K_P'; \\
h(\bar{z}_1, \bar{z}_2, \bar{x}_L; \bar{x}_1) = \bar{u},
\end{cases} \tag{S10}$$

where $\bar{z}_1 = \mu\frac{K_P - K_F}{K_I - \omega_0 K_F}$, $\bar{z}_2 = \mu\frac{K_P - K_F}{\omega_0 K_P - K_I}$ and $\bar{u}$ is fixed (it depends on the process and setpoint only). Of course whether this inversion is doable or not depends on the number of degrees of freedom that shape the actuation function h.

Our goal is to derive the mappings between the Filtered PI parameters (K_P, K_I, ω_0) and the various biomolecular parameters $(\eta, ...)$. We first start with the analysis problem: given the biomolecular parameters, what are the PI gains and cutoff frequency? Then we move to the design problem: what are the biomolecular parameters that achieve some desired PI gains and cutoff frequency? We treat the analysis and design problems for the rAIF controller and the sAIF controller with two biologically-relevant functional forms of h implementing the two negative actuation mechanisms (production and removal) shown in Fig. 2(b).

S2.1 Mappings for rAIF Controllers

For rAIF with $h(z_1, z_2, x_L; x_1) = kz_1$, we have $K_P = K_P' = 0$ and for a fixed μ and θ, the mappings back and forth between the block diagram and biomolecular parameters are given by

$$\begin{cases} \textbf{Analysis:} & K_I = \dfrac{k\bar{z}_1}{\bar{z}_1 + \bar{z}_2}, \quad \omega_0 = \eta(\bar{z}_1 + \bar{z}_2) \\ \textbf{Design:} & \eta = \dfrac{\omega_0 K_I}{\bar{u}}, \quad k^{\pm} = \dfrac{\bar{u}}{\mu}\dfrac{\omega_0}{2}\left[1 \mp \sqrt{1 - 4\dfrac{\mu}{\bar{u}}\dfrac{K_I}{\omega_0}}\right], \end{cases} \tag{S11}$$

Observe that K_F is left out on purpose because with this actuation function K_F is not a degree of freedom (unless μ or θ are allowed to be tuned). Furthermore, since k has to be a nonnegative real number, then the following condition constrains the coverage of the integral gain and cutoff frequency:

$$K_I \leq \frac{\bar{u}}{4\mu}\omega_0. \tag{S12}$$

S2.2 Mappings for sAIF Controllers

For sAIF, we have $K_F = K_P' = 0$ since h is not a function of z_1; instead it is a monotonically decreasing function of z_2. We consider actuations via repression and degradation separately.

Actuation via Repression

The actuation function h is given here as a Hill-type function with cooperativity, that is

$$u = h(z_2; x_1) = \frac{\alpha}{1 + (z_2/\kappa)^n}, \tag{S13}$$

where κ is the dissociation constant, α is the maximal production rate and n is the Hill coefficient. The setpoint is given by $\bar{x}_L = r \triangleq \mu/\theta$. For a given process and setpoint r, satisfying Assumption 1, the supporting input $\bar{u}$ satisfies $F_L(\bar{u}) = r$ and is fixed. We first treat the analysis problem, then move on to the design problem.

Analysis. The controller coordinates $(\bar{z}_1, \bar{z}_2)$ of the fixed point are given by

$$\bar{z}_1 = \frac{\mu}{\eta\kappa\sqrt[n]{\frac{\alpha}{\bar{u}} - 1}}, \qquad \bar{z}_2 = \kappa\sqrt[n]{\frac{\alpha}{\bar{u}} - 1}. \tag{S14}$$

Clearly, the following condition on the biomolecular parameters has to be satisified to guarantee that $\bar{z}_1, \bar{z}_2 > 0$,

$$\alpha > \bar{u}. \tag{S15}$$

Violating this condition causes both coordinates of the fixed point to become either negative or complex and thus causing instability. By substituting the partial derivatives of the actuation function $\sigma_1 = \sigma_L = \sigma_x = 0$ in Equation (S8), one can write the PI gains (K_P, K_I) and cutoff frequency ω_0 in terms of the various biochemical parameters as

$$K_I = \frac{\sigma_2\bar{z}_2}{\bar{z}_1 + \bar{z}_2}, \quad K_P = \frac{\sigma_2}{\eta(\bar{z}_1 + \bar{z}_2)}, \quad \omega_0 = \eta(\bar{z}_1 + \bar{z}_2). \tag{S16}$$

where $\sigma_2 = n\frac{\bar{u}^2}{\alpha\kappa}\left(\frac{\bar{z}_2}{\kappa}\right)^{n-1}$.

Design. By fixing μ and r (and thus $\bar{u}$), one can easily solve the equations given in Equation (S14) and Equation (S16) for the biomolecular parameters α, κ, and η in terms of the PI gains and cutoff frequency to obtain

$$\eta = \frac{1}{\mu}\frac{K_I}{K_P}\left(\omega_0 - \frac{K_I}{K_P}\right), \quad \alpha = \frac{\bar{u}}{1 - \frac{\mu}{n\bar{u}}\frac{\omega_0 K_P}{\omega_0 - \frac{K_I}{K_P}}}, \quad \kappa = \frac{\mu}{\omega_0 - \frac{K_I}{K_P}}\sqrt[n]{n\frac{\bar{u}}{\mu}\frac{\omega_0 - \frac{K_I}{K_P}}{\omega_0 K_P} - 1}. \tag{S17}$$

Filtered-PI Coverage. Constraining α, κ and η to be non-negative and to satisfy condition Equation (S15) yields the following achievable PI gains and cutoff frequency.

$$\mathcal{S}_r^n = \left\{ (K_P, K_I, \omega_0) \in \mathbb{R}_+^3 : K_P < n\tfrac{\bar{u}}{\mu},\ K_I < \omega_0 K_P \left(1 - \tfrac{\mu K_P}{n\bar{u}}\right) \right\}. \tag{S18}$$

This indicates that employing repression for negative actuation imposes an upper bound on both the proportional gain K_P and integral gain K_I. It is worth noting that these upper bounds can be relaxed by increasing n since $\mathcal{S}_r^n \subset \mathcal{S}_r^{n+1}$, suggesting that cooperativity enhances the coverage, thereby enabling more flexible tuning of the filtered PI parameters. Lastly, it is important to highlight that the upper bound of K_I depends not only on the process and the setpoint via the supporting input $\bar{u}$, but also on the proportional gain K_P and cutoff frequency ω_0.

Actuation via Degradation

Next, consider the case where $\mathbf{Z_2}$ degrades the input species $\mathbf{X_1}$. The actuation function h is thus given by

$$u = h(z_2; x_1) = \alpha - \gamma \bar{z}_2 \xi(x_1), \tag{S19}$$

where $\xi(x_1) = \frac{\bar{x}_1}{\bar{x}_1 + \kappa_x}$. The controller coordinates $(\bar{z}_1, \bar{z}_2)$ of the fixed point are

$$\bar{z}_1 = \frac{\mu\gamma\xi(\bar{x}_1)}{\eta(\alpha - \bar{u})}, \qquad \bar{z}_2 = \frac{\alpha - \bar{u}}{\gamma\xi(\bar{x}_1)}, \tag{S20}$$

with $\xi(\bar{x}_1) \triangleq \frac{\bar{x}_1}{\bar{x}_1 + \kappa_x} \approx 1$, by choosing κ_x to be small for simplicity. Note that this assumption can be easily relaxed. Calculations of the analysis problem are similar to the repression case but with $\sigma_2 = \gamma\xi(\bar{x}_1) \approx \gamma$. The mappings from the PI gains (K_P, K_I) and the cutoff frequency ω_0 to the biomolecular parameters are given by

$$\eta = \frac{1}{\mu}\frac{K_I}{K_P}\left(\omega_0 - \frac{K_I}{K_P}\right), \quad \alpha \approx \bar{u} + \mu\frac{\omega_0 K_P}{\omega_0 - \frac{K_I}{K_P}}, \quad \gamma \approx \omega_0 K_P. \tag{S21}$$

Constraining the biomolecular parameters to be non-negative yields the following achievable PI parameters,

$$\mathcal{S}_d = \left\{ (K_P, K_I, \omega_c) \in \mathbb{R}_+^3 : K_I < \omega_0 K_P \right\}. \tag{S22}$$

This indicates that employing degradation for negative actuation, imposes an upper bound on the integral gain K_I only. Furthermore, this bound is less restrictive than that corresponding to the actuation via repression. In fact, observe that for all $n = 1, 2, \cdots$, we have $\mathcal{S}_r^n \subset \mathcal{S}_r^{n+1} \subset \mathcal{S}_d$ as visually demonstrated in SI Fig. S2. Also note that $\mathcal{S}_r^n$ converges to $\mathcal{S}_d$ as $n \to \infty$.

S3 Root-locus Analysis

To carry out a standard root-locus analysis, the closed-loop transfer function should be rewritten in the following form

$$H(s) = \frac{T(s)}{1 + KG(s)}, \tag{S23}$$

where K is the constant gain of interest (e.g. K_I or K_P), such that $KG(s) \triangleq K\frac{N(s)}{D(s)}$ represents the loop gain, and $T(s) \triangleq \frac{M(s)}{D(s)}$ is a rational function of s which does not play a role in the closed-loop root-locus. For the rAIF topology in Fig. 3(a) which realizes a filtered (I + FF) controller, Equation (9) can be rewritten in the form of Equation (S23) as

$$K = K_I, \quad G(s) = \frac{K_S\omega_0}{s(s + \omega_0)(s + \gamma_1)}. \tag{S24}$$

The root-locus starts (at $K_I = 0$) from the poles $(0, -\omega_0, -\gamma_1)$ of $G(s)$ and ends (at $K_I \to \infty$) at its zeros ($s \to \infty$ because $N(s) = K_S\omega_0$ is a constant). As K_I is increased from zero, the first root-locus branch starting from the most negative open-loop pole, $-\max(\gamma_1, \omega_0)$, moves on the real axis toward $-\infty$. The other two branches move toward each other and break away from the real axis and approach two asymptotes intersecting with the real axis at $-(\gamma_1 + \omega_0)/3$ with angles $\pi/3$ and $-\pi/3$. The break-away point of the root-locus branch starting from $s = -\min(\gamma_1, \omega_0)$ and $s = 0$ is at

$$s_b = \frac{\sqrt{\omega_0^2 + \gamma_1^2 - \omega_0\gamma_1} - (\omega_0 + \gamma_1)}{3}, \tag{S25}$$

and so it is easy to show that $-\frac{\gamma_1}{2} < s_b \leq 0$. In fact, the fastest response which can be achieved by an infinite cutoff frequency ω_0 is limited by a threshold dictated by $\frac{\gamma_1}{2}$. These results are summarized in Fig. 4 (a) of the main text. More details are also reported in SI Fig. S3(a).

S4 Pole Placement

In this section, we derive the bounds on the achievable poles for the two negative actuation scenarios of sAIF: repression and degradation. Placing the three poles at a single location $s = -a$, allows us to express (K_P, K_I, ω_0) in terms of the birth-death parameter γ_1, the sensing gain K_S, and the placed pole $-a$ as shown in Equation (11). Note that the supporting input $\bar{u}$ is calculated using the equation $\bar{u} - \gamma_1 r = 0$, where $r \triangleq \mu/\theta$ represents the setpoint.

S4.1 Repression

Plugging (K_P, K_I, ω_0) in the coverage condition in Equation (S18) yields

$$\begin{cases} 0 < \dfrac{3a^2 - \gamma_1(3a - \gamma_1)}{K_S(3a - \gamma_1)} < \dfrac{n\gamma_1}{K_S} \\ \dfrac{a^3 n\gamma_1}{(n+1)\gamma_1(3a - \gamma_1) - 3a^2} < 3a^2 - \gamma_1(3a - \gamma_1). \end{cases} \tag{S26}$$

From the first inequality, we get

$$\frac{n + 1 - \sqrt{(n+1)(n - \frac{1}{3})}}{2} < a < \frac{n + 1 + \sqrt{(n+1)(n - \frac{1}{3})}}{2}, \tag{S27}$$

and from the second, we get $\zeta_1 < a < \zeta_2$ where ζ_1, ζ_2 are the two positive roots of the following fourth-order polynomial equation given by

$$9\zeta^4 - (8n + 18)\zeta^3 + (12n + 15)\zeta^2 - (6n + 61)\zeta + (n + 1) = 0. \tag{S28}$$

Calculating the intersection of the two inequalities yields the bounds for the achievable poles $s_l(n)\gamma_1 < a < s_u(n)\gamma_1$ where

$$\begin{cases} s_l(n) = \max\left(\dfrac{n + 1 - \sqrt{(n+1)(n - \frac{1}{3})}}{2}, \zeta_1\right) \\ s_u(n) = \min\left(\dfrac{n + 1 + \sqrt{(n+1)(n - \frac{1}{3})}}{2}, \zeta_2\right). \end{cases} \tag{S29}$$

In the case of repression without cooperativity, it is not possible to place the three poles at a single location. However, we can still study the dynamics by placing the poles at two different locations instead of one. To this end, assume two poles are placed at $s = -a_1$ and one pole at $s = -a_2$. Equating the closed-loop characteristic polynomial in this case $(s + a_1)^2(s + a_2)$ to the denominator of $H_{\text{sAIF}}(s)$ gives the expression of the PI gains (K_P, K_I) and the cutoff frequency ω_0 in terms of the birth-death parameter γ_1, the sensing gain K_S and the placed pole locations $-a_1, -a_2$ as

$$\begin{cases} K_P = \dfrac{a_1^2 + 2a_1a_2}{K_S(2a_1 + a_2 - \gamma_1)} - \dfrac{\gamma_1}{K_S}, \\ K_I = \dfrac{a_1^2 a_2}{K_S(2a_1 + a_2 - \gamma_1)}, \ \omega_0 = 2a_1 + a_2 - \gamma_1. \end{cases} \tag{S30}$$

Plugging (K_P, K_I, ω_0) in the coverage condition in Equation (S18) yields

$$\begin{cases} 0 < \dfrac{B_2}{B_1} < (n+1)\gamma_1 \\ \dfrac{n\gamma_1 a_1^2 a_2}{(n+1)\gamma_1 B_1 - B_2} < B_2 - B_1 \end{cases} \tag{S31}$$

where $B_1 = 2a_1 + a_2 - \gamma_1$, $B_2 = a_1^2 + 2a_1a_2$. Rewriting $a_1 = b_1\gamma_1$ and $a_2 = b_2\gamma_2$, the inequalities in Equation (S31) simplify to

$$\begin{cases} (n+1)c_1 - C_2 > 0 \\ (C_2 - C_1)\left[(n+1)C_1 - C_2\right] - nb_1^2 b_2 > 0 \end{cases} \tag{S32}$$

where $C_1 = 2b_1 + b_2 - 1$, $C_2 = b_1^2 + 2b_1b_2$. One can rely on graphical tools to calculate the intersection of the two inequalities as demonstrated in SI Fig. S3(d).

S4.2 Degradation

Plugging (K_P, K_I, ω_0) in the coverage condition in Equation (S22) yields

$$\frac{a^3}{K_S(3a-\gamma_1)} < (3a-\gamma_1)\frac{3a^2-\gamma_1(3a-\gamma_1)}{K_S(3a-\gamma_1)}, \tag{S33}$$

which simplifies to $a > \frac{\gamma_1}{2}$.

S5 Connections between the Deterministic & Stochastic Settings

This section delves into the connections that tie the sAIF controller to the pure integral controller on one hand, and the filtered proportional controller on the other. Specifically, we connect their performance with respect to the gains in the deterministic setting, and noise behavior in the stochastic setting. As a result of this analysis, we draw a connection between deterministic gains and stochastic noise characteristics.

S5.1 Deterministic Setting

We begin by examining how the gains of the sAIF controller change while tuning the sequestration rate η. As calculated in Equation (S7) and Equation (S16), the transfer function of the sAIF controller is given by

$$\mathcal{C}: \quad \hat{u}(s) = \left[\frac{K_I}{s}\hat{e}(s) - K_P\hat{x}_L(s)\right]\frac{\omega_0}{s+\omega_0}, \tag{S34}$$

where

$$K_I \triangleq \frac{\sigma_2\bar{z}_2}{\bar{z}_1+\bar{z}_2}, \quad K_P \triangleq \frac{\sigma_2\theta}{\eta(\bar{z}_1+\bar{z}_2)}, \quad \omega_0 \triangleq \eta(\bar{z}_1+\bar{z}_2). \tag{S35}$$

Note the slight change of notation in the controller transfer function: the proportional gain K_P here is equal to K_PK_S in Equation (S7). This change of notation is necessary to perform a fair comparison with the filtered proportional controller. Recall that the supporting input $\bar{u} = h(\bar{z}_2)$ that steers the output to the robust setpoint at steady state depends solely on the setpoint r and the process (see Assumption 1 and the remarks thereafter). Therefore, as long as closed-loop stability is maintained, RPA is achieved with $\bar{x}_L = \mu/\theta$, and the steady state value $\bar{z}_2$ is independent of η. However, $\bar{z}_1$ changes in accordance with η to guarantee RPA. From Equation (S5), at steady state we have $\mu = \eta\bar{z}_1\bar{z}_2$, and thus we can express $\bar{z}_1 = \frac{\mu}{\eta\bar{z}_2}$. To this end, getting rid of $\bar{z}_1$ in the gains of sAIF controller yields

$$K_I = \frac{\sigma_2\bar{z}_2}{\frac{\mu}{\eta\bar{z}_2}+\bar{z}_2}, \qquad K_P = \frac{\sigma_2\theta}{\frac{\mu}{\bar{z}_2}+\eta\bar{z}_2}, \qquad \omega_0 = \frac{\mu}{\bar{z}_2}+\eta\bar{z}_2. \tag{S36}$$

Observe that K_I and ω_0 are monotonically increasing in η, while K_P is monotonically decreasing in η. Hence, varying the sequestration rate η tunes the integral and proportional gains in opposite directions. Next, let us examine the two extreme values of η: 0 and ∞. Observe that as $\eta \to \infty$, we have

$$\lim_{\eta\to\infty} K_I = \sigma_2, \qquad \lim_{\eta\to\infty} K_P = 0, \qquad \lim_{\eta\to\infty} \omega_0 = \infty. \tag{S37}$$

Therefore, increasing η towards infinity yields a pure integral controller (with no low-pass filter). In contrast, for small values of η, we have

$$K_I \approx 0, \qquad K_P \approx \frac{\sigma_2\theta}{\mu/\bar{z}_2}, \qquad \omega_0 \approx \mu/\bar{z}_2. \tag{S38}$$

Observe that Equation (S38) becomes identical to Equation (S4) (with $K_F = K_P' = 0$) by equating the degradation rate δ of $\mathbf{Z_2}$ in the filtered proportional controller to the cutoff frequency of the sAIF controller, i.e. $\delta \triangleq \omega_0 = \mu/\bar{z}_2$. This implies that for small η, the sAIF controller behaves like the filtered proportional controller. In fact, as far as the sequestration reaction is concerned, the highest proportional gain that can be achieved by the sAIF controller corresponds to the gain of the filtered proportional controller with $\delta \triangleq \mu/\bar{z}_2$. This indicates that the proportional gain of the sAIF controller is limited by the filtered proportional component used to assemble the sAIF controller. This analysis reveals how the sAIF controller connects a pure integral controller with a filtered proportional controller, where the sequestration rate η dictates the relative contribution of the two components since

$$\frac{K_P}{K_I} = \frac{\theta}{\eta\bar{z}_2}, \tag{S39}$$

where $\bar{z}_2$ is independent of η.

S5.2 Stochastic Setting

How does this connection established in the deterministic setting translate into the stochastic setting? We explore this question by analyzing the coefficient of variation (CV) across different controllers for a simple birth-death process. The CV, defined as the ratio between the standard deviation and the mean, gives us a dimensionless measure of variability. Given the intractability of the chemical master equation (CME) and the challenges posed by the moment closure problem, we estimate the CV of the output using the linear noise approximation (LNA).

S5.2.1 Filtered Proportional Controller

In the stochastic setting, a simple birth-death process controlled by the filtered proportional controller of Fig. 2(c) can be modeled by a stochastic chemical reaction network (SCRN) represented by the following stoichiometry matrix and propensity function

$$S = \begin{bmatrix} 1 & -1 & 0 & 0 \\ 0 & 0 & 1 & -1 \end{bmatrix}, \qquad \lambda(x, z_2) = \begin{bmatrix} h(z_2) & \gamma x & \theta x & \delta z_2 \end{bmatrix}^T. \tag{S40}$$

LNA provides algebraic equations that approximate the stationary mean $\left(\mathbb{E}\left[\bar{X}\right], \mathbb{E}\left[\bar{Z}_2\right]\right)$ and covariance $\bar{\Sigma}$ of the closed-loop state vector $\begin{bmatrix} X & Z_2 \end{bmatrix}^T$ given by

$$\begin{cases} h\left(\mathbb{E}\left[\bar{Z}_2\right]\right) - \gamma \mathbb{E}\left[\bar{X}\right] \approx 0 \\ \theta \mathbb{E}\left[\bar{X}\right] - \delta \mathbb{E}\left[\bar{Z}_2\right] \approx 0 \\ A\bar{\Sigma} + \bar{\Sigma} A^T + W \approx 0, \end{cases} \tag{S41}$$

where $A \triangleq \begin{bmatrix} -\gamma & -\sigma_2 \\ \theta & -\delta \end{bmatrix}, W \triangleq \begin{bmatrix} h\left(\mathbb{E}\left[\bar{Z}_2\right]\right) + \gamma \mathbb{E}\left[\bar{X}\right] & 0 \\ 0 & \theta \mathbb{E}\left[\bar{X}\right] + \delta \mathbb{E}\left[\bar{Z}_2\right] \end{bmatrix}$ and $\sigma_2 \triangleq -h'\left(\mathbb{E}\left[\bar{Z}_2\right]\right)$. Using the first two equations in Equation (S41), we get rid of the terms $h\left(\mathbb{E}\left[\bar{Z}_2\right]\right)$ and $\mathbb{E}\left[\bar{Z}_2\right]$ in W to express it in terms of $\mathbb{E}\left[\bar{X}\right]$ as $W = \begin{bmatrix} 2\gamma & 0 \\ 0 & 2\theta \end{bmatrix} \mathbb{E}\left[\bar{X}\right]$. Thus solving the Lyapunov equation in Equation (S41), we obtain $\mathrm{Var}\left[\bar{X}\right]$ from $\bar{\Sigma}_{11}$. This allows us to express the CV in terms of the expectation as

$$\mathrm{CV}\left[\bar{X}\right]^2 \approx \frac{1}{\mathbb{E}\left[\bar{X}\right]} \left[1 + \frac{\sigma_2 \theta (\sigma_2 - \delta)}{(\gamma + \delta)(\gamma\delta + \sigma_2 \theta)}\right]. \tag{S42}$$

To connect the CV with the deterministic proportional gain, we recall that $K_P \triangleq \frac{\sigma_2 \theta}{\omega_0}$ and $\omega_0 \triangleq \delta$, and thus we have

$$\mathrm{CV}\left[\bar{X}\right]^2 \approx \frac{1}{\mathbb{E}\left[\bar{X}\right]} \left[1 + \frac{K_P \omega_0 \left(\frac{K_P}{\theta} - 1\right)}{(\gamma + \omega_0)(\gamma + K_P)}\right]. \tag{S43}$$

Compared to the CV in the open-loop in Equation (13), the filtered proportional controller attenuates noise if

$$K_P < \theta \text{ or equivalently } \sigma_2 < \omega_0. \tag{S44}$$

It is important to mention that this result should not be interpreted as "lower proportional gain reduces noise". Instead, it shows that the noise reduction is constrained by the low-pass filter (ω_0 and θ). In fact, if we increase ω_0 and θ towards ∞, the filtered proportional controller approaches the unfiltered proportional controller which unconditionally reduces noise.

S5.2.2 sAIF Controller

Next, we consider the simple birth-death process controlled by the sAIF controller depicted in Fig. 3(a). The closed-loop can now be modeled as a SCRN represented by the following stoichiometry matrix and propensity function

$$S = \begin{bmatrix} 1 & -1 & 0 & 0 & 0 \\ 0 & 0 & 1 & 0 & -1 \\ 0 & 0 & 0 & 1 & -1 \end{bmatrix}, \qquad \lambda(x, z_1, z_2) = \begin{bmatrix} h(z_2) & \gamma x & \mu & \theta x & \eta z_1 z_2 \end{bmatrix}^T. \tag{S45}$$

Once again, LNA provides algebraic equations that approximate the stationary mean $\left(\mathbb{E}[\bar{X}], \mathbb{E}[\bar{Z}_1], \mathbb{E}[\bar{Z}_2]\right)$ and covariance $\bar{\Sigma}$ of the closed-loop state vector $\begin{bmatrix} X & Z_1 & Z_2 \end{bmatrix}^T$ given by

$$\begin{cases} h\left(\mathbb{E}[\bar{Z}_2]\right) - \gamma\mathbb{E}[\bar{X}] \approx 0 \\ \mu - \eta\mathbb{E}[\bar{Z}_1]\,\mathbb{E}[\bar{Z}_2] \approx 0 \\ \theta\mathbb{E}[\bar{X}] - \eta\mathbb{E}[\bar{Z}_1]\,\mathbb{E}[\bar{Z}_2] \approx 0 \\ A\bar{\Sigma} + \bar{\Sigma}A^T + W \approx 0, \end{cases} \tag{S46}$$

where $A \triangleq \begin{bmatrix} -\gamma & 0 & -\sigma_2 \\ 0 & -\eta\mathbb{E}[\bar{Z}_2] & -\eta\mathbb{E}[\bar{Z}_1] \\ \theta & -\eta\mathbb{E}[\bar{Z}_2] & -\eta\mathbb{E}[\bar{Z}_1] \end{bmatrix}$, $W = \begin{bmatrix} h\left(\mathbb{E}[\bar{Z}_2]\right) + \gamma\mathbb{E}[\bar{X}] & 0 & 0 \\ 0 & \mu + \eta\mathbb{E}[\bar{Z}_1]\,\mathbb{E}[\bar{Z}_2] & \eta\mathbb{E}[\bar{Z}_1]\,\mathbb{E}[\bar{Z}_2] \\ 0 & \eta\mathbb{E}[\bar{Z}_1]\,\mathbb{E}[\bar{Z}_2] & \theta\mathbb{E}[\bar{X}] + \eta\mathbb{E}[\bar{Z}_1]\,\mathbb{E}[\bar{Z}_2] \end{bmatrix}$ and $\sigma_2 \triangleq -h'\left(\mathbb{E}[\bar{Z}_2]\right)$. Using the first three equations in Equation (S46), we get rid of the terms $h\left(\mathbb{E}[\bar{Z}_2]\right), \mu$, and $\mathbb{E}[\bar{Z}_1]\,\mathbb{E}[\bar{Z}_2]$ in W to express it in terms of $\mathbb{E}[\bar{X}]$ as $W = \begin{bmatrix} 2\gamma & 0 & 0 \\ 0 & 2\theta & \theta \\ 0 & \theta & 2\theta \end{bmatrix}\mathbb{E}[\bar{X}]$. Similarly, we substitute $\mathbb{E}[\bar{Z}_1] \approx \mu/\eta\mathbb{E}[\bar{Z}_2]$ and $\mathbb{E}[\bar{Z}_2] \approx h^{-1}\left(\gamma\mathbb{E}[\bar{X}]\right)$ in A. Hence, solving the Lyapunov equation in Equation (S46), we obtain $\mathrm{Var}[\bar{X}]$ from $\bar{\Sigma}_{11}$. This allows us to express the CV in terms of the expectation as

$$\mathrm{CV}[\bar{X}]^2 \approx \frac{1}{\mathbb{E}[\bar{X}]}\left[1 + \frac{\sigma_2\theta\left(\sigma_2 - \omega_0\right) + \eta\mathbb{E}[\bar{Z}_2]\,\sigma_2\left(\omega_0 + \gamma + \theta\right)}{\left(\gamma + \omega_0\right)\left(\gamma\omega_0 + \sigma_2\theta\right) - \eta\mathbb{E}[\bar{Z}_2]\,\sigma_2\theta}\right], \tag{S47}$$

where

$$\omega_0 \triangleq \eta\left(\mathbb{E}[\bar{Z}_1] + \mathbb{E}[\bar{Z}_2]\right) = \frac{\mu}{\mathbb{E}[\bar{Z}_2]} + \eta\mathbb{E}[\bar{Z}_2] \qquad \text{and} \qquad \mathbb{E}[\bar{Z}_2] \approx h^{-1}\left(\gamma\mathbb{E}[\bar{X}]\right). \tag{S48}$$

Two observations can now be made regarding Equation (S47) for a given setpoint $\mathbb{E}[\bar{X}] = \mu/\theta$. First, computing the derivative of $\mathrm{CV}[\bar{X}]^2$ with respect to η yields

$$\frac{d}{d\eta}\mathrm{CV}[\bar{X}]^2 \approx \frac{\mu\sigma_2\mathbb{E}[\bar{Z}_2]^2}{\mathbb{E}[\bar{X}]}\frac{\eta^2\gamma\mathbb{E}[\bar{Z}_2]^4 + 2\eta(\gamma^2 + \theta\gamma + \sigma_2\theta)\mathbb{E}[\bar{Z}_2]^3 + \gamma(\gamma^2 + \theta\gamma + 2\eta\mu)\mathbb{E}[\bar{Z}_2]^2 + \mu(2\gamma^2 + 2\theta\gamma + \sigma_2\theta)\mathbb{E}[\bar{Z}_2] + \gamma\mu^2}{\left[\left(\gamma + \omega_0\right)\left(\gamma\omega_0 + \sigma_2\theta\right) - \eta\mathbb{E}[\bar{Z}_2]\,\sigma_2\theta\right]^2}. \tag{S49}$$

Given that $\frac{d}{d\eta}\mathrm{CV}[\bar{X}]^2 \geq 0$, it follows that the coefficient of variation for a specified expected value is a monotonically increasing function of the sequestration rate η. Consequently, the LNA reflects the trend observed in the simulations depicted in Fig. 5, showing that increasing η leads to a higher noise level in the output.

The second observation pertains to the connection of the sAIF controller with the filtered proportional controller. Indeed, observe that for small η, from Equation (S47), we have

$$\mathrm{CV}[\bar{X}]^2 \approx \frac{1}{\mathbb{E}[\bar{X}]}\left[1 + \frac{\sigma_2\theta\left(\sigma_2 - \omega_0\right)}{\left(\gamma + \omega_0\right)\left(\gamma\omega_0 + \sigma_2\theta\right)}\right] \qquad \text{with} \quad \omega_0 = \frac{\mu}{h^{-1}\left(\gamma\mathbb{E}[\bar{X}]\right)}. \tag{S50}$$

When the degradation rate δ of $\mathbf{Z_2}$ in the filtered proportional controller is set equal to the cutoff frequency of the sAIF controller with small η, namely $\delta \triangleq \omega_0 = \mu/h^{-1}\left(\gamma\mathbb{E}[\bar{X}]\right)$, Equation (S50) becomes identical to Equation (S42). This alignment underscores that in scenarios where η is very small, the sAIF controller mimics the behavior of the filtered proportional controller with respect to CV, similar to observations in the deterministic framework. Consequently, the minimum CV achievable by the sAIF controller is constrained by its hidden proportional component - an observation that is seen in the simulations of Fig. 5.

To explicitly connect the CV with the deterministic framework, we recall from Equation (S36) that

$$\begin{cases} K_P = \dfrac{\sigma_2\theta}{\omega_0} \implies \sigma_2 = \dfrac{K_P\omega_0}{\theta} \\ K_I = \dfrac{\eta\mathbb{E}[\bar{Z}_2]\,\sigma_2}{\omega_0} \implies \eta\mathbb{E}[\bar{Z}_2] = \dfrac{\theta K_I}{K_P}. \end{cases} \tag{S51}$$

Substituting for σ_2 and $\eta\mathbb{E}[\bar{Z}_2]$ in Equation (S47) yields

$$\mathrm{CV}[\bar{X}]^2 \approx \frac{1}{\mathbb{E}[\bar{X}]}\left[1 + \frac{K_P\omega_0\left(\frac{K_P}{\theta} - 1\right) + K_I\left(\omega_0 + \gamma + \theta\right)}{\left(\gamma + \omega_0\right)\left(\gamma + K_P\right) - \theta K_I}\right] \geq \frac{1}{\mathbb{E}[\bar{X}]}\left[1 + \frac{K_P\omega_0\left(\frac{K_P}{\theta} - 1\right)}{\left(\gamma + \omega_0\right)\left(\gamma + K_P\right)}\right], \tag{S52}$$

where the lower bound is exactly the CV corresponding to the proportional component given in Equation (S43) which is achieved by setting the integral gain K_I to zero.

S6 Non-Ideal Conditions: Dilution Effects

In this section, we examine the properties of the various controllers while considering the effects of dilution on the controller species.

S6.1 Steady-State Sensitivities in the Deterministic Setting

Consider the closed-loop configuration shown in Fig. 2(a), which consists of an arbitrary regulated network—referred to as the process $\mathcal{P}_\Delta$—subject to a constant disturbance Δ. The system's input and output are denoted by u and y, respectively, with y potentially representing a species concentration, such as x_L, as an example. The feedback controller, denoted by $\mathcal{C}$, takes the output y as its input and generates the control signal u, which is fed back to the process. Let x and z be two nonnegative vectors representing the internal states of the regulated network and the controller, respectively. The deterministic dynamics of the closed-loop system are described by the following set of nonlinear differential-algebraic equations

$$\begin{aligned} &\textbf{Process:} \quad y = \mathcal{P}_\Delta(u) \quad \Longleftrightarrow \quad \begin{cases} \dot{x} = f_\Delta(x,u), \\ y = g_\Delta(x,u), \end{cases} \\ &\textbf{Controller:} \quad u = \mathcal{C}(y) \quad \Longleftrightarrow \quad \begin{cases} \dot{z} = \psi(z,y), \\ u = h(z), \end{cases} \end{aligned} \tag{S53}$$

where f_Δ, g_Δ, ψ, and h are continuously differentiable functions defined on the positive orthant. Observe that here u is a function of z only.

Definitions. The set of feasible inputs $\mathbb{U}$ is defined as the range of h over the positive orthant, i.e.,

$$\mathbb{U} \triangleq \{\bar{u} \geq 0 : \exists \bar{z} \geq 0 \text{ with } \bar{u} = h(\bar{z})\}. \tag{S54}$$

The set of admissible setpoints of the process $\mathcal{P}_\Delta$ with disturbance Δ over the set of feasible inputs $\mathbb{U}$ is denoted by $\mathcal{R}(\mathcal{P}_\Delta, \mathbb{U})$ with

$$\mathcal{R}(\mathcal{P}_\Delta, \mathbb{U}) \triangleq \{\bar{y} \geq 0 : \exists \bar{u} \in \mathbb{U}, \bar{x} \geq 0 \text{ with } f_\Delta(\bar{x},\bar{u}) = 0 \text{ and } \bar{y} = g_\Delta(\bar{x},\bar{u})\}. \tag{S55}$$

The steady-state input/output maps of the process and the controller are expressed as

$$\begin{aligned} &\textbf{Process:} \quad \bar{y} = \bar{\mathcal{P}}_\Delta(\bar{u}) \quad \Longleftrightarrow \quad \begin{cases} 0 = f_\Delta(\bar{x},\bar{u}), \\ \bar{y} = g_\Delta(\bar{x},\bar{u}), \end{cases} \\ &\textbf{Controller:} \quad \bar{u} = \bar{\mathcal{C}}(\bar{y}) \quad \Longleftrightarrow \quad \begin{cases} 0 = \psi(\bar{z},\bar{y}), \\ \bar{u} = h(\bar{z}), \end{cases} \end{aligned} \tag{S56}$$

where we assume for simplicity that the algebraic equations $f_\Delta(\bar{x},\bar{u}) = 0$ and $\psi_\Delta(\bar{z},\bar{y}) = 0$ have unique non-negative solutions $\bar{x}$ and $\bar{z}$ for a given $\bar{u}$ and $\bar{y}$, respectively. Finally, the network $\mathcal{P}_\Delta$ is strictly monotonic if $\bar{\mathcal{P}}'_\Delta(\bar{u})$ does not change sign for all $\bar{u} \geq 0$, and the closed loop is said to operate in a negative feedback configuration if $\mathcal{P}_\Delta$ and $\mathcal{C}$ have opposite monotonicity or $\bar{\mathcal{P}}'_\Delta(\bar{u})\bar{\mathcal{C}}'(\bar{y}) \leq 0$.

S6.1.1 Comparison Between Non-Ideal sAIF and Filtered Proportional Controllers

We are now ready to prove Theorem 1 which is repeated here for convenience.

Theorem 1. *For any strictly monotonic regulated network under a constant disturbance Δ, operating in negative feedback with either a non-ideal sAIF or filtered proportional (fP) controller, assume identical dilution rate δ and strictly monotonic actuation mechanisms h_s for both controllers (see Fig. 6(a)). At any desired steady-state output $\bar{x}_L = r$, the steady-state sensitivity to the disturbance satisfies*

$$\left|\frac{\partial \bar{x}_L}{\partial \Delta}\right|^{sAIF} < \left|\frac{\partial \bar{x}_L}{\partial \Delta}\right|^{fP}.$$

Moreover, if either μ or θ is fixed and the other tuned to maintain $\bar{x}_L = r$, the sensitivity strictly decreases as the sequestration rate η increases.

Proof. Consider an arbitrary process $\mathcal{P}_\Delta$ infiltrated by a constant disturbance Δ, and whose input and output are denoted by u and y, respectively. The dynamics of the closed-loop systems with either the non-ideal sAIF controller $\mathcal{C}_s$ or the filtered proportional controller $\mathcal{C}_p$ are given by the following equations:

$$\begin{aligned}
&\textbf{Process:} && y = \mathcal{P}_\Delta(u) && \iff && \begin{cases} \dot{x} = f_\Delta(x,u) \\ y = g_\Delta(x,u) \end{cases} \\
&\textbf{Non-Ideal sAIF Controller:} && u = \mathcal{C}_s(y) && \iff && \begin{cases} \dot{z}_1 = \mu - \eta z_1 z_2 - \delta z_1 \\ \dot{z}_2 = \theta_s y - \eta z_1 z_2 - \delta z_2 \\ u = h_s(z_2) \end{cases} \\
&\textbf{fP Controller:} && u = \mathcal{C}_p(y) && \iff && \begin{cases} \dot{z}_2 = \theta_p y - \delta z_2 \\ u = h_s(z_2). \end{cases}
\end{aligned} \tag{S57}$$

Here, f_Δ, g_Δ, and h_s are continuously differentiable functions, with h_s being strictly monotonic. Observe that the dilution rate δ and the actuation mechanism h_s are the same for both controllers.

For a given disturbance Δ and desired admissible steady-state output $\bar{y} \in \mathcal{R}(\mathcal{P}_\Delta, \mathbb{U})$, there exists a $\bar{u} \in \mathbb{U}$ such that $\bar{y} = \bar{\mathcal{P}}_\Delta(\bar{u})$. Furthermore, since $\bar{u} \in \mathbb{U}$, there exists a $\bar{z}_2 \geq 0$ such that $h_s(\bar{z}_2) = \bar{u}$. Therefore, we have

$$\bar{y} = \bar{\mathcal{P}}_\Delta \circ h_s(\bar{z}_2) \implies \bar{z}_2 = h_s^{-1} \circ \bar{\mathcal{P}}_\Delta^{-1}(\bar{y}) \triangleq F(\bar{y}, \Delta), \tag{S58}$$

where the inverses exist due to the strict monotonicity assumptions. These expressions are valid for both controllers. Next, we write a single nonlinear algebraic equation for $\bar{y}$ for both controllers. The following calculations encapsulate both cases with $(\theta, \eta) = (\theta_s, \text{positive})$ for the sAIF controller, while $(\theta, \eta) = (\theta_p, 0)$ for the fP controller. Dropping the bar for convenience, we have

$$\begin{cases} \mu - \eta z_1 z_2 - \delta z_1 = 0 \\ \theta y - \eta z_1 z_2 - \delta z_2 = 0 \end{cases} \implies \eta\delta z_2^2 + \left[\eta(\mu - \theta y) + \delta^2\right] z_2 - \delta\theta y = 0 \qquad \text{with} \qquad z_2 = F(y, \Delta). \tag{S59}$$

The sensitivity of the steady-state output with respect to disturbances can be implicitly calculated as follows

$$2\eta\delta z_2 \frac{\partial z_2}{\partial \Delta} - \eta\theta \frac{\partial y}{\partial \Delta} z_2 + \left[\eta(\mu - \theta y) + \delta^2\right] \frac{\partial z_2}{\partial \Delta} - \delta\theta \frac{\partial y}{\partial \Delta} = 0 \quad \text{with} \quad \begin{cases} z_2 = F(y, \Delta) \\ \dfrac{\partial z_2}{\partial \Delta} = \dfrac{\partial F(y,\Delta)}{\partial y} \dfrac{\partial y}{\partial \Delta} + \dfrac{\partial F(y,\Delta)}{\partial \Delta}. \end{cases} \tag{S60}$$

We proceed with some algebraic manipulations to obtain an expression for $\frac{\partial y}{\partial \Delta}$

$$\begin{aligned}
\left[2\eta\delta z_2 + \delta^2 + \eta(\mu - \theta y)\right] \frac{\partial z_2}{\partial \Delta} - \theta\left(\eta z_2 + \delta\right) \frac{\partial y}{\partial \Delta} &= 0 \\
\left[\delta(\eta z_2 + \delta) + \eta(\mu - \theta y + \delta z_2)\right] \frac{\partial z_2}{\partial \Delta} - \theta\left(\eta z_2 + \delta\right) \frac{\partial y}{\partial \Delta} &= 0 \\
\left[\delta(\eta z_2 + \delta) + \eta\delta z_1\right] \frac{\partial z_2}{\partial \Delta} - \theta\left(\eta z_2 + \delta\right) \frac{\partial y}{\partial \Delta} &= 0 \\
\left[\delta(\eta z_2 + \delta) + \eta \frac{\mu\delta}{\eta z_2 + \delta}\right] \frac{\partial z_2}{\partial \Delta} - \theta\left(\eta z_2 + \delta\right) \frac{\partial y}{\partial \Delta} &= 0 \\
\delta\left[1 + \frac{\eta\mu}{(\eta z_2 + \delta)^2}\right] \frac{\partial z_2}{\partial \Delta} - \theta \frac{\partial y}{\partial \Delta} &= 0 \\
\delta\left[1 + \frac{\eta\mu}{(\eta z_2 + \delta)^2}\right] \left[\frac{\partial F(y,\Delta)}{\partial y} \frac{\partial y}{\partial \Delta} + \frac{\partial F(y,\Delta)}{\partial \Delta}\right] - \theta \frac{\partial y}{\partial \Delta} &= 0 \\
\left[\delta\left(1 + \frac{\eta\mu}{(\eta z_2 + \delta)^2}\right) \frac{\partial F(y,\Delta)}{\partial y} - \theta\right] \frac{\partial y}{\partial \Delta} &= -\delta\left(1 + \frac{\eta\mu}{(\eta z_2 + \delta)^2}\right) \frac{\partial F(y,\Delta)}{\partial \Delta} \\
\implies \frac{\partial y}{\partial \Delta} &= -\frac{\frac{\partial F(y,\Delta)}{\partial \Delta}}{\frac{\partial F(y,\Delta)}{\partial y} - \frac{\theta}{\delta} \frac{1}{1 + \frac{\eta\mu}{(\eta z_2 + \delta)^2}}}.
\end{aligned} \tag{S61}$$

Note that

$$\frac{\partial F(y,\Delta)}{\partial y} = \frac{1}{h_s' \left(h_s^{-1} \circ \bar{\mathcal{P}}_\Delta^{-1}(y)\right) \bar{\mathcal{P}}_\Delta' \left(\bar{\mathcal{P}}_\Delta^{-1}(y)\right)} < 0, \tag{S62}$$

since we have a negative feedback configuration. Therefore, we have

$$\left|\frac{\partial \bar{y}}{\partial \Delta}\right| = \frac{\left|\frac{\partial F(\bar{y},\Delta)}{\partial \Delta}\right|}{\left|\frac{\partial F(\bar{y},\Delta)}{\partial \bar{y}}\right| + \frac{\theta}{\delta}\frac{1}{1+\frac{\eta\mu}{(\eta F(\bar{y},\Delta)+\delta)^2}}}. \tag{S63}$$

To fix the setpoint $\bar{y} = r$ at some disturbance Δ_0, the parameters μ, θ and η should satisfy

$$\eta\delta\bar{z}_2^2 + \left[\eta(\mu - \theta\bar{y}) + \delta^2\right]\bar{z}_2 - \delta\theta\bar{y} = 0 \quad \Longrightarrow \quad \theta = \frac{F(r,\Delta_0)}{r}\left[\delta + \frac{\eta\mu}{\eta F(r,\Delta_0)+\delta}\right]. \tag{S64}$$

Therefore the sensitivity becomes

$$\left|\frac{\partial \bar{y}}{\partial \Delta}\right|_{(\bar{y},\Delta)=(r,\Delta_0)} = \frac{\left|\frac{\partial F(r,\Delta_0)}{\partial \Delta}\right|}{\left|\frac{\partial F(r,\Delta_0)}{\partial \bar{y}}\right| + \frac{F(r,\Delta_0)}{r}\frac{1+\frac{1}{\delta}\frac{\eta\mu}{\eta F(r,\Delta_0)+\delta}}{1+\frac{\eta\mu}{(\eta F(r,\Delta_0)+\delta)^2}}}. \tag{S65}$$

As such, for the cases of the non-ideal sAIF and filtered proportional controllers, we obtain:

$$\begin{aligned}
&\textbf{non-ideal sAIF:} \quad \left|\frac{\partial \bar{y}}{\partial \Delta}\right|_{(\bar{y},\Delta)=(r,\Delta_0)} = \frac{\left|\frac{\partial F(r,\Delta_0)}{\partial \Delta}\right|}{\left|\frac{\partial F(r,\Delta_0)}{\partial \bar{y}}\right| + \phi_s} \quad \text{with} \quad \phi_s \triangleq \frac{F(r,\Delta_0)}{r}\frac{1+\frac{1}{\delta}\frac{\eta\mu}{\eta F(r,\Delta_0)+\delta}}{1+\frac{\eta\mu}{(\eta F(r,\Delta_0)+\delta)^2}} \\
&\textbf{fP:} \quad \left|\frac{\partial \bar{y}}{\partial \Delta}\right|_{(\bar{y},\Delta)=(r,\Delta_0)} = \frac{\left|\frac{\partial F(r,\Delta_0)}{\partial \Delta}\right|}{\left|\frac{\partial F(r,\Delta_0)}{\partial \bar{y}}\right| + \phi_p} \quad \text{with} \quad \phi_p \triangleq \frac{F(r,\Delta_0)}{r}.
\end{aligned} \tag{S66}$$

Observe that

$$\phi_s - \phi_p = \frac{F(r,\Delta_0)}{r}\left[\frac{1+\frac{1}{\delta}\frac{\eta\mu}{\eta F(r,\Delta_0)+\delta}}{1+\frac{\eta\mu}{(\eta F(r,\Delta_0)+\delta)^2}} - 1\right] = \frac{\eta F^2(r,\Delta_0)}{r\delta}\frac{\frac{\eta\mu}{(\eta F(r,\Delta_0)+\delta)^2}}{1+\frac{\eta\mu}{(\eta F(r,\Delta_0)+\delta)^2}} > 0, \tag{S67}$$

and therefore the sensitivity in the case of the non-ideal sAIF controller is lower than that in the case of the filtered proportional controller.

Next, we analyze the monotonicity of $\left|\frac{\partial \bar{y}}{\partial \Delta}\right|$ with respect to η. We consider two scenarios.

Scenario 1. Fix θ, δ, the steady-state output level $\bar{y} = r$ and the disturbance level $\Delta = \Delta_0$. Then as η is adjusted, μ should be tuned to maintain the steady-state output level at $\bar{y} = r$ according to the following equation

$$\eta\delta\bar{z}_2^2 + \left[\eta(\mu - \theta\bar{y}) + \delta^2\right]\bar{z}_2 - \delta\theta\bar{y} = 0 \quad \Longrightarrow \quad \mu = \frac{1}{\eta F(r,\Delta_0)}\Big(\eta F(r,\Delta_0) + \delta\Big)\Big(\theta r - \delta F(r,\Delta_0)\Big). \tag{S68}$$

Note that $\theta\bar{y} - \delta\bar{z}_2 = \eta\bar{z}_1\bar{z}_2 \geq 0$, and thus $\theta r - \delta F(r,\Delta_0) \geq 0$ for any admissible fixed point. In this scenario, we substitute for μ in Equation (S63) to yield the sensitivity given by

$$\left|\frac{\partial \bar{y}}{\partial \Delta}\right|_{(\bar{y},\Delta)=(r,\Delta_0)} = \frac{\left|\frac{\partial F(r,\Delta_0)}{\partial \Delta}\right|}{\left|\frac{\partial F(r,\Delta_0)}{\partial \bar{y}}\right| + \frac{\theta}{\delta}\frac{1}{1+\frac{1}{F(r,\Delta_0)}\frac{\theta r - \delta F(r,\Delta_0)}{\eta F(r,\Delta_0)+\delta}}}. \tag{S69}$$

Clearly, in this scenario the sensitivity is a decreasing function in η.

Scenario 2. Fix μ, δ, the steady-state output level $\bar{y} = r$ and the disturbance level $\Delta = \Delta_0$. Then as η is adjusted, θ should be tuned to maintain the steady-state output level at $\bar{y} = r$ according to the following equation

$$\eta\delta\bar{z}_2^2 + \left[\eta(\mu - \theta\bar{y}) + \delta^2\right]\bar{z}_2 - \delta\theta\bar{y} = 0 \quad \Longrightarrow \quad \theta = \frac{F(r,\Delta_0)}{r}\left[\delta + \frac{\eta\mu}{\eta F(r,\Delta_0)+\delta}\right]. \tag{S70}$$

In this scenario, we substitute for θ in Equation (S63) to yield the sensitivity given by

$$\left|\frac{\partial \bar{y}}{\partial \Delta}\right|_{(\bar{y},\Delta)=(r,\Delta_0)} = \frac{\left|\frac{\partial F(r,\Delta_0)}{\partial \Delta}\right|}{\left|\frac{\partial F(r,\Delta_0)}{\partial \bar{y}}\right| + \frac{F(r,\Delta_0)}{r}\frac{1+\frac{1}{\delta}\frac{\eta\mu}{\eta F(r,\Delta_0)+\delta}}{1+\frac{\eta\mu}{(\eta F(r,\Delta_0)+\delta)^2}}}. \tag{S71}$$

Note that

$$\phi(\eta) \triangleq \frac{1+\frac{1}{\delta}\frac{\eta\mu}{\eta F(r,\Delta_0)+\delta}}{1+\frac{\eta\mu}{(\eta F(r,\Delta_0)+\delta)^2}} \quad \Longrightarrow \quad \phi'(\eta) = \frac{\eta\mu F(r,\Delta_0)}{\delta}\frac{\eta\mu + 2\delta\left[\eta F(r,\Delta_0)+\delta\right]}{\left[\eta\mu + (\eta F(r,\Delta_0)+\delta)^2\right]^2} \geq 0. \tag{S72}$$

Therefore, in this scenario the sensitivity is also a decreasing function in η. □

A numerical demonstration of this result is presented in Fig. S6, highlighting the steady-state errors caused by a disturbance and comparing the performance of the non-ideal sAIF controller with that of the filtered proportional controller.

S6.1.2 Comparison between Non-Ideal sAIF and rAIF Controllers

We are now ready to prove Theorem 2 which is repeated here for convenience.

Theorem 2. *For any strictly monotonic regulated network under a constant disturbance Δ, operating in negative feedback with either a non-ideal sAIF or rAIF controller, assume identical controller parameters μ, θ, η, and δ for both controllers (see Fig. 6(a)). At any fixed desired steady-state output $\bar{x}_L$, the steady-state sensitivities to the disturbance satisfy:*

$$\begin{cases} \left|\dfrac{\partial \bar{x}_L}{\partial \Delta}\right|^{sAIF} < \left|\dfrac{\partial \bar{x}_L}{\partial \Delta}\right|^{rAIF} & \text{if} \quad \bar{x}_L > \dfrac{\mu}{\theta} - \dfrac{\delta^2}{\eta\theta}, \\ \left|\dfrac{\partial \bar{x}_L}{\partial \Delta}\right|^{sAIF} > \left|\dfrac{\partial \bar{x}_L}{\partial \Delta}\right|^{rAIF} & \text{if} \quad \bar{x}_L < \dfrac{\mu}{\theta} - \dfrac{\delta^2}{\eta\theta}, \end{cases}$$

assuming the absolute value of the actuation gains of both controllers are matched (see Fig. 6(c)).

Proof. Consider an arbitrary process $\mathcal{P}_\Delta$ infiltrated by a constant disturbance Δ, and whose input and output are denoted by u and y, respectively. The dynamics of the closed-loop systems with either the non-ideal sAIF controller $\mathcal{C}_s$ or rAIF controllers $\mathcal{C}_r$ are given by the following equations:

$$\begin{aligned} &\textbf{Process:} && y = \mathcal{P}_\Delta(u) && \iff && \begin{cases} \dot{x} = f_\Delta(x,u) \\ y = g_\Delta(x,u) \end{cases} \\ &\textbf{Non-Ideal sAIF Controller:} && u = \mathcal{C}_s(y) && \iff && \begin{cases} \dot{z}_1^s = \mu - \eta z_1^s z_2^s - \delta z_1^s \\ \dot{z}_2^s = \theta y - \eta z_1^s z_2^s - \delta z_2^s \\ u = h_s(z_2^s) \end{cases} \\ &\textbf{Non-Ideal rAIF Controller:} && u = \mathcal{C}_r(y) && \iff && \begin{cases} \dot{z}_1^r = \mu - \eta z_1^r z_2^r - \delta z_1^r \\ \dot{z}_2^r = \theta y - \eta z_1^r z_2^r - \delta z_2^r \\ u = h_r(z_1^r). \end{cases} \end{aligned} \tag{S73}$$

Here, f_Δ, g_Δ, h_s and h_r are continuously differentiable functions, with h_s and h_r being strictly monotonic. Observe that all controller parameters μ, θ, η and δ are kept the same for both controllers.

Let $\mathbb{U}_s$ and $\mathbb{U}_r$ be the sets of feasible inputs associated with h_s and h_r, respectively. For a given disturbance Δ and desired steady-state output $\bar{y}$ that is admissible for both controllers, i.e. $\bar{y} \in \mathcal{R}(\mathcal{P}_\Delta, \mathbb{U}_s) \cap \mathcal{R}(\mathcal{P}_\Delta, \mathbb{U}_r)$, there exists a $\bar{u} \in \mathbb{U}_s \cap \mathbb{U}_r$ such that $\bar{y} = \bar{\mathcal{P}}_\Delta(\bar{u})$. Furthermore, since $\bar{u} \in \mathbb{U}_s \cap \mathbb{U}_r$, there exists a $\bar{z}_2^s \geq 0$ such that $h_s(\bar{z}_2^s) = \bar{u}$ and a $\bar{z}_1^r \geq 0$ such that $h_r(\bar{z}_1^r) = \bar{u}$. Therefore, we have

$$\bar{u} = h_s(\bar{z}_2^s) = h_r(\bar{z}_1^r) = \bar{\mathcal{P}}_\Delta^{-1}(\bar{y}), \tag{S74}$$

where the inverse exists due to the strict monotonicity assumption. Furthermore, at steady state, the following equations are satisfied

$$\begin{cases} \mu - \eta \bar{z}_1^s \bar{z}_2^s - \delta \bar{z}_1^s = 0 \\ \theta \bar{y} - \eta \bar{z}_1^s \bar{z}_2^s - \delta \bar{z}_2^s = 0 \end{cases} \quad \text{and} \quad \begin{cases} \mu - \eta \bar{z}_1^r \bar{z}_2^r - \delta \bar{z}_1^r = 0 \\ \theta \bar{y} - \eta \bar{z}_1^r \bar{z}_2^r - \delta \bar{z}_2^r = 0. \end{cases} \tag{S75}$$

Then we have

$$\begin{aligned} \bar{z}_1^r = \bar{z}_1^s &= \frac{1}{2}\left[\frac{\mu - \theta\bar{y}}{\delta} - \frac{\delta}{\eta} + \sqrt{\left(\frac{\mu - \theta\bar{y}}{\delta} - \frac{\delta}{\eta}\right)^2 + \frac{4\mu}{\eta}}\right] && \triangleq \bar{z}_1 \\ \bar{z}_2^r = \bar{z}_2^s &= \frac{1}{2}\left[\frac{\theta\bar{y} - \mu}{\delta} - \frac{\delta}{\eta} + \sqrt{\left(\frac{\theta\bar{y} - \mu}{\delta} - \frac{\delta}{\eta}\right)^2 + \frac{4\theta\bar{y}}{\eta}}\right] && \triangleq \bar{z}_2. \end{aligned} \tag{S76}$$

Therefore, having the same setpoint and actuation gains for both controllers are translated to the following equations

$$\begin{cases} \bar{z}_1^s = \bar{z}_1^r \triangleq \bar{z}_1 \\ \bar{z}_2^s = \bar{z}_2^r \triangleq \bar{z}_2, \end{cases} \quad \begin{cases} \bar{z}_1 = h_r^{-1} \circ \bar{\mathcal{P}}_\Delta^{-1}(\bar{y}) \triangleq F_r(\bar{y}, \Delta) \\ \bar{z}_2 = h_s^{-1} \circ \bar{\mathcal{P}}_\Delta^{-1}(\bar{y}) \triangleq F_s(\bar{y}, \Delta), \end{cases} \quad \text{and} \quad |h_r'(\bar{z}_1)| = |h_s'(\bar{z}_2)| = G. \tag{S77}$$

Next, we calculate the steady-state sensitivities of the output with respect to the disturbance for both controllers. For the rAIF controller we proceed by dropping the bar for convenience. We have

$$\begin{cases} \mu - \eta z_1 z_2 - \delta z_1 = 0 \\ \theta y - \eta z_1 z_2 - \delta z_2 = 0 \end{cases} \implies \eta\delta z_1^2 - \left[\eta(\mu - \theta y) - \delta^2\right] z_1 - \delta\mu = 0 \qquad \text{with} \qquad z_1 = F_r(y, \Delta). \tag{S78}$$

The sensitivity of the steady-state output with respect to disturbances can be implicitly calculated as follows

$$2\eta\delta z_1 \frac{\partial z_1}{\partial \Delta} + \eta\theta \frac{\partial y}{\partial \Delta} z_1 - \left[\eta(\mu - \theta y) - \delta^2\right] \frac{\partial z_1}{\partial \Delta} = 0 \quad \text{with} \quad \begin{cases} z_1 = F_r(y, \Delta) \\ \dfrac{\partial z_1}{\partial \Delta} = \dfrac{\partial F_r(y,\Delta)}{\partial y} \dfrac{\partial y}{\partial \Delta} + \dfrac{\partial F_r(y,\Delta)}{\partial \Delta}. \end{cases} \tag{S79}$$

We proceed with some algebraic manipulations to obtain an expression for $\frac{\partial y}{\partial \Delta}$

$$\begin{aligned}
\left[2\eta\delta z_1 + \delta^2 - \eta(\mu - \theta y)\right] \frac{\partial z_1}{\partial \Delta} + \eta\theta z_1 \frac{\partial y}{\partial \Delta} &= 0 \\
\left[\delta(\eta z_1 + \delta) - \eta(\mu - \theta y - \delta z_1)\right] \frac{\partial z_1}{\partial \Delta} + \eta\theta z_1 \frac{\partial y}{\partial \Delta} &= 0 \\
\left[\delta(\eta z_1 + \delta) + \eta\delta z_2\right] \frac{\partial z_1}{\partial \Delta} + \eta\theta z_1 \frac{\partial y}{\partial \Delta} &= 0 \\
\left[\delta(\eta z_1 + \delta) + \eta \frac{\delta\theta y}{\eta z_1 + \delta}\right] \frac{\partial z_1}{\partial \Delta} + \eta\theta z_1 \frac{\partial y}{\partial \Delta} &= 0 \\
\delta\left[1 + \frac{\eta\theta y}{(\eta z_1 + \delta)^2}\right] \frac{\partial z_1}{\partial \Delta} + \frac{\eta\theta z_1}{\eta z_1 + \delta} \frac{\partial y}{\partial \Delta} &= 0 \\
\delta\left[1 + \frac{\eta\theta y}{(\eta z_1 + \delta)^2}\right] \left[\frac{\partial F_r(y,\Delta)}{\partial y} \frac{\partial y}{\partial \Delta} + \frac{\partial F_r(y,\Delta)}{\partial \Delta}\right] + \frac{\eta\theta z_1}{\eta z_1 + \delta} \frac{\partial y}{\partial \Delta} &= 0 \\
\left[\delta\left(1 + \frac{\eta\theta y}{(\eta z_1 + \delta)^2}\right) \frac{\partial F_r(y,\Delta)}{\partial y} + \frac{\eta\theta z_1}{\eta z_1 + \delta}\right] \frac{\partial y}{\partial \Delta} &= -\delta\left(1 + \frac{\eta\theta y}{(\eta z_1 + \delta)^2}\right) \frac{\partial F_r(y,\Delta)}{\partial \Delta} \\
\implies \frac{\partial y}{\partial \Delta} &= -\frac{\frac{\partial F_r(y,\Delta)}{\partial \Delta}}{\frac{\partial F_r(y,\Delta)}{\partial y} + \frac{\theta}{\delta} \frac{\eta z_1(\eta z_1 + \delta)}{(\eta z_1 + \delta)^2 + \eta\theta y}}.
\end{aligned} \tag{S80}$$

Note that

$$\frac{\partial F_r(y,\Delta)}{\partial y} = \frac{1}{h_r'\left(h_r^{-1} \circ \bar{\mathcal{P}}_\Delta^{-1}(y)\right) \bar{\mathcal{P}}_\Delta'\left(\bar{\mathcal{P}}_\Delta^{-1}(y)\right)} > 0, \tag{S81}$$

since we have a negative feedback configuration. Therefore, we have

$$\left|\frac{\partial \bar{y}}{\partial \Delta}\right| = \frac{\left|\frac{\partial F_r(y,\Delta)}{\partial \Delta}\right|}{\left|\frac{\partial F_r(y,\Delta)}{\partial y}\right| + \frac{\theta}{\delta} \frac{\eta z_1(\eta z_1 + \delta)}{(\eta z_1 + \delta)^2 + \eta\theta y}}. \tag{S82}$$

The calculations for the sAIF controller was already carried out in the proof of Theorem 1, and so the results are summarized in the following equations

$$\begin{aligned}
\textbf{sAIF:} \quad \left|\frac{\partial \bar{y}}{\partial \Delta}\right|_{(\bar{y},\Delta)=(r,\Delta_0)} &= \frac{\left|\frac{\partial F_s(r,\Delta_0)}{\partial \Delta}\right|}{\left|\frac{\partial F_s(r,\Delta_0)}{\partial \bar{y}}\right| + \phi_s} \quad \text{with} \quad \phi_s \triangleq \frac{\theta}{\delta} \frac{1}{1 + \frac{\eta\mu}{(\eta\bar{z}_2 + \delta)^2}} \\
\textbf{rAIF:} \quad \left|\frac{\partial \bar{y}}{\partial \Delta}\right|_{(\bar{y},\Delta)=(r,\Delta_0)} &= \frac{\left|\frac{\partial F_r(r,\Delta_0)}{\partial \Delta}\right|}{\left|\frac{\partial F_r(r,\Delta_0)}{\partial \bar{y}}\right| + \phi_r} \quad \text{with} \quad \phi_r \triangleq \frac{\theta}{\delta} \frac{\eta\bar{z}_1(\eta\bar{z}_1 + \delta)}{(\eta\bar{z}_1 + \delta)^2 + \eta\theta\bar{y}}.
\end{aligned} \tag{S83}$$

First, observe that

$$\begin{aligned}\left|\frac{\partial F_r(r,\Delta)}{\partial y}\right| &= \left|\frac{1}{h_r'\left(h_r^{-1}\circ\bar{\mathcal{P}}_\Delta^{-1}(r)\right)\bar{\mathcal{P}}_\Delta'\left(\bar{\mathcal{P}}_\Delta^{-1}(r)\right)}\right| \\ &= \left|\frac{1}{h_r'(\bar{z}_1)\bar{\mathcal{P}}_\Delta'\left(\bar{\mathcal{P}}_\Delta^{-1}(r)\right)}\right| \\ &= \left|\frac{1}{h_s'(\bar{z}_2)\bar{\mathcal{P}}_\Delta'\left(\bar{\mathcal{P}}_\Delta^{-1}(r)\right)}\right| \\ &= \left|\frac{1}{h_s'\left(h_s^{-1}\circ\bar{\mathcal{P}}_\Delta^{-1}(r)\right)\bar{\mathcal{P}}_\Delta'\left(\bar{\mathcal{P}}_\Delta^{-1}(r)\right)}\right| = \left|\frac{\partial F_s(r,\Delta_0)}{\partial y}\right|,\end{aligned} \tag{S84}$$

and similarly

$$\left|\frac{\partial F_r(r,\Delta_0)}{\partial \Delta}\right| = \left|\frac{\partial F_s(r,\Delta_0)}{\partial \Delta}\right|. \tag{S85}$$

Hence, we are left with comparing ϕ_s and ϕ_r. We have

$$\begin{aligned}\phi_r - \phi_s &= \frac{\theta}{\delta}\left[\frac{\eta\bar{z}_1(\eta\bar{z}_1+\delta)}{(\eta\bar{z}_1+\delta)^2+\eta\theta\bar{y}} - \frac{1}{1+\frac{\eta\mu}{(\eta\bar{z}_2+\delta)^2}}\right] \\ &= \frac{\theta}{\delta}\left[\frac{\eta\bar{z}_1}{\eta\bar{z}_1+\delta+\frac{\eta\theta\bar{y}}{\eta\bar{z}_1+\delta}} - \frac{\eta\bar{z}_2+\delta}{\eta\bar{z}_2+\delta+\frac{\eta\mu}{\eta\bar{z}_2+\delta}}\right].\end{aligned} \tag{S86}$$

But recall that $\bar{z}_1 = \frac{\mu}{\eta\bar{z}_1+\delta}$ and $\bar{z}_2 = \frac{\theta\bar{y}}{\eta\bar{z}_1+\delta}$. Then

$$\begin{aligned}\phi_r - \phi_s &= \frac{\theta}{\delta}\left[\frac{\eta\bar{z}_1}{\eta\bar{z}_1+\delta+\eta\bar{z}_2} - \frac{\eta\bar{z}_2+\delta}{\eta\bar{z}_1+\delta+\eta\bar{z}_1}\right] \\ &= \frac{\theta}{\delta}\frac{\eta(\bar{z}_1-\bar{z}_2)-\delta}{\eta(\bar{z}_1+\bar{z}_2)+\delta} \\ &= \frac{\theta}{\delta}\frac{\eta\frac{\mu-\theta\bar{y}}{\delta}-\delta}{\eta(\bar{z}_1+\bar{z}_2)+\delta} \\ &= \frac{\theta}{\delta^2}\frac{\eta(\mu-\theta\bar{y})-\delta^2}{\eta(\bar{z}_1+\bar{z}_2)+\delta}.\end{aligned} \tag{S87}$$

Hence, $\phi_r > \phi_s$ iff $\bar{y} < \frac{\mu}{\theta} - \frac{\delta^2}{\eta\theta}$. Therefore,

$$\left|\frac{\partial\bar{y}}{\partial\Delta}\right|^{\text{rAIF}}_{(\bar{y},\Delta)=(r,\Delta_0)} < \left|\frac{\partial\bar{y}}{\partial\Delta}\right|^{\text{sAIF}}_{(\bar{y},\Delta)=(r,\Delta_0)} \qquad \Longleftrightarrow \qquad \bar{y} < \frac{\mu}{\theta} - \frac{\delta^2}{\eta\theta}. \tag{S88}$$

□

S6.2 Noise Analysis for the Non-Ideal sAIF Controller Using Linear Noise Approximation

Consider the simple birth-death process controlled by the non-ideal sAIF controller depicted in Fig. 6(a). The closed-loop can now be modeled as a SCRN represented by the following stoichiometry matrix and propensity function

$$S = \begin{bmatrix}1 & -1 & 0 & 0 & 0 & 0 & 0\\ 0 & 0 & 1 & 0 & -1 & -1 & 0\\ 0 & 0 & 0 & 1 & -1 & 0 & -1\end{bmatrix}, \qquad \lambda(x,z_1,z_2) = \begin{bmatrix}h(z_2) & \gamma x & \mu & \theta x & \eta z_1 z_2 & \delta z_1 & \delta z_2\end{bmatrix}^T. \tag{S89}$$

The goal here is to derive the sensitivity of the stationary coefficient of variation of the output $\text{CV}\left[\bar{X}\right]$ to the sequestration rate η for a fixed setpoint $\mathbb{E}\left[\bar{X}\right] = r$. LNA provides algebraic equations that approximate the stationary mean $\left(\mathbb{E}\left[\bar{X}\right], \mathbb{E}\left[\bar{Z}_1\right], \mathbb{E}\left[\bar{Z}_2\right]\right)$ and covariance $\bar{\Sigma}$ of the closed-loop state vector $\begin{bmatrix}X & Z_1 & Z_2\end{bmatrix}^T$ given by

$$\begin{cases} h\left(\mathbb{E}\left[\bar{Z}_2\right]\right) - \gamma\mathbb{E}\left[\bar{X}\right] \approx 0 \\ \mu - \eta\mathbb{E}\left[\bar{Z}_1\right]\mathbb{E}\left[\bar{Z}_2\right] - \delta\mathbb{E}\left[\bar{Z}_1\right] \approx 0 \\ \theta\mathbb{E}\left[\bar{X}\right] - \eta\mathbb{E}\left[\bar{Z}_1\right]\mathbb{E}\left[\bar{Z}_2\right] - \delta\mathbb{E}\left[\bar{Z}_2\right] \approx 0 \\ A\bar{\Sigma} + \bar{\Sigma}A^T + W \approx 0, \end{cases} \tag{S90}$$

where $A \triangleq \begin{bmatrix} -\gamma & 0 & -\sigma_2 \\ 0 & -\eta\mathbb{E}[\bar{Z}_2] - \delta & -\eta\mathbb{E}[\bar{Z}_1] \\ \theta & -\eta\mathbb{E}[\bar{Z}_2] & -\eta\mathbb{E}[\bar{Z}_1] - \delta \end{bmatrix}$,
$W = \begin{bmatrix} h\left(\mathbb{E}[\bar{Z}_2]\right) + \gamma\mathbb{E}[\bar{X}] & 0 & 0 \\ 0 & \mu + \eta\mathbb{E}[\bar{Z}_1]\,\mathbb{E}[\bar{Z}_2] + \delta\mathbb{E}[\bar{Z}_1] & \eta\mathbb{E}[\bar{Z}_1]\,\mathbb{E}[\bar{Z}_2] \\ 0 & \eta\mathbb{E}[\bar{Z}_1]\,\mathbb{E}[\bar{Z}_2] & \theta\mathbb{E}[\bar{X}] + \eta\mathbb{E}[\bar{Z}_1]\,\mathbb{E}[\bar{Z}_2] + \delta\mathbb{E}[\bar{Z}_2] \end{bmatrix}$ and $\sigma_2 \triangleq -h'\left(\mathbb{E}[\bar{Z}_2]\right)$.
Using the first three equations in Equation (S90) and fixing the stationary output to $\mathbb{E}[\bar{X}] = r$, we can write

$$h\left(\mathbb{E}[\bar{Z}_2]\right) = \gamma\mathbb{E}[\bar{X}] \qquad \mathbb{E}[\bar{Z}_1] = \frac{\mu}{\eta\mathbb{E}[\bar{Z}_2] + \delta} \qquad \text{and} \qquad \theta = \frac{\mathbb{E}[\bar{Z}_2]}{r}\left(\delta + \frac{\eta\mu}{\eta\mathbb{E}[\bar{Z}_2] + \delta}\right).$$

Note that the last equation provides a tuning scheme for θ that yields, up to an LNA approximation, a fixed stationary output $\mathbb{E}[\bar{X}] = r$ as η is varied. Hence we can get rid of $h\left(\mathbb{E}[\bar{Z}_2]\right), \theta$, and $\mathbb{E}[\bar{Z}_1]$ in A and W to express them in terms of r and $\mathbb{E}[\bar{Z}_2]$ as

$$A = \begin{bmatrix} -\gamma & 0 & -\sigma_2 \\ 0 & -\eta\mathbb{E}[\bar{Z}_2] - \delta & -\frac{\eta\,\mu}{\eta\mathbb{E}[\bar{Z}_2]+\delta} \\ \frac{\mathbb{E}[\bar{Z}_2]}{r}\left(\delta + \frac{\eta\mu}{\eta\mathbb{E}[\bar{Z}_2]+\delta}\right) & -\eta\mathbb{E}[\bar{Z}_2] & -\frac{\eta\,\mu}{\eta\mathbb{E}[\bar{Z}_2]+\delta} - \delta \end{bmatrix}$$

$$W = \begin{bmatrix} 2\,\gamma\,r & 0 & 0 \\ 0 & 2\,\mu & \frac{\eta\,\mu\mathbb{E}[\bar{Z}_2]}{\eta\mathbb{E}[\bar{Z}_2]+\delta} \\ 0 & \frac{\eta\,\mu\mathbb{E}[\bar{Z}_2]}{\eta\mathbb{E}[\bar{Z}_2]+\delta} & 2\mathbb{E}[\bar{Z}_2]\left(\frac{\eta\mu}{\eta\mathbb{E}[\bar{Z}_2]+\delta} + \delta\right) \end{bmatrix}.$$

Note that, up to an LNA approximation, $\mathbb{E}[\bar{Z}_2]$ is independent of η when the stationary output is fixed $\mathbb{E}[\bar{X}] = r$. Using the expressions for A and W, the system of linear equations $A\bar{\Sigma} + \bar{\Sigma}A^T + W = 0$ can be solved for $\bar{\Sigma}$. Due to the complexity of the calculations, Matlab's symbolic toolbox is employed to compute $\bar{\Sigma}$, specifically its first entry, which represents the stationary variance of the output, $\mathrm{Var}[\bar{X}]$. The MATLAB code can be found at the following Github repository https://github.com/Maurice-Filo/Sensor-Based-Biomolecular-Integral-Controllers. While the full expression for $\bar{\Sigma}$ is complicated and not presented here, the derivative of the variance with respect to η at $\eta = 0$ is given by:

$$\left.\frac{\partial \mathrm{Var}[\bar{X}]}{\partial \eta}\right|_{\eta=0,\,\mathbb{E}[\bar{X}]=r} = -\frac{\mathbb{E}[\bar{Z}_2]\,\mu\,r\,\left|h'(\mathbb{E}[\bar{Z}_2])\right|\,\left(\gamma + \left|h'(\mathbb{E}[\bar{Z}_2])\right|\right)}{\delta\,(\delta+\gamma)^2\,\left(\mathbb{E}[\bar{Z}_2]\,\left|h'(\mathbb{E}[\bar{Z}_2])\right| + \gamma\,r\right)} < 0. \tag{S91}$$

This indicates that as η increases from zero (the filtered P controller case) while maintaining a fixed output level, the variance—and consequently the coefficient of variation (CV)—must decrease. This analytical approximation complements the numerical findings in Fig. 6(e), which show a decrease in CV as η increases from zero.

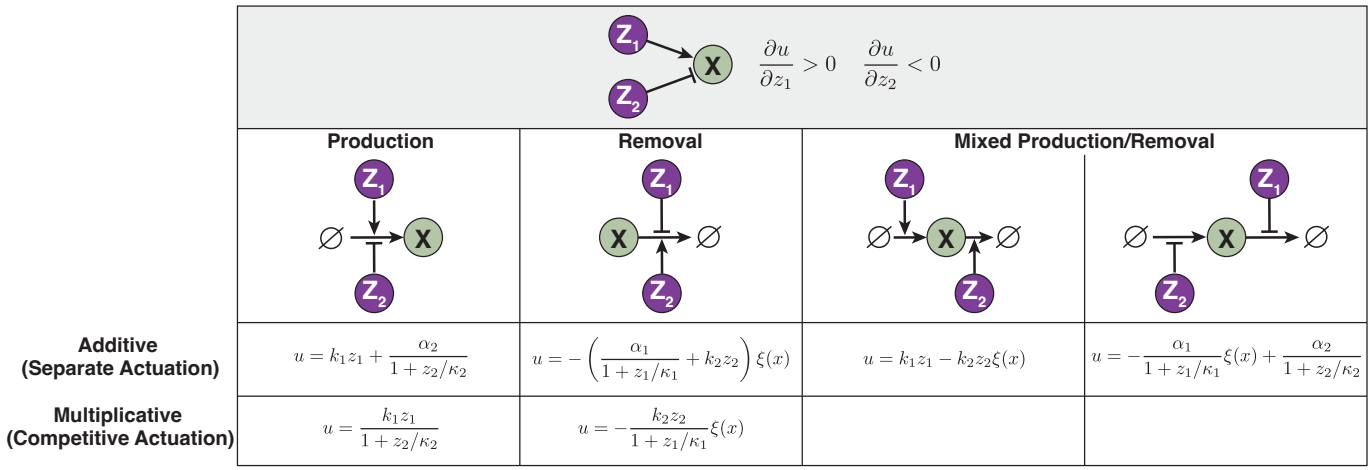

Figure S1: Actuation with multiple species. This extends Fig. 2(b) to the case where two controller species $\mathbf{Z_1}$ and $\mathbf{Z_2}$ actuate $\mathbf{X}$ positively and negatively, respectively. The implementations can once again be via production and/or removal reactions. Furthermore, two particular classes of functional forms are shown here, where the effects of $\mathbf{Z_1}$ and $\mathbf{Z_2}$ enter additively (such as separate promoters for the same gene) or multiplicatively (such as competition over the same promoter).

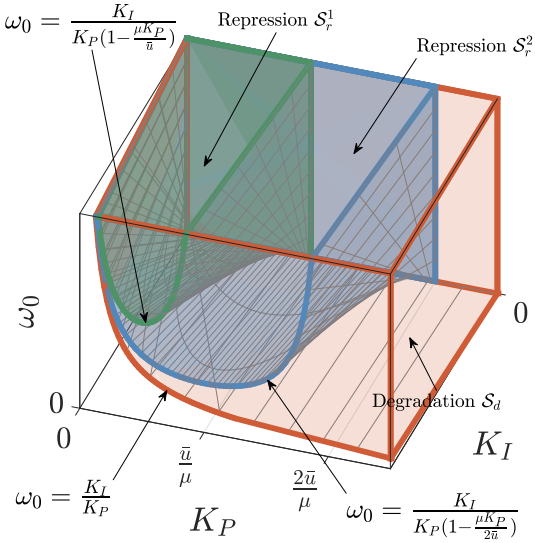

Figure S2: Filtered-PI Coverage. The colored regions depict the achievable PI gains (K_P, K_I) and cutoff frequency ω_0 by adjusting the corresponding biomolecular parameters. These regions are color-coded to represent different actuation functions h, modeling three distinct negative actuation mechanisms: repression Equation (S13) with and without cooperativity in green $(n = 1)$ and blue $(n = 2)$, respectively, and degradation Equation (S19) in red. Note that $\bar{u}$ represents the steady-state supporting input necessary to achieve the desired setpoint, and its value depends solely on the plant and the desired setpoint. The span of achievable filtered-PI parameters for repression and degradation actuations are respectively calculated as $\mathcal{S}_r^n$ in Equation (S18) and $\mathcal{S}_d$ in Equation (S22), and they are shown to satisfy $\mathcal{S}_r^n \subset S_r^{n+1} \subset \mathcal{S}_d$. This demonstrates that degradation provides greater tuning flexibility than repression actuation. It also demonstrates that cooperativity helps in expanding the achievable gains and cutoff frequency.

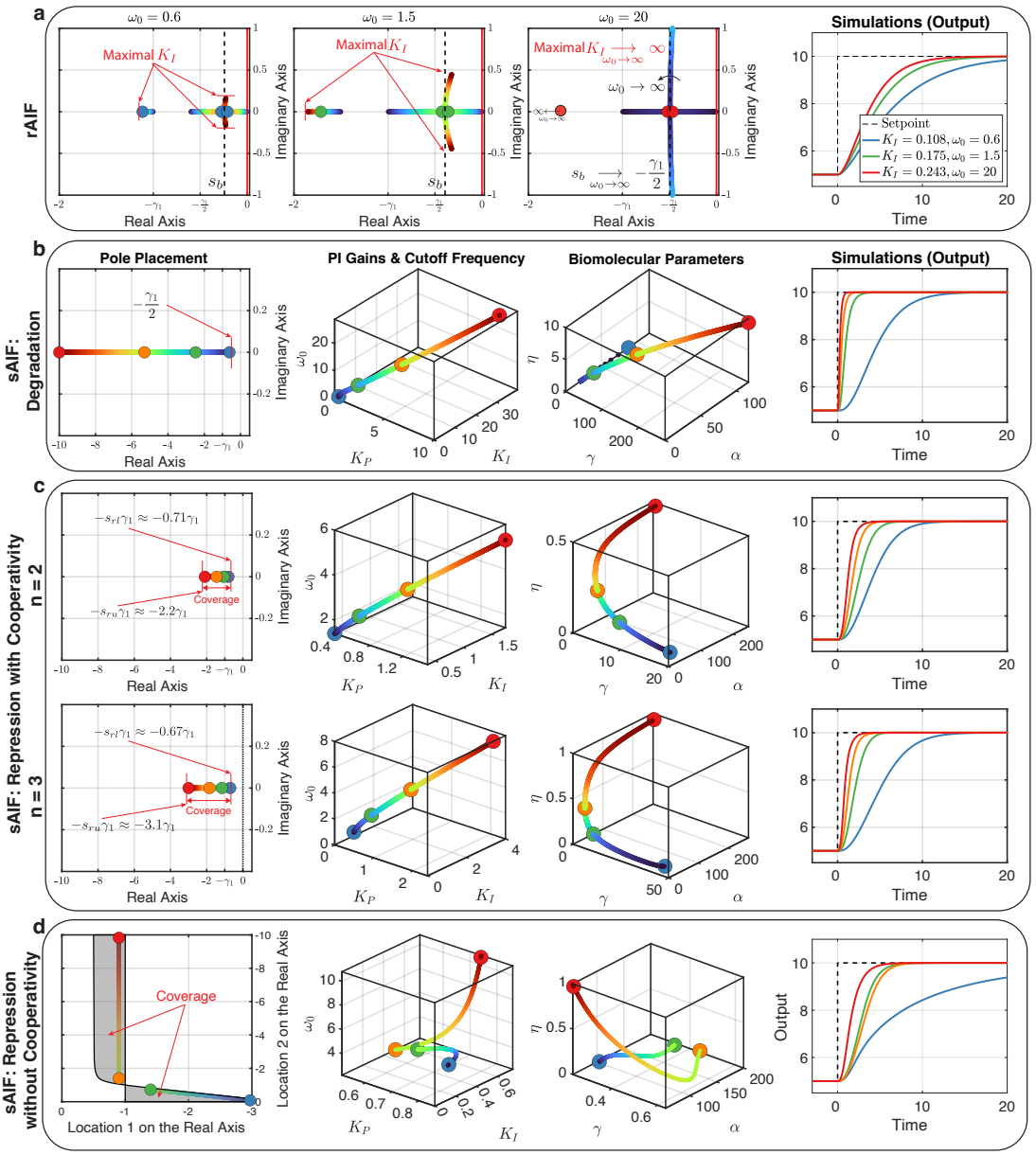

Figure S3: Dynamic Performance Assessment. A birth-death process (see Fig. 5(a), left) is controlled, as a case study, by rAIF and sAIF. The control action is denoted by u and the degradation rate of the process is denoted by γ_1. (a) Performance limitation of rAIF. Positive actuation by $\mathbf{Z_1}$ (i.e. $u = kz_1$) yields a response that cannot be sped up beyond a certain threshold without inflicting oscillations. The three plots to the left depict the root-locus of the linearized closed-loop dynamics in the complex plane for three values of the cutoff frequency ω_0 as the integral gain K_I is increased from zero up to its upper bound given in Equation (S12). Note that s_b, calculated analytically in Equation (S25), denotes the breaking point where two eigenvalues meet on the real axis and break away to become complex conjugates. As ω_0 is increased, one real eigenvalue moves more to the left and the breaking point s_b tends to $-\gamma_1/2$. This indicates that the dominant eigenvalue is confined (by the breaking point s_b) within a small region close to the imaginary axis when γ_1 is small, and thus imposing a limitation on the achievable performance as demonstrated in the simulations shown in the right plot. (b) and (c) Design flexibility offered by sAIF. Giving rise to a filtered-PI controller, sAIF offers more flexibility in achieving superior performance compared to rAIF. These two panels show the steps of a pole-placement control design problem where the three dominant poles are placed on the real axis of the left-half plane to ensure a stable and non-oscillating response. The design problems start by picking the poles, then computing the PI gains and cutoff frequency, and finally computing the biomolecular parameters that allow us to obtain the nonlinear simulations to the right. With degradation actuation in Panel (b), one can place the eigenvalues arbitrarily as far to the left as desired and thus achieving a response that is as fast as desired without overshoots or oscillations. In contrast, with repression in Panel (c), there is a restriction on how far to the left the poles can be placed. However, this restriction can be mitigated by introducing higher cooperativity. (d) Repression without cooperativity. Without cooperativity, the three poles cannot be placed in the same location. To this end we place them at two locations on the real axis. The shaded regions in the left plot depicts the feasible locations that are constrained by the PI coverages (see SI Section S4). These regions indicate that one cannot place all the poles to the left of $-\gamma_1$ which still yields a better performance than rAIF, but cannot outperform those presented in Panels (b) and (c). The numerical values of the parameters are $\gamma_1 = 1, \mu = 5, \theta = 1, \kappa_1 = 10^{-5}$. To change the setpoint at $t = 0$, μ is doubled.

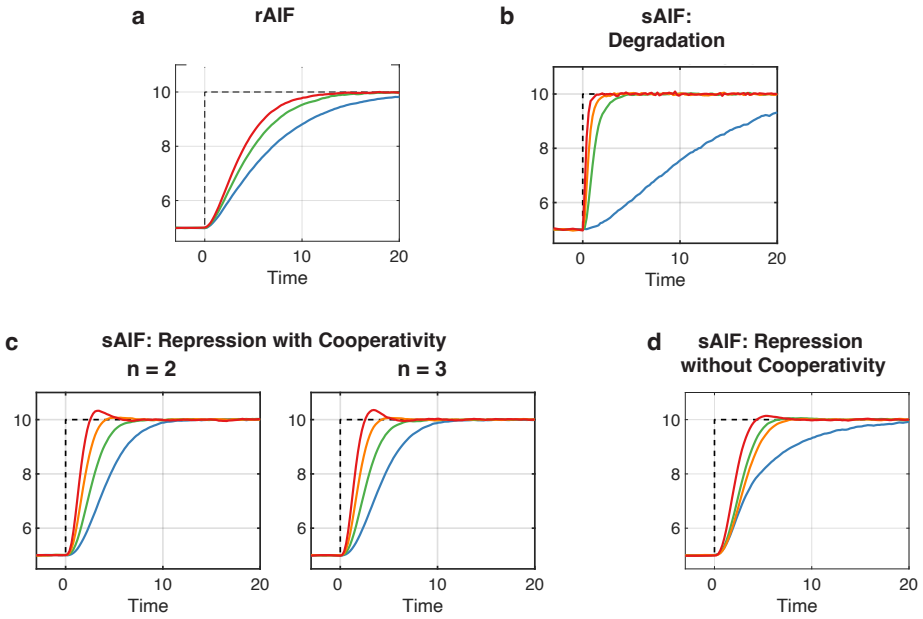

Figure S4: Dynamics of Average Concentrations in the Stochastic Setting. This figure presents the stochastic counterpart to the simulations shown in Figs. 4 and S3. Biomolecular parameters are taken directly from the root locus analysis performed in the deterministic setting, and stochastic simulations—averaged over 10^5 trajectories—are used to track the evolution of mean concentrations. The results confirm that the same dynamic patterns persist under stochasticity, with a slight overshoot observed in some cases, which can be mitigated by selecting less aggressive pole placements.

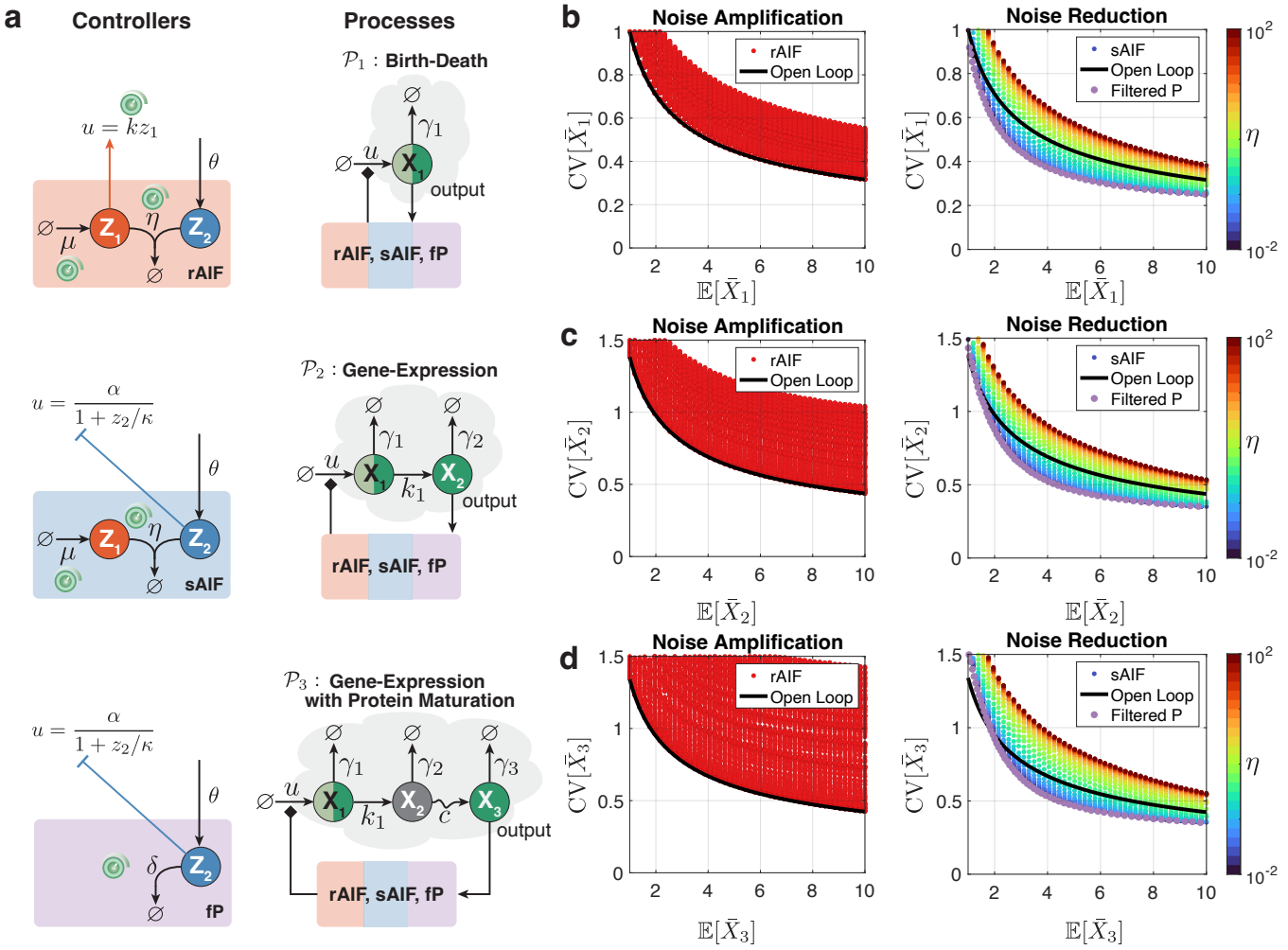

Figure S5: Controlling three processes with rAIF, sAIF and fP controllers. (a) The processes to be controlled are denoted by $\mathcal{P}_1, \mathcal{P}_2$, and $\mathcal{P}_3$. $\mathcal{P}_1$ is a birth-death process identical to that in Fig. 5(a). $\mathcal{P}_2$ is a process with two species which can be used to model gene expression with $\mathbf{X_1}$ being the mRNA while $\mathbf{X_2}$ being the protein. For this model, k_1 is the translation rate while γ_1 and γ_2 are the removal rates. Finally $\mathcal{P}_3$ is similar to $\mathcal{P}_2$, but with an additional maturation step where $\mathbf{X_2}$ is converted to $\mathbf{X_3}$ at a rate c. Note that all arrows pointing to a species indicate catalytic production reactions except the curved arrow which indicates a conversion reaction. Furthermore, the square shaped arrowhead indicates either activation or repression. These processes are controlled by three different controllers: rAIF and sAIF and a fP controller. (b), (c) and (d) displays the relationship between the coefficients of variation and expectations at stationarity for the outputs. The left plots correspond to rAIF, while the right plots correspond to sAIF and fP feedback. The solid black lines are calculated analytically using an equation similar to Equation (13) given by $\mathrm{CV}[\bar{X}_L] = \sqrt{\frac{1+\beta}{\mathbb{E}[\bar{X}_L]}}$ with $\beta = 0, \frac{k_1}{\gamma_1+\gamma_2}$ and $\frac{k_1 c(c+\gamma_1+\gamma_2+\gamma_3)}{(\gamma_1+\gamma_3)(\gamma_1+\gamma_2+c)(\gamma_2+c+\gamma_3)}$ for $\mathcal{P}_1, \mathcal{P}_2$ and $\mathcal{P}_3$, respectively. In contrast, the remaining data points are computed empirically through the stochastic simulation algorithm[1], generating $10^4 - 10^5$ trajectories on the Euler cluster (https://scicomp.ethz.ch/wiki/Euler). Numerical values for $\mathcal{P}_1$ are $\gamma_1 = 0.1$. Numerical values for $\mathcal{P}_2$ are: $\gamma_1 = k_1 = 1, \gamma_2 = 0.1$. Numerical values for $\mathcal{P}_3$ are: $\gamma_1 = k_1 = c = 1, \gamma_2 = \gamma_3 = 0.1$. The controller parameter values are as follows: $\alpha = 2, \theta = 1, \kappa = 0.05, \eta \in [10^{-2}, 10^2], k \in [10^{-3}, 1], \delta \in [0.1, 20], \mu \in [1, 10]$.

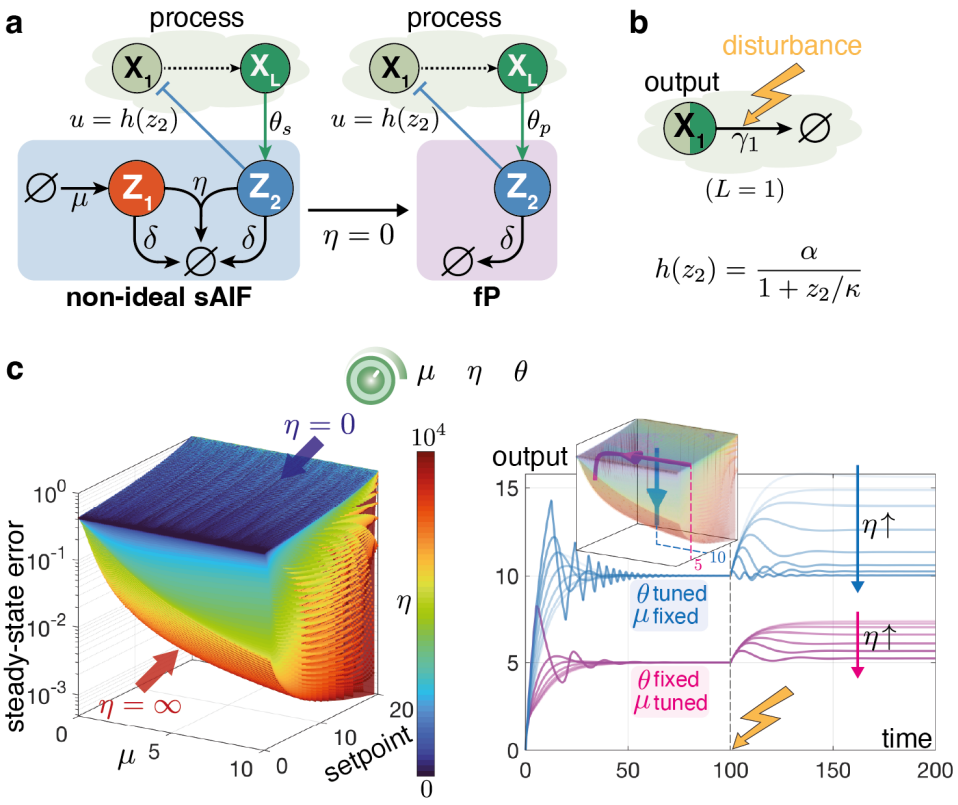

Figure S6: Steady-state error comparison: non-ideal sAIF controller vs. filtered proportional controller. (a) Closed-loop networks illustrating the non-ideal sAIF controller and the filtered proportional controller. The topology of the non-ideal sAIF controller differs from the ideal sAIF controller shown in Fig. 3, as the controller species $\mathbf{Z_1}$ and $\mathbf{Z_2}$ are subject to dilution at a rate δ. (b) Example process and actuation mechanism used in numerical simulations. The process is a simple birth-death system with $L = 1$ species, where the disturbance perturbs the degradation rate γ_1 of the output. Both controllers share the same actuation mechanism, modeled by the function h, with α representing the maximal production rate and κ the dissociation constant of the repressor $\mathbf{Z_2}$. (c) Numerical demonstration of steady-state errors. In these simulations, the example process is regulated by the non-ideal sAIF controller with fixed parameters: $\gamma_1 = \delta = 0.1$, $\alpha = 2$, and $\kappa = 0.05$. The swept parameters are $\mu \in [0, 10]$, $\eta \in [0, 10^4]$, and $\theta \in [10^{-5}, 10]$. Note that when $\eta = 0$, the system reduces to the filtered proportional controller. A disturbance is applied by halving the degradation rate. The 3D plot on the left illustrates the steady-state error caused by the disturbance as μ, θ, and η are varied. For each combination of these parameters, the steady-state error and the corresponding setpoint are computed and represented as points in the plot. The results indicate that, for any given setpoint, the filtered proportional controller ($\eta = 0$) exhibits the highest steady-state error. As η increases, the steady-state error decreases, with the minimum error achieved as $\eta \to \infty$. The plot on the right provides detailed examples for specific parameter values. The blue responses correspond to a fixed $\mu = 10$, with θ adjusted to maintain a pre-disturbance setpoint of 10. The magenta responses correspond to a fixed $\theta = 5$, with μ tuned to achieve a pre-disturbance setpoint of 5. These examples highlight the dependence of steady-state error on parameter tuning and demonstrate the improved performance of the non-ideal sAIF controller as η increases.

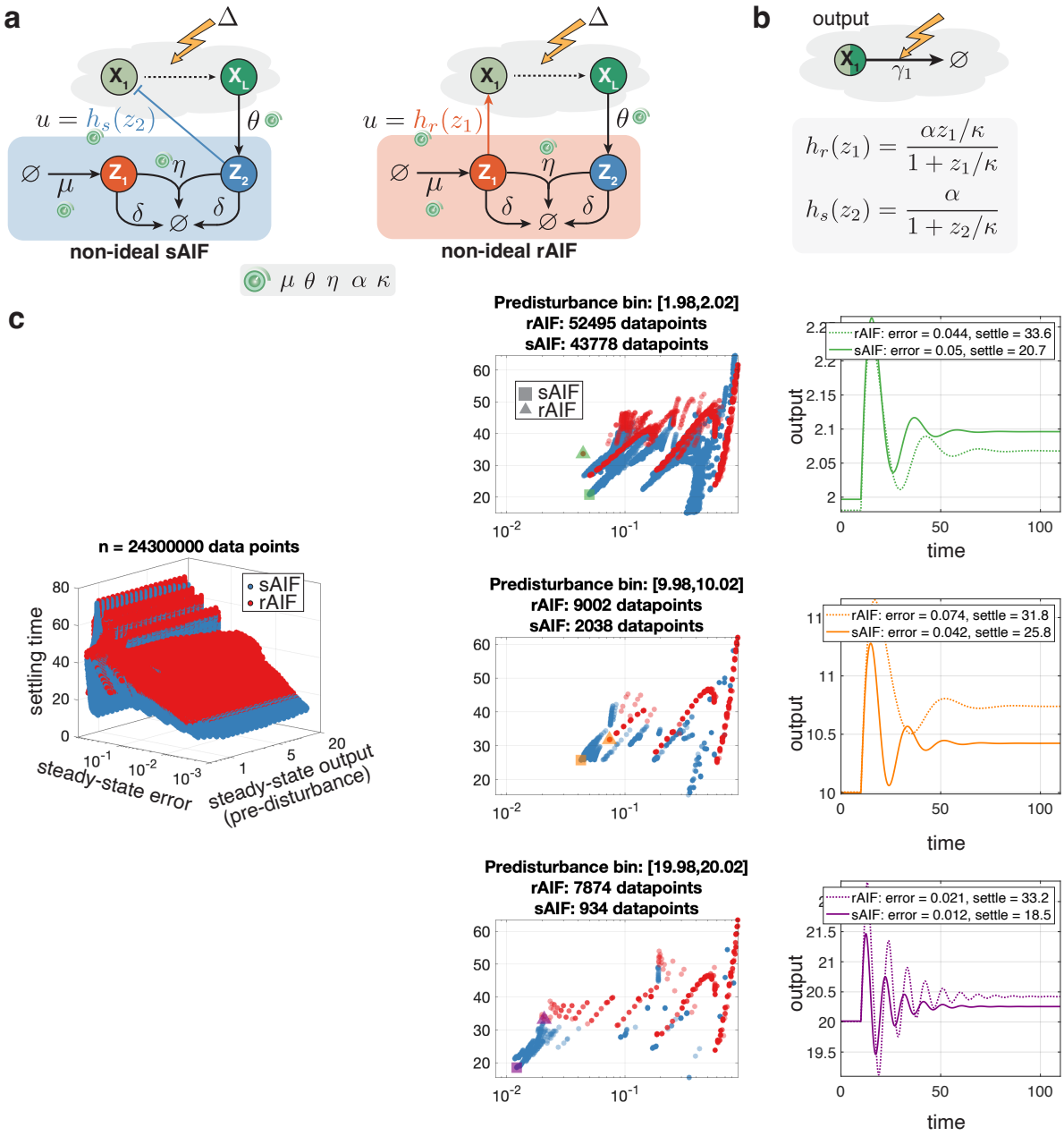

Figure S7: Dynamic performance vs. steady-state error for non-ideal sAIF and rAIF Controllers. (a) Closed-loop network diagrams of the sAIF and rAIF controllers, highlighting the scanned parameters. (b) Regulated network and actuation functions. The regulated network consists of a simple single species process whose production is controlled by the feedback controllers, while its degradation rate γ_1 is disturbed by halving its value. The actuation is modeled via activating and repressing Hill functions for the rAIF and sAIF controllers, respectively, with α as the maximal production rate and κ as the dissociation constant. (c) Simulation results. Controller parameters $\mu, \theta, \eta, \alpha$, and κ were jointly scanned, and for each combination, the pre-disturbance steady-state level, post-disturbance steady-state error, and settling time were computed. Each parameter set corresponds to a data point—shown in blue for sAIF and red for rAIF. The sAIF data points (blue) extend further downward, indicating that sAIF can simultaneously achieve faster settling times without sacrificing steady-state errors. This demonstrates that sAIF relaxes the trade-off between dynamic performance and steady-state error more effectively than rAIF, due to the additional control afforded by its proportional component. Representative data points for sAIF (square) and rAIF (triangle) are highlighted and their dynamic responses are shown in the right-hand-side plots with slices of the 3D plot binned over 3 pre-disturbed steady-state levels. Simulation details: $\gamma_1 = \delta = 0.1$, $\mu, \theta, \alpha \in [0.1, 10]$, $\eta \in [10^{-5}, 10^3]$, $\kappa \in [10^{-3}, 0.1]$. Settling time was defined as the time required for the signal to enter and remain within a 1% tolerance band around the new steady state. Simulations were performed in MATLAB over a grid of 30^5 parameter combinations using a workstation with 128 parallel threads. The three slices are binned across three steady-state output levels (pre-disturbance) given by $2, 10$ and 20 with a bin width of 0.04. The number of data points collected for each slice are shown in the titles of the plots.

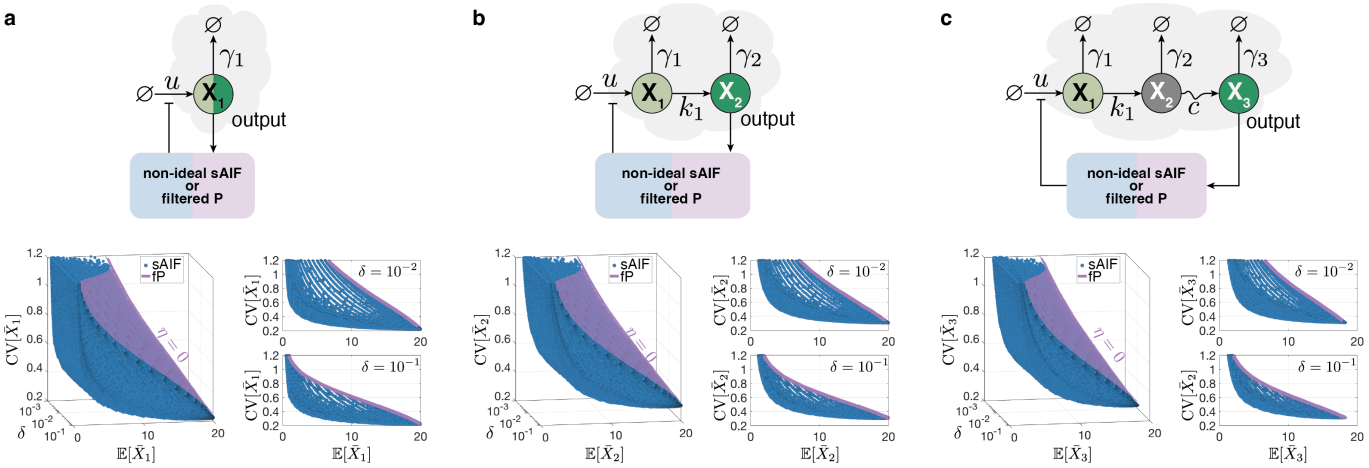

Figure S8: Comparison of stationary noise between the non-ideal sAIF and filtered proportional (fP) controllers in feedback with three regulated networks consisting of (a) one species, (b) two species, and (c) three species. Panel (a) is identical to Fig. 6(e) and is included here for convenience. In all cases, the actuation function is $u = \frac{\alpha}{1+z_2/\kappa}$ with fixed $\alpha = 2$ and $\kappa = 0.05$, while $\delta \in [10^{-3}, 10^{-1}]$ is varied for both controllers. For the non-ideal sAIF controller, $\theta \in [10^{-5}, 10]$, $\mu \in [10^{-1}, 10]$, and $\eta \in [10^{-5}, 10^{5}]$ are also varied across all three networks. For the fP controller, $\theta_p \in [10^{-5}, 10]$ is varied. The simulations consistently show that for a fixed repressor $\mathbf{Z_2}$ (and thus the actuation mechanism h_s), the non-ideal sAIF controller either outperforms or matches the fP controller in reducing stationary noise in the output. The numerical values of the parameters of the three regulated networks are as follows: (a) $\gamma_1 = 0.1$, (b) $\gamma_1 = k_1 = 1, \gamma_2 = 0.1$, and (c) $\gamma_1 = c = k_1 = 1, \gamma_2 = \gamma_3 = 0.1$.

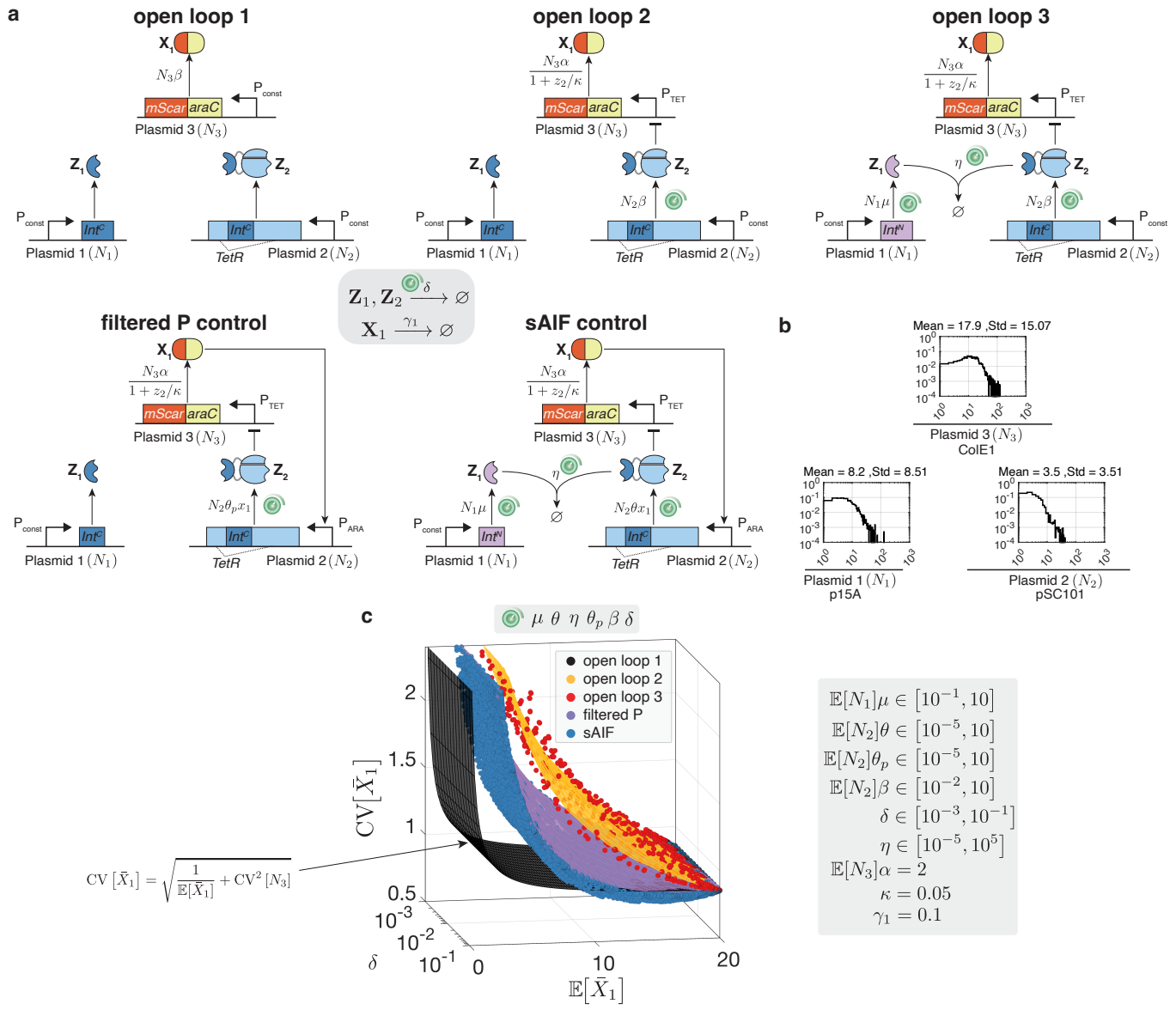

Figure S9: Numerical analysis in the presence of both intrinsic and extrinsic noise. (a) The three open-loop circuits under consideration, filtered proportional control, and sAIF control. In OL 1 and the filtered-proportional control circuit, plasmid 1 serves as a dummy plasmid in the experiments—included solely to ensure that all circuits operate under comparable plasmid burden but do not affect the output. However, it does not influence the regulated output $\mathbf{X_1}$. Similarly, in OL3, both plasmids 1 and 2 are dummy plasmids and do not affect $\mathbf{X_1}$, serving only to maintain consistent experimental conditions. (b) This panel shows the experimentally measured distributions of plasmid copy numbers for three plasmids: p15A, pSC101, and ColE1, as reported in [2]. These distributions are used to model extrinsic noise in our simulations. Specifically, the propensities of the production reactions in the model (as in Fig. 6) are multiplied by the plasmid copy numbers N_1, N_2, and N_3, which are now treated as random variables sampled from these distributions. As noted in [2], the standard deviations are comparable to the means, highlighting the significant cell-to-cell variability in plasmid abundance. (c) The circuits shown in panel (a) are simulated under the same conditions as in Fig. 6, with the key difference being that plasmid copy numbers are now drawn randomly from the distributions shown in panel (b). This introduces extrinsic variability in addition to the intrinsic noise already present. The resulting plot—identical to Fig. 7(e)—is included here for convenience. The fixed and swept parameter values used in the simulations are listed on the right, and can be directly compared with those used in the intrinsic-noise-only case of Fig. 6(e).

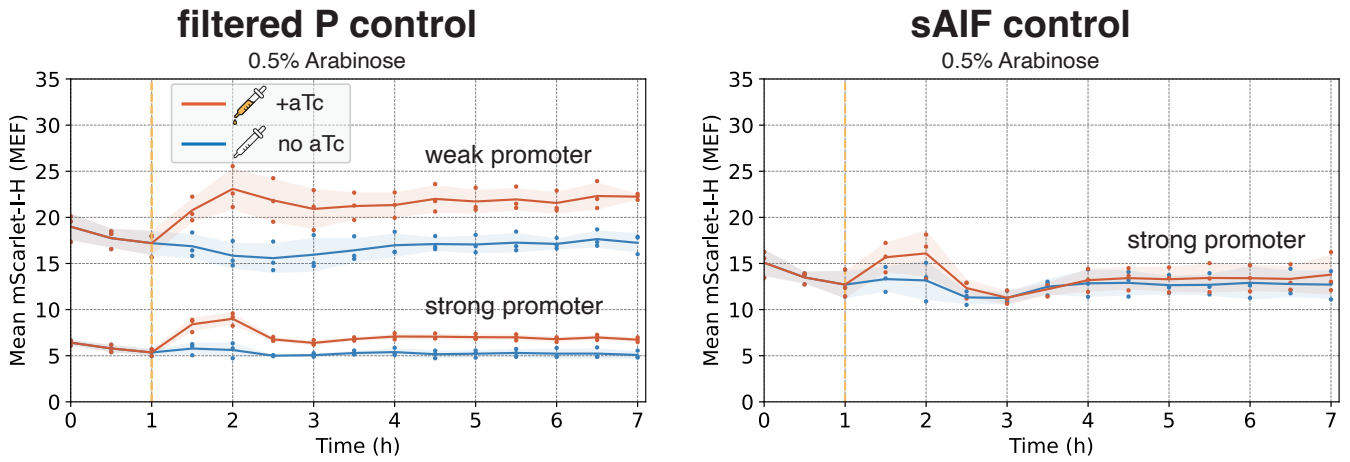

Figure S10: Time-course experiments illustrating the dynamic response of the output to a disturbance. This figure extends Fig. 7(b) by including an additional experiment for the filtered proportional controller, where Gene 2 is driven by both strong and weak promoters. In contrast, Fig. 7(b) depicts only the response for the weak promoter case. Here, we show that the output level, measured in Molecules of Equivalent Fluorochrome (MEF), for the sAIF controller falls between the two levels observed for the filtered proportional controller under strong and weak promoter conditions. Notably, the sAIF controller exhibits significantly improved adaptation, achieving a much smaller steady-state error compared to both cases of the filtered proportional controller.

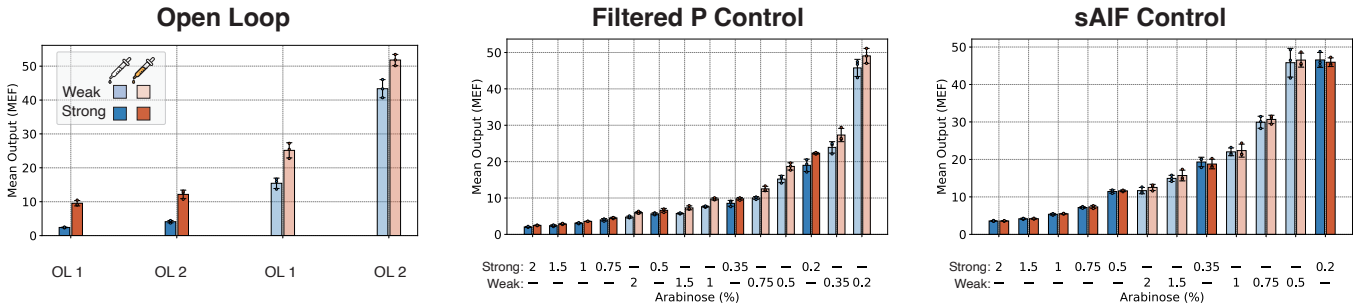

Figure S11: Bar graphs showing the unnormalized data presented in Fig. 7(c). All measurements reported here are in Molecules of Equivalent Fluorochrome (MEF) units.

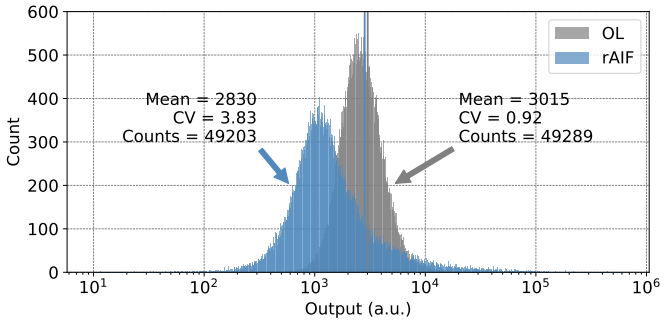

Figure S12: Noise amplification in an rAIF controller. The data in this panel are adapted from previously published measurements of an rAIF controller implemented using Sigma/anti-Sigma sequestration[3]. The two distributions compare the output noise level in the open- and closed-loop circuits with comparable mean levels. Although the rAIF successfully achieved RPA (see[3]), it increases the CV by more than fourfold relative to the open-loop circuit. Note that the mean superfolder GFP output (FL1-A) and CV of previously published flow cytometry measurements of rAIF (0.2% arabinose, 7 nM 3OC6-HSL) and open loop (0.2% arabinose, 0 nM 3OC6-HSL) strains from Aoki et al. (Extended Data Fig. 6(d))[3] are calculated and plotted here.

Plasmid	Gene type	Circuits	Description
pSKA837	1	OL1, OL2, fP	$P_{J23119\text{-}B0033}$-*intC(gp41-1)-B0015*, p15A *ori*, spec^{R}
pSKA838	1	OL3, sAIF	$P_{J23119\text{-}B0033}$-*intN(gp41-1)-B0015*, p15A *ori*, spec^{R}
pSKA839	2 (weak)	OL2, OL3	$P_{J23111\text{-}B0033}$-$tetR_{1\text{-}183}$*::intC(gp41-1)::*$tetR_{184\text{-}212}$*-B0015*, pSC101 *ori*, cam^{R}
pSKA840	2 (strong)	OL1, OL2, OL3	$P_{J23119\text{-}B0033}$-$tetR_{1\text{-}183}$*::intC(gp41-1)::*$tetR_{184\text{-}212}$*-B0015*, pSC101 *ori*, cam^{R}
pSKA841	2 (weak)	fP, sAIF	$P_{araB\text{-}B0033}$-$tetR_{1\text{-}183}$*::intC(gp41-1)::*$tetR_{184\text{-}212}$*-B0015*, pSC101 *ori*, cam^{R}
pSKA842	2 (strong)	fP, sAIF	$P_{araB\text{-}AraJ\text{-}B0033m}$-$tetR_{1\text{-}183}$*::intC(gp41-1)::*$tetR_{184\text{-}212}$*-B0015*, pSC101 *ori*, cam^{R}
pSKA843	3	OL2, OL3, fP, sAIF	$P_{LtetO\text{-}1\text{-}B0033}$-*V5::araC::mScarlet-I-B0015*, ColE1 *ori*, carb^{R}
pSKA884	3	OL1	$P_{J23101*}$-*V5::araC::mScarlet-I-B0015*, ColE1 *ori*, carb^{R}
pSKA885	3	OL1	P_{J23114}-*V5::araC::mScarlet-I-B0015*, ColE1 *ori*, carb^{R}
pSKA886	3	OL1	P_{J23106}-*V5::araC::mScarlet-I-B0015*, ColE1 *ori*, carb^{R}
pSKA887	3	OL1	P_{J23102}-*V5::araC::mScarlet-I-B0015*, ColE1 *ori*, carb^{R}
pSKA888	3	OL1	P_{J23111}-*V5::araC::mScarlet-I-B0015*, ColE1 *ori*, carb^{R}
pSKA889	3	OL1	P_{J23119}-*V5::araC::mScarlet-I-B0015*, ColE1 *ori*, carb^{R}

Table S1: List of plasmids constructed and used in this study. Plasmid sequences can be found at the following Github repository https://github.com/Maurice-Filo/Sensor-Based-Biomolecular-Integral-Controllers.

Circuit	Gene 1	Gene 2 promoter	Testing strain	Host strain	Plasmids (in order: Gene type 1, 2, 3)
Open loop 1	*intC*	strong	SKA1838	SKA360	pSKA838, pSKA840, pSKA884
Open loop 1	*intC*	strong	SKA1839	SKA360	pSKA838, pSKA840, pSKA885
Open loop 1	*intC*	strong	SKA1840	SKA360	pSKA838, pSKA840, pSKA886
Open loop 1	*intC*	strong	SKA1841	SKA360	pSKA838, pSKA840, pSKA887
Open loop 1	*intC*	strong	SKA1842	SKA360	pSKA838, pSKA840, pSKA888
Open loop 1	*intC*	strong	SKA1843	SKA360	pSKA838, pSKA840, pSKA889
Open loop 2	*intC*	weak	SKA1785	SKA360	pSKA838, pSKA839, pSKA843
Open loop 2	*intC*	strong	SKA1787	SKA360	pSKA838, pSKA840, pSKA843
Open loop 3	*intN*	weak	SKA1784	SKA360	pSKA837, pSKA839, pSKA843
Open loop 3	*intN*	strong	SKA1786	SKA360	pSKA837, pSKA840, pSKA843
Filtered P	*intC*	weak	SKA1789	SKA360	pSKA838, pSKA841, pSKA843
Filtered P	*intC*	strong	SKA1791	SKA360	pSKA838, pSKA842, pSKA843
sAIF	*intN*	weak	SKA1788	SKA360	pSKA837, pSKA841, pSKA843
sAIF	*intN*	strong	SKA1790	SKA360	pSKA837, pSKA842, pSKA843

Table S2: List of testing strains constructed and used in this study.

References

1. Gillespie, D.T. (1977). Exact stochastic simulation of coupled chemical reactions. The journal of physical chemistry *81*, 2340–2361.

2. Shao, B., Rammohan, J., Anderson, D.A., Alperovich, N., Ross, D., and Voigt, C.A. (2021). Single-cell measurement of plasmid copy number and promoter activity. Nature communications *12*, 1475.

3. Aoki, S.K., Lillacci, G., Gupta, A., Baumschlager, A., Schweingruber, D., and Khammash, M. (2019). A universal biomolecular integral feedback controller for robust perfect adaptation. Nature *570*, 533–537.